

NG9-33438
NASA CR-103825

RESEARCH FOR THE MEASURING OF NEUTRON INTENSITY IN SPACE

By J. A. Lockwood

CASE FILE
COPY

FINAL REPORT

June 1969

Prepared under Contract No. 164 by

University of New Hampshire
Department of Physics
Durham, New Hampshire 03824

The information presented herein was developed from NASA-funded work. Since the report preparation was not under NASA control, all responsibility for the material in this document must necessarily reside in the author or organization who prepared it.

NATIONAL AERONAUTICS AND SPACE ADMINISTRATION

ACKNOWLEDGMENTS

In this project Dr. R. E. Houston, University of New Hampshire, Department of Physics, has been a co-investigator.

We are grateful to the following people who have worked on various phases of this project:

Archer Buck
Dana Schow
Daniel Huntley
Richard Simmons
Karl Pratt
Shadrack Ifedili
Herbert Scheibel

Earl Noble
Donald Meeker
Sheila Dewdney
Antal Sarkady
Richard Wakefield
Dale Chinburg
Karl Flanders

The following students have been supported partially or completely under this contract:

Lawrence A. Friling, M.S.
Thomas Wilson, M.S.
Lee Larson, Ph.D.
Edward Nickoloff, M.S.

Richard St. Onge, Ph.D.
John Apostolos, Ph.D. cand.
David Klumpar, Ph.D. cand.

We appreciate the many helpful discussions with Dr. E. L. Chupp and Dr. D. J. Forrest.

TABLE OF CONTENTS

	Page
1. SUMMARY	1
2. INTRODUCTION	4
3. COSMIC-RAY NEUTRON MEASUREMENTS (J.A. Lockwood et al.)	
3.1 Abstract of "Design of a Neutron Monitor for Measurements in Space" (M.S. Thesis)	5
3.2 Neutron Albedo Measurements on Rocket Flights (Proc. Phys. Soc., London, 1965)	7
3.3 Cosmic-Ray Neutron Flux Measurements above the At- mosphere (<u>J. Geophys. Res.</u> , <u>73</u> , 6649, 1968).	23
3.4 A Fast Neutron-Gamma Detector for Space Research (<u>IEEE Trans. on Nucl. Science</u> , <u>NS-15</u> , 264, 1968)	66
3.5 A Simple High Resolution Pulse Shape Discrimi- nator (<u>Nuclear Instr. and Methods</u> , <u>69</u> , 1969)	78
3.6 A Total Enclosing Active Charged Particle Shield (in press <u>Nuclear Instr. and Methods</u> , 1969).	96
3.7 The Energy Spectrum and Flux of Fast Neutrons in the Atmosphere (in press <u>The Physical Review</u> , 1969).	108
4. ELECTRON DENSITY MEASUREMENTS IN THE IONOSPHERE (R. E. Houston et al.)	
4.1 Abstract entitled "Electron Density Measurements from Southern Latitude Rocket Flights"(URSI Spring Meeting, 1966)	138
4.2 Abstract entitled "Lower Ionospheric Parameters as Measured from Sounding Rockets" (URSI Fall Meeting, 1966).	140
4.3 Abstract entitled "A Measurement of the Effective Recombination Coefficient in the Lower Ionosphere" (<u>Transactions</u> , <u>49</u> , 735, 1968).	141

TABLE OF CONTENTS (continued)

	Page
4.4 A Sensitive Radio Receiver for Ionosphere Measurements (in press <u>Scientific Instruments</u> , 1969) . . .	142
4.5 A Measurement of the Effective Recombination Coefficient in the Lower Ionosphere (in press <u>Journal of Geophysical Research</u> , 1969)	150

SUMMARY

We report here the results of measurements of (1) the fast neutron flux and energy spectra near the top and above the earth's atmosphere and (2) the electron density in the ionosphere. Observations were made both on rocket and balloon flights at several different epochs and at a range of geographic latitudes.

The first measurements of the cosmic-ray neutron flux above the atmosphere were made with a standardized He^3 proportional counter encased in a polyethylene moderator which, in turn, was surrounded by charged particle counters to reject neutron events associated with neutron production in the neutron detector assembly by galactic and solar cosmic rays. Flights were made from 1965-1967 at 0, 20, 50 and 70° geomagnetic latitudes on Nike-Apache and Nike-Tomahawk rocket vehicles. The neutron leakage fluxes at these latitudes were 0.08 ± 0.02 , 0.21 ± 0.03 , 0.45 ± 0.06 , and $0.85 \pm 0.12 \text{ cm}^{-2}\text{sec}^{-1}$ in the energy range 10 to $5 \times 10^6 \text{ ev}$. This latitude effect is about 10/1, less than the 13/1 ratio calculated theoretically.

These results on the latitude dependence of the cosmic neutron leakage flux indicated the importance of determining the neutron energy spectrum between 1 and 50 MeV. A fast neutron gamma detector was designed for space applications.

This instrument included a highly efficient 4π charged particle shield, a pulse-shape discriminator to separate neutrons from gamma-rays in the energy range 1-50 MeV and 1-7 MeV respectively, an in-flight calibrator, and, most importantly, provided for separately extracting the recoil proton, alpha particle and Compton electron spectra from which the neutron and gamma-ray spectra can be unfolded. The first balloon flight of this detector was made from Palestine, Texas, on September 7, 1968, and the neutron energy spectrum in the atmosphere at Pforter maximum ($\sim 100 \text{ g/cm}^2$) was measured from 3 to 20 MeV. The slope of the differential neutron energy spectrum $\left(\frac{dN}{dE} = F(E)/E^{\beta(E)} \right)$ decreased from about 4.0 ± 1.0 between 3-6 MeV to 1.2 ± 0.5 between 12-20 MeV. Since this neutron energy spectrum is considerably steeper than previously measured spectra, further observations are being conducted.

Propagation experiments in the 1 MHz and 3 MHz range were utilized to determine electron density distributions in the lower ionosphere. From the Faraday rotation data obtained from the rocket telemetry signal and the linearly polarized ground-based transmission are used in the appropriate theoretical equations to deduce an electron density of about $5 \times 10^4 \text{ cm}^{-3}$ at 100 km and 10^2 cm^{-3} at 65 km.

The charged particle spectra obtained on a rocket flight at Ft. Churchill were used to calculate the electron production

in the lower ionosphere. Since the electron density was being measured simultaneously with a Faraday rotation experiment, the effective recombination coefficient (the ratio of the electron production to the electron density squared) was determined to be approximately $6 \times 10^{-7} \text{ cm}^3 \text{ sec}^{-1}$ at 65 km.

INTRODUCTION

In this investigation we have measured:

1. the fast neutron flux and energy spectra near the top of and above the atmosphere;
2. electron density measurements in the ionosphere;
3. solar X-rays; and
4. solar ultraviolet radiation.

We have collected in this report all the publications pertaining to the above investigations and have arranged them chronologically into two groups: cosmic-ray neutron and ionospheric measurements.

COSMIC-RAY NEUTRON PUBLICATIONS

J. A. Lockwood et al.

DESIGN OF A NEUTRON MONITOR FOR MEASUREMENTS IN SPACE

J. A. Lockwood and L. A. Friling
University of New Hampshire
Physics Department
Durham, New Hampshire

ABSTRACT

A study has been made of suitable neutron detecting systems for space measurements. As a results of this investigation a neutron monitor, consisting of a He^3 proportional counter encased in a polyethylene moderator which, in turn, is surrounded by charged particle counters, has been constructed and tested. The efficiency of this neutron detector system is 2.0 counts/neutron/cm² for 14 MeV neutrons and 20 cts/n/cm² at thermal energies. The electronics system is designed to reject neutron events occurring within 200 microseconds after a charged particle counter is triggered, thereby providing discrimination against neutron production in the detector.

A Li^6I scintillator encased in a plastic scintillator which acts as both a moderator for the neutrons and a charged particle detector has also been built and tested. This detector system was not adopted now as "space neutron monitor" because pulse shaping circuits were required and the rejection of gamma ray events was not as good as for the He^3 detector system.

Studies have also been made of detectors for fast neutron measurements and directional neutron fluxes.

NEUTRON ALBEDO MEASUREMENTS ON ROCKET FLIGHTS

Neutron Albedo Measurements on Rocket Flights

J. A. Lockwood, L. Friling, T. Wilson, and E. Chupp

University of New Hampshire

Durham, New Hampshire

Introduction:

Neutrons are produced by the interaction of the cosmic radiation with nuclei in the earth's atmosphere, and a fraction of these neutrons leak out from the atmosphere, giving rise to the earth's neutron albedo. The decay of some of these neutrons within the magnetosphere can supply part of the protons and electrons trapped in the Van Allen radiation belts (Singer, 1958). Any evaluation of the trapping mechanism for charged particles from this source will require knowledge of the neutron energy spectrum and flux, as well as the spatial and temporal variations.

The present experiment, designed to measure the integrated flux of neutrons with energies up to ~ 15 Mev, consists of a moderated He^3 proportional counter for neutron detection surrounded by a ring of charged-particle detectors to count and discriminate against protons and alpha-particles that can produce neutrons in the detector assembly. This detecting system was flown on four rocket flights in 1965 at geomagnetic latitudes of 0° , 19° , and 49° and essentially the same longitude.

Table I gives the launch dates, latitudes, longitudes, and gated counting rates.

Table I. Summary of Neutron Albedo Measurements

<u>Launch Date</u>	<u>Geographic</u>		<u>Geomagnetic</u>	Counts/sec
	<u>Latitude</u>	<u>Longitude</u>	<u>Latitude</u>	
3 February 1965 1808 UT	38.0° N	75.5° W	49.4° N	2.3
2 April 1965 1320 UT	12.0° S	78.2° W	0.6° S	0.54
5 April 1965 1942 UT	30.5 S	75.0° W	19.0° S	0.85
13 April 1965 1711 UT	60.0° S	78.0° W	48.5° S	2.7

Experimental Method:

The basic detector, shown in Figure 1, consists of a He^3 proportional counter for neutron detection, encased in a polyethylene moderator approximately $7/8$ inch thick. The Sylgard used as a potting compound for high voltage insulation and interstitial support also acts as a moderator, especially at the ends of the tube array. The He^3 counter is one inch in diameter, 4 inches in active length, and is filled to a pressure of 10 atmospheres. The proportional counters surrounding the polyethylene moderator are $1/2$ inch in diameter by 7 inches active length, are filled with a mixture of argon and methane, and are operated in the semi-proportional region. This experimental arrangement is a modification of the units flown previously on polar-orbiting satellites (Trainor and Lockwood, 1964).

The four separate banks of five counters each are operated in two coincidence arrays composed of opposite banks, and the separate outputs also added serially. The output pulses from both the add and coincidence modes are scaled and fed to the telemetry, as well as being used to trigger a univibrator which blanks certain neutron channels. The blanking time is set for 200 μsec , which is estimated to be greater than three times the half-life of neutrons in the detecting system. Within the add mode circuit a binary stage provides an additional 200 μsec of blanking time to discriminate against two charged-particle events occurring within 200 μsec . Outputs from the total and from both gated modes of the He^3 counter are scaled and fed to the telemetry system.

The neutron detector assembly is located as far forward as possible, away from dense and hydrogeneous materials in which neutrons might be produced. The clamshell nose cone section, which surrounds the detector, is jettisoned above the atmosphere to remove a significant source of neutron production.

The detecting system was calibrated by exposing the complete detector assembly to fluxes of gamma rays and neutrons. The gamma-ray response of the detector was measured with a calibrated Co^{60} source and was found to be negligible. Neutrons of different energies were produced by a calibrated Ra-Be source and a 400 Kev Van de Graaff accelerator. The accelerator provided a source of nearly monoenergetic neutrons at 14.4, 5.2, 2.9, and 0.11 Mev. The absolute neutron fluxes were determined by foil activation techniques, and an associated particle detecting system, as well as the calibrated Ra-Be neutron source. A standard long counter (Hanson and McKibben, 1947) was used as a monitor during the accelerator runs. The neutron energy calibration is summarized in Figure 2. The directional response of the complete sensor, measured at 2.9 Mev, is shown in Figure 3. The slight asymmetry in the angular response is due to the high voltage package, which is potted and located directly below the detector assembly.

Using the calibration curve in Figure 2 and the energy spectrum given by Lingenfelter (1963), the counting rate of the detector assembly can be converted to a neutron flux. If the differential neutron flux in neutrons/cm² sec Mev is given by $j(E)$ and the response of the detector in counts/cm² is given by $S(E)$, the mean response of the detector is :

$$\frac{\bar{S}}{S} = \frac{\int J(E)S(E)dE}{\int J(E)dE} \quad (\text{counts/neutron/cm}^2). \quad \text{For the detectors}$$

flown $\bar{S} = 5.5 \text{ cm}^2$.

It should be noted that the energy calibration in the range $10^5 < E_n < 10^7$ ev is most important, because according to Lingenfelter's spectrum (1963), two-thirds of the neutron flux lies in this range, whereas only one-tenth lies below 3×10^3 ev and one-tenth above 3.5×10^6 ev.

Results of Neutron Albedo Measurements:

The gated neutron counting rates for the He^3 detector assembly are shown in Figure 4. No correction has been applied for the altitude above the earth (Hess et al., 1961), because the counting rates shown represent the integrated rate above 2×10^5 ft. for the flights. The background effects as measured are negligible. The error flags represent the statistical standard deviation for each flight and a small error from the intercalibration of the flight units. The latitude effect for the gated neutron counting rate between 50° and 0° geomagnetic latitude is 4:1. The calculated neutron leakage flux for solar minimum (Lingenfelter, 1963) is indicated in Figure 4 by the smooth curve normalized to the experimental value at 0° .

When measuring a neutron flux in the presence of a background of energetic charged particles ($T_0 \gtrsim 100$ Mev), local production of neutrons must always be evaluated. Table II lists the contribution to the counting rates from the principle sources of local production at the different latitudes. The method used to calculate the neutron production is essentially the same as that outlined by Trainor and Lockwood (1964). However, in the present calculation,

several refinements have been added to improve the accuracy. These refinements include: (1) the energy variation of the primary cosmic radiation was taken into account, rather than assuming it to be a monoenergetic flux; (2) the interactions of primary alpha particles were included; (3) the secondary neutron production by fast knock-on particles (cascade protons) was evaluated; and (4) an energy distribution for the evaporation neutrons was folded into the known energy response of the detector. Since the difference between the gated and the total neutron counting rates is due to neutron production in the detector assembly, we can compare this measured quantity with the calculated production in the module due to primary cosmic radiation. The last column in Table II gives the above measured production rate. The agreement is good considering the large uncertainties in the differences for such low counting rates. During none of the flights was the neutron channel gated off more than three percent of the time, which is within the statistical errors. For the low counting rates obtained, no estimate could be made of local production in the nose cone assembly from the difference in counting rates before and after ejection. The two gated neutron counting rates were essentially the same, indicating that most of the charged particles were primary cosmic rays.

By converting the neutron counting rates to a neutron flux, the results can be compared with calculations of Lingenfelter (1963) and other experimental results. In Figure 5 is shown the neutron flux values from these flights as a function of geomagnetic latitude. The error flags indicated include statistical, intercalibration and absolute calibration errors. The smooth curve is the calculated

Table II. Calculated and Measured Neutron Counting Rates from
Local Production on Rocket Vehicle

<u>Latitude (Geomagnetic)</u>	<u>P_M(bv)</u>	<u>Calculated (Cts/sec)</u>			<u>Measured (Cts/sec)</u>	
		<u>Moderator Assembly</u>	<u>Clamshell Nose Cone</u>	<u>Vehicle</u>	<u>Moderator Assembly</u>	
49	2.5	0.4 ± 0.2	0.2 ± 0.1	<0.1	0.3 ± 0.15 0.6 ± 0.3	
20	~8.0	0.15 ± 0.07	0.07 ± 0.03	<0.1	0.1 ± 0.1	
0	14	0.06 ± 0.03	0.03 ± 0.01	<0.05	0.6 ± 0.2	

flux of Lingenfelter at minimum solar activity. At low latitudes the measurements and the calculations agree. At higher latitudes, however, the measured values fall slightly below the calculated flux.

The data of Figure 5 have been replotted in Figure 6 with other comparable neutron measurements above the atmosphere added. Again there is good agreement among the experimental measurements at the low latitudes. The results of Albert et al. (1962) on polar-orbiting satellites, and of Williams and Bostrom (1964) on the Traac satellite have not been included because in both cases local production effects were large. The excellent fast neutron measurements by Haymes (1964) and Mendell and Korff (1963) near the top of the atmosphere have not been included either, because it is difficult to extrapolate these results above the atmosphere. The smaller latitude effect measured by Trainor and Lockwood (1964) on the polar-orbiting satellites is not fully understood.

In conclusion, there is reasonable agreement at low latitudes among the measurements of neutron albedo fluxes and calculated and experimental values. The latitude dependence of the neutron leakage flux is still uncertain. More rocket flights at higher latitudes are now being made to determine this quantity. Clearly, further measurements with more efficient detecting systems which include methods to determine the neutron energy distribution are needed for the energy interval $10^5 < E_n < 10^7$ ev.

This research was supported by the National Aeronautics and Space Administration under Contract NASr-164, and by the Air Force Cambridge Research Laboratories, Office of Aerospace Research, USAF, under Contract AF19(628)-2352.

References

- Albert, R. D., C. Gilbert, and W. N. Hess,
J. Geophys. Research 67, 3537, 1962.
- Hanson, A. O., and J. L. McKibben
Phys. Rev. 72, (8), 673, 1947.
- Haymes, R. C. J. Geophys. Research 69, 841, 1964.
- Hess, W. N., E. H. Canfield, and R. E. Lingenfelter
J. Geophys. Research 66, 665, 1961.
- Lingenfelter, R. E., J. Geophys. Research 68, 5633, 1963.
- Mendell, R. B., and S. A. Korff
J. Geophys. Research 68, 5487, 1963.
- Singer, S. F. Phys. Rev. Letters 1 (5), 181-183, 1958.
- Trainor, J. H., and J. A. Lockwood
J. Geophys. Research 69, 3115, 1964.
- Williams, D. J., and C. O. Bostrom
J. Geophys. Research 69, 377, 1964.

Figure Captions

- Figure 1. Schematic diagram of the He^3 neutron detecting system.
2. Efficiency of the He^3 neutron detector system as a function of neutron energy from 10^{-2} to 10^7 ev.
 3. Directional response of the neutron detector. 0° is along the axis of He^3 proportional counter.
 4. The gated neutron counting rate above the atmosphere for the four flights. The smooth curve is the calculated neutron leakage at solar minimum (Lingenfelter, 1963) normalized to the experimental data at the equator.
 5. The measured neutron albedo flux above the atmosphere. The smooth curve is the calculated neutron leakage at solar minimum (Lingenfelter, 1963).
 6. The measured neutron albedo flux above the atmosphere. The calculated neutron albedo at both solar maximum and minimum is indicated (Lingenfelter, 1963).

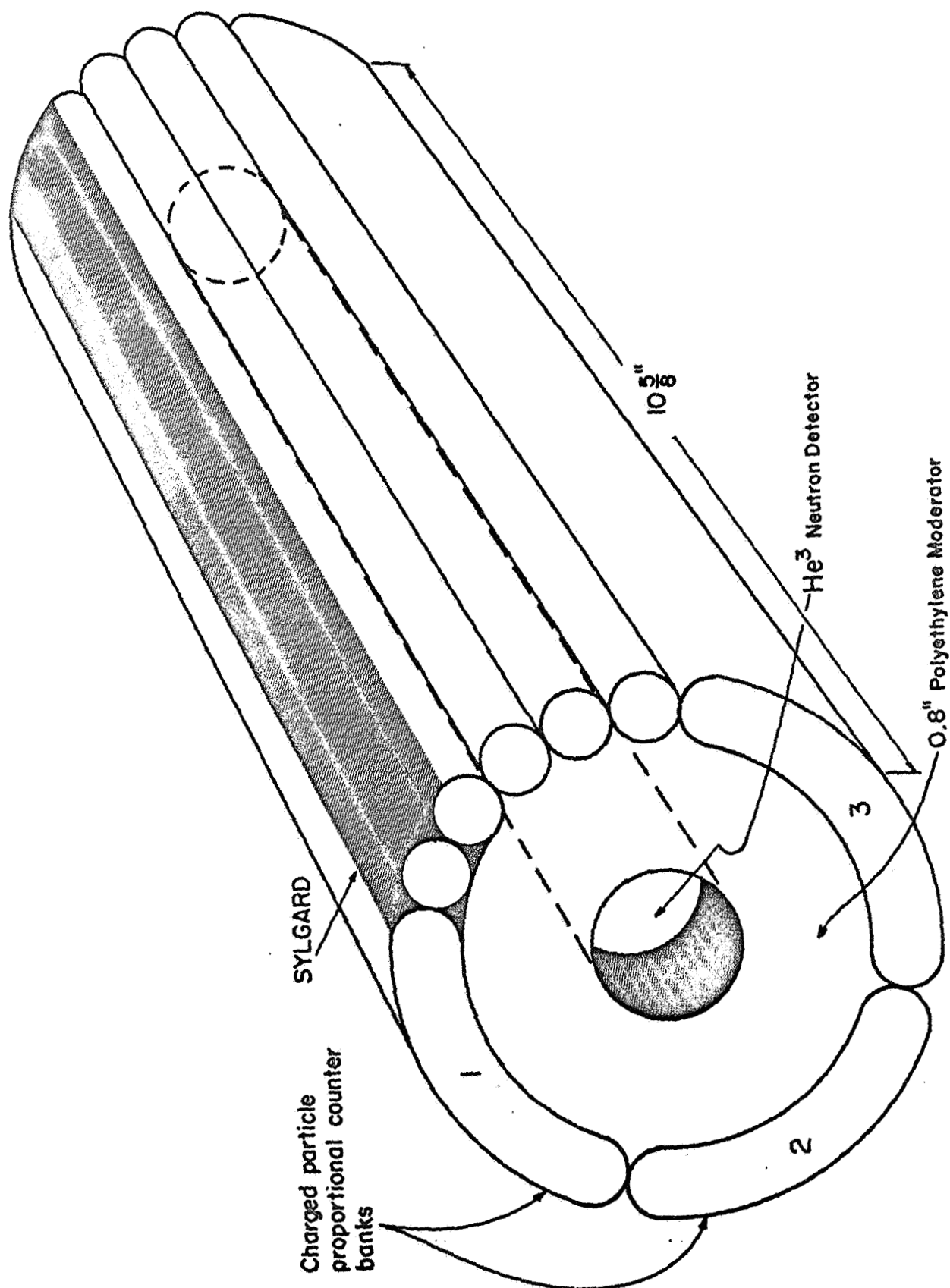
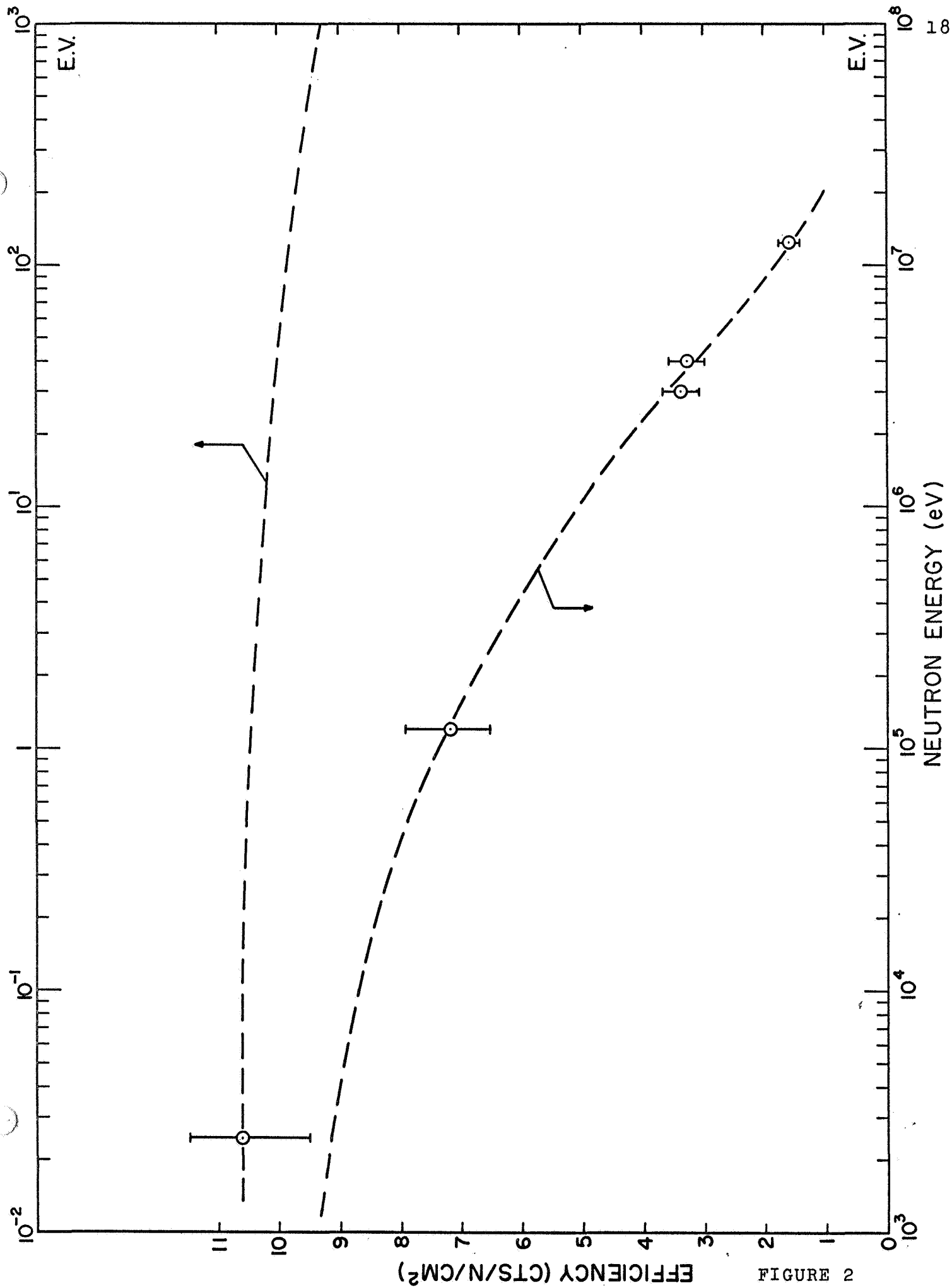


FIGURE 1



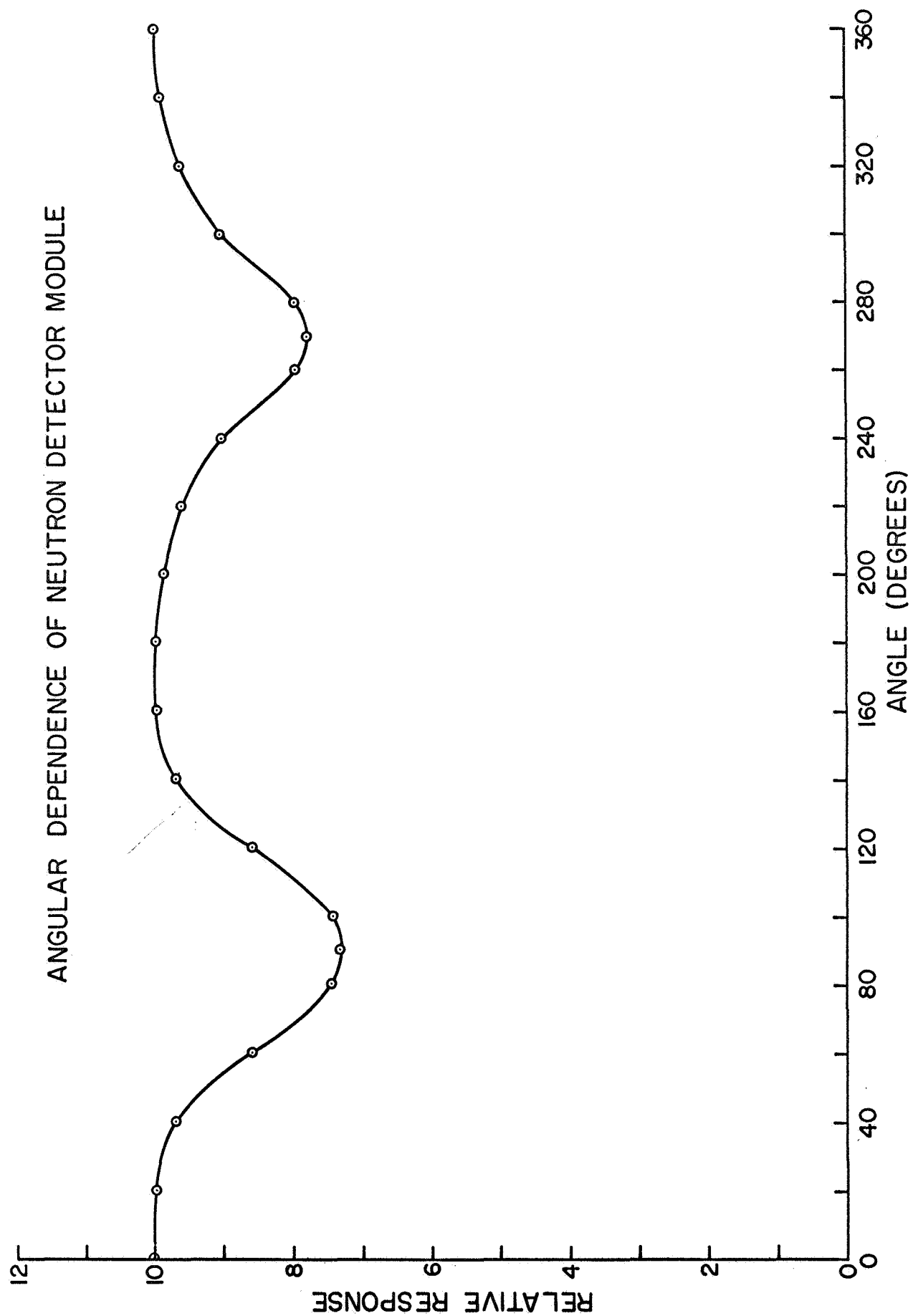


FIGURE 3

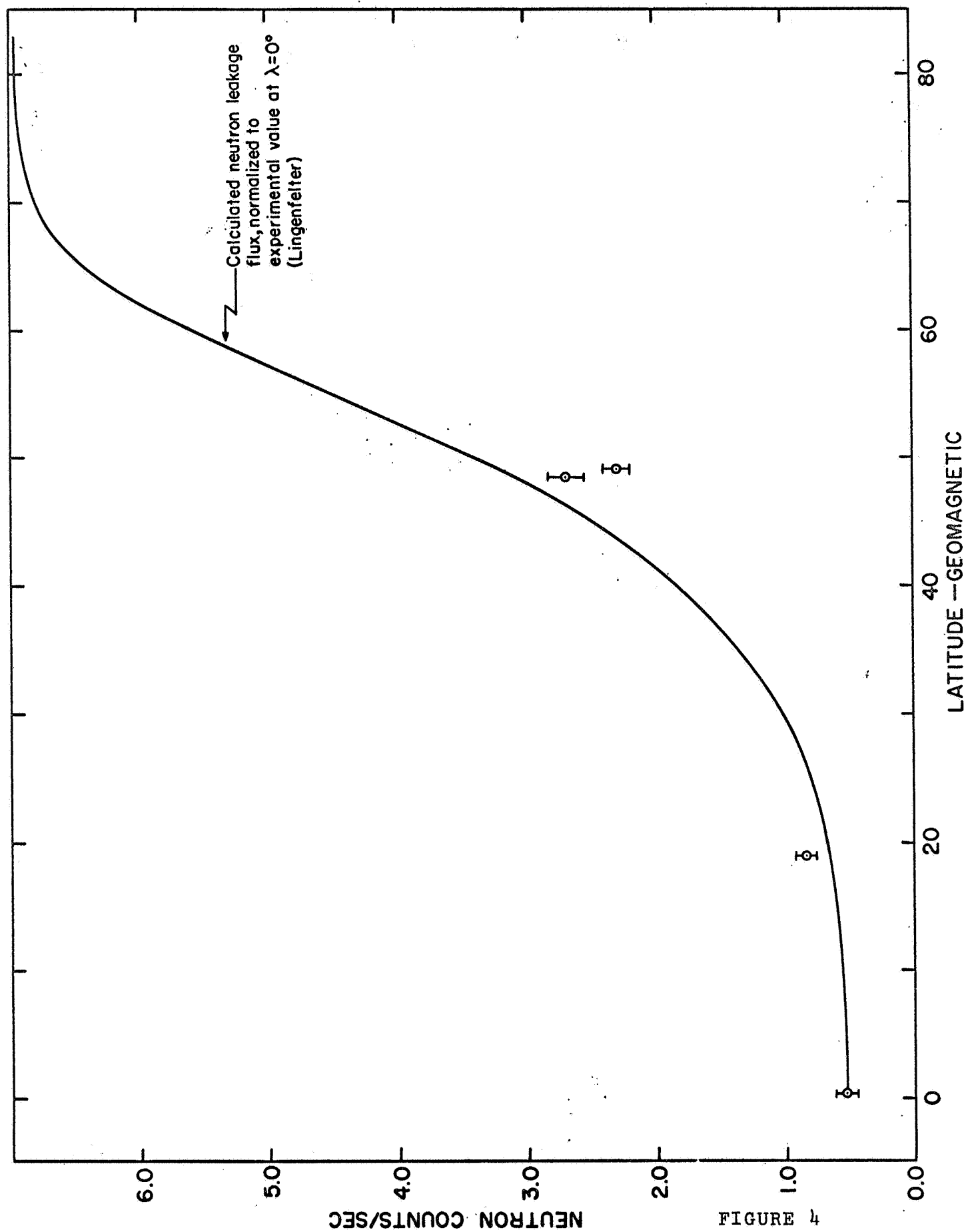
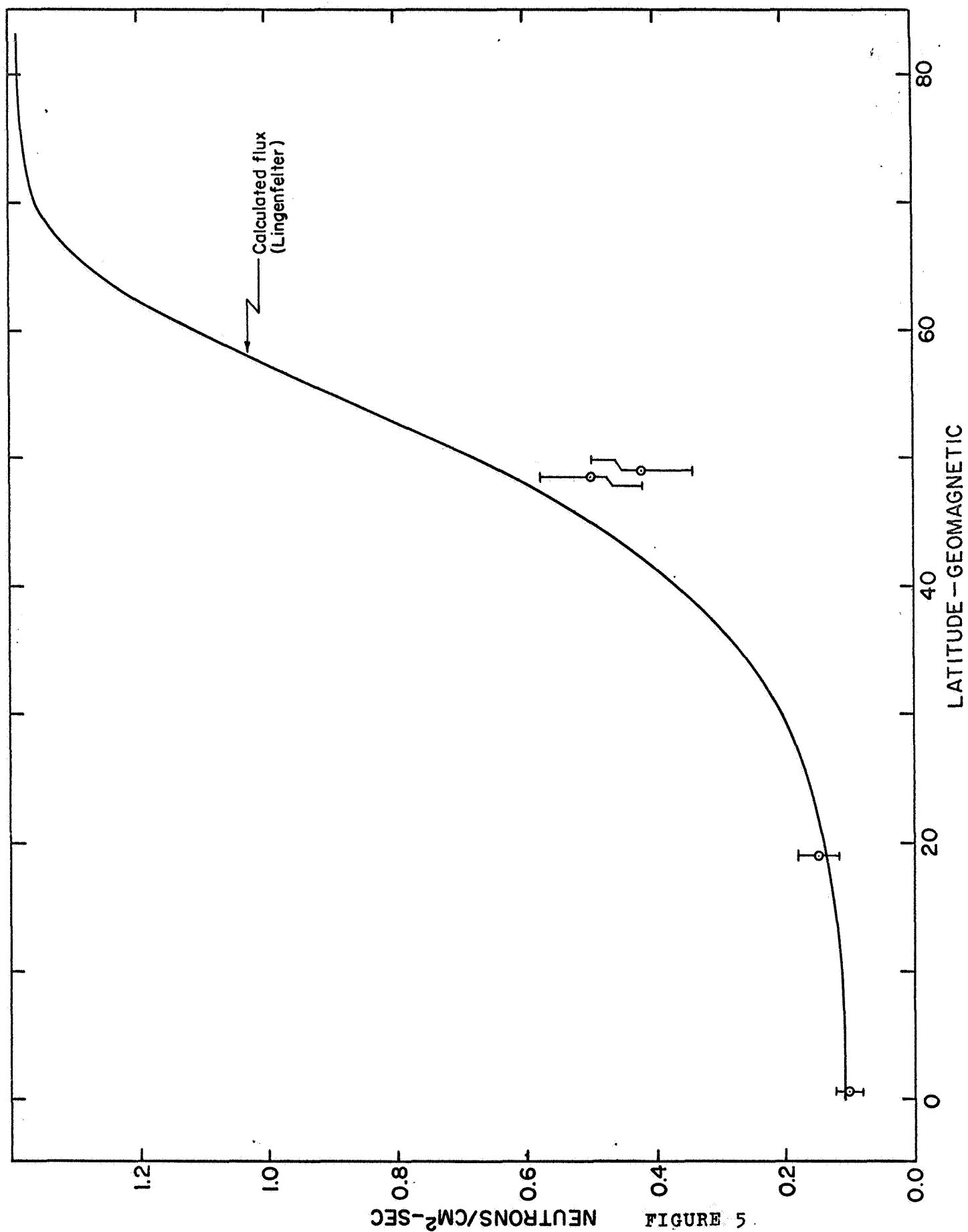


FIGURE 4



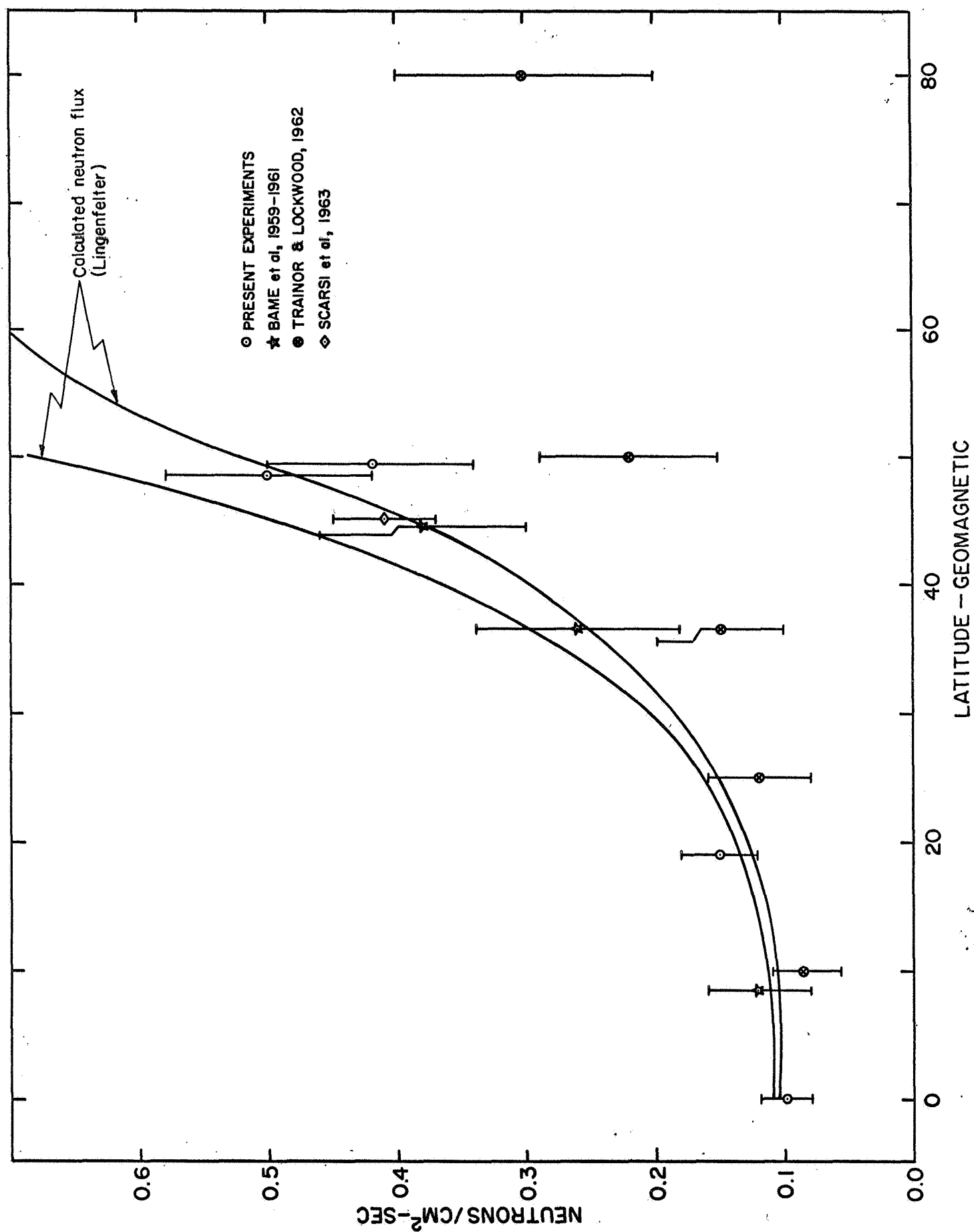


FIGURE 6

COSMIC-RAY NEUTRON FLUX MEASUREMENTS ABOVE THE ATMOSPHERE

ABSTRACT

Measurements have been made of the neutron intensities above the atmosphere at rocket altitudes with a moderated He^3 neutron detector. The He^3 proportional counter was encased in a polyethylene moderator, and the moderator and neutron detector were surrounded by a ring of charged particle counters to discriminate against neutrons produced in the detector assembly by galactic and solar cosmic rays. Flights were made from 1965-1967 at 0° , 20° , 50° , and 70° geomagnetic latitudes (λ). The neutron counting rates at these latitudes are 0.3, <0.7 , 1.7, and 3.0 sec^{-1} . These counting rates can be converted to a neutron leakage flux in the energy range 10 to $5 \times 10^6 \text{ ev}$, using the neutron detector calibration curve and Lingenfelter's calculated neutron energy spectrums at different latitudes. The neutron leakage flux is 0.08 ± 0.02 and $0.80 \pm 0.10 \text{ neutrons/cm}^2 \text{ sec}$ at $\lambda = 0^\circ$ and $\lambda = 70^\circ$ respectively. This latitude effect is about 10/1, less than the 13/1 ratio calculated by Lingenfelter (1963). For $\lambda < 50^\circ$ the measured and the calculated neutron fluxes agree.

COSMIC RAY NEUTRON FLUX MEASUREMENTS

ABOVE THE ATMOSPHERE

J. A. Lockwood
L. A. Friling
Department of Physics
University of New Hampshire
Durham, New Hampshire
03824

Introduction

Neutrons in the earth's atmosphere are produced by the interaction of the cosmic radiation with air nuclei. A fraction of these neutrons leak out from the atmosphere giving rise to the earth's neutron albedo. The radioactive decay of some of these neutrons within the magnetosphere is a source of the protons and electrons trapped in the Van Allen radiation belts, (Singer, 1958). Any evaluation of the trapping mechanism for charged particles from this source will require knowledge of the neutron energy spectrum and flux, as well as the spatial and temporal variations.

Calculations have been made of the intensity and energy spectrum of the neutron leakage. The earlier calculations by Kellogg (1959); Hess (1959); Hess, Canfield and Lingenfelter (1961); and Newkirk (1963) were made at particular latitudes and times. The more recent calculations by Lingenfelter (1963) include the variation of the cosmic-ray production with latitude, altitude and time in the solar cycle. From these calculations the latitude and time dependent neutron leakage flux was calculated by a multigroup diffusion code.

Lingenfelter and Flamm (1964) have extended the calculations to include the production and leakage of neutrons from solar proton events. Dragt, Austin, and White (1966) and Hess and Killeen (1966) have used these calculations to determine quantitatively the contributions to the radiation belts. Both conclude that solar protons and solar neutrons make an insignificant contribution to the protons trapped in the radiation belts. However, Hess and Killeen conclude that the decay of cosmic-ray produced neutrons leaking out of the atmosphere can be the main source of the trapped proton flux ($E > 20$ Mev). On the other hand, Dragt et al. conclude that the trapped protons ($E > 20$ Mev) can be explained by this mechanism only if the ratio of source strength to loss mechanism is increased by a factor of 50 from the values used. Both agree that for trapped protons with $E < 20$ Mev the cosmic-ray neutron source is inadequate to produce the measured proton fluxes.

The present experiment was designed to measure the integrated flux of neutrons with energies to about 15 Mev at altitudes up to 350 km above the earth. The neutron detector consisted of a moderated He^3 proportional counter surrounded by a ring of charged particle detectors to count and discriminate against protons and alphas that can produce neutrons in the detector assembly. This detecting system was flown on Nike-Apache and Nike-Tomahawk rockets at several latitudes over the period from 1965-1967, near the minimum in solar activity. We present in this paper the experimental

results from these flights, comparisons with other experimental measurements along with the calculations of Lingenfelter (1963), and interpretations of these results.

Experimental Method

The basic detector, shown in Figure 1, consists of a He^3 proportional counter for neutron detection, encased in a polyethylene moderator approximately 7/8 inch thick. The Sylgard used as a potting compound for high voltage insulation and interstitial support also acts as a moderator, especially at the ends of the tube array. The He^3 counter is one inch in diameter, four inches in active length, and is filled to a pressure of 10 atmospheres. The proportional counters surrounding the polyethylene moderator are 1/2 inch in diameter by 7 inches active length, are filled with a mixture of argon and methane, and are operated in the semiproportional region. The detection threshold on the counters is set below the pulse height corresponding to minimum ionizing particles. This experimental arrangement is a modification of the units flown previously on polar orbiting satellites (Trainor and Lockwood, 1964).

The four separate banks of five proportional counters each are operated in two coincidence arrays composed of opposite banks of counters and the outputs from the individual counters are also added serially, as shown in the diagram of the electronics system displayed in Figure 2. The output pulses

from both the add and coincidence modes are scaled and fed to the telemetry, as well as being used to trigger a uni-vibrator which blanks certain neutron channels. The blanking time is set for 200 μ sec, which is greater than three times the half-life of the neutrons in the detecting system. Within the add mode circuit a binary stage provides an additional 200 μ sec of blanking time to discriminate against two charged particle events occurring within 200 μ sec. Outputs from the total and the coincidence-gated modes of the He^3 counter are scaled and fed to the telemetry system. We shall designate the raw or total neutron counting rate as N_T , the neutron rate gated by the counting rate of the total charged particle shield as N_{GT} , and the neutron rate gated by the charged particle coincidence banks as N_{GC} (see Figure 2).

The design of the neutron detector and its location in the vehicle were based upon minimizing the effects of local production of neutrons. The neutron detector assembly is located as far forward as possible, away from dense and hydrogenous materials in which neutrons might be produced. The clamshell nose-cone section, which surrounds the detector, illustrated in Figure 3, is jettisoned above the atmosphere to remove this source of local neutron production. Since the neutron sensor is oriented with its long axis parallel to the spin axis of the rocket and is far forward, the solid angle subtended at the detector by the main rocket payload is small.

Since the charged particle shield does not completely surround the neutron detector, we may expect a small contribution from neutron production by charged particles leaking in the ends of the sensor. For an isotropic charged particle flux we estimate from geometrical considerations that this contribution is six percent. Furthermore, the charged particle counters do not overlap each other around the neutron detector so about five percent of the charged particles entering the sides will escape detection. Since the neutron detector is disabled for 200 μ sec every time a charged particle is detected by the proportional counters, the difference $N_T - N_{GT}$ represents an upper limit to the neutron production by charged particles. This difference should be increased by about 10 percent to take into account the fraction of charged particles leaking through the sides and ends. This is neglected because of the large statistical errors (see Table 4). Neutron production effects for different parts of the rocket payload were calculated and are evaluated in terms of measured production (to be discussed later).

With the charged particle anticoincidence shield used in this experiment, corrections might be necessary for the self-gating rate. An energetic neutron ($E > 50$ Mev) entering the moderator can produce a proton recoil or a reaction with one or more charged particle fragments. The secondary charged particle can then turn off the neutron detector for at least 200 μ sec. The total number of such interactions has

been calculated, assuming the Lingenfelter neutron energy spectrum ($E_n > 50$ Mev) and the measured total neutron cross-section in polyethylene. We estimate the charged particle counting rate to be $\leq 1 \text{ sec}^{-1}$, which introduces a deadtime correction of ≤ 0.1 percent.

Calibration of the Neutron Detector

The detecting system was calibrated by exposing the complete detector assembly to known fluxes of gamma rays and neutrons. The gamma-ray response of the detector was measured with a calibrated Co^{60} source and was found to be negligible for all payloads. Calibrated Ra-Be, Am^{241} -Be, Am^{241} -mock fission, and Am^{241} -Li neutron sources were used, as well as 14.4 Mev and 2.7 Mev neutrons produced by a 400 Kev Van de Graaff accelerator. The accelerator-produced neutron fluxes were checked against the calibrated neutron sources with a standard long counter (Hanson and McKibben, 1947). The associated particle technique was also used to measure the neutron flux from the (d,t) reaction (Marian and Fowler, 1960). The neutron flux produced at the target in the Van de Graaff accelerator room was viewed through a hole so located in the room shielding that the effects of neutron scattering were minimized. The remaining background of low energy neutrons from room scattering was subtracted out in all runs. The calibrations with the radioactive neutron sources were made with both the source and the detector assembly at least twenty feet above the

ground to minimize the contributions from scattered neutrons. Careful measurements were made of the effect of the scattered neutrons at different elevations above the ground with different water content in the ground. We believe that the uncertainty in the absolute calibration for any neutron source is less than 10 percent, based upon the known accuracy for the source strength, effects of scattering, and statistical errors. Where the neutron energy spectrum from the radioactive sources extends over a considerable range, e.g. Ra-Be or Am-Be neutron sources, the efficiency was determined for the average energy of the neutron spectrum by an iterative process. To calibrate the neutron detector at thermal energies, a bare identical He^3 counter was first calibrated at the thermal neutron facilities of the Portsmouth Naval Shipyard. This counter was then used as a standard to measure (by the cadmium difference technique) the thermal flux in a large paraffin moderator constructed around the target of the accelerator into which the flight detector was placed.

The neutron energy calibration is summarized in Figure 4. For the calibrations made with neutron sources, we have indicated the energy range in which 50 percent of the neutrons are found. Since no energy calibrations were made between 3×10^{-2} and 4.8×10^5 ev, the response functions of Fraki et al. (1963) for a BF_3 counter with a one inch polyethylene moderator were normalized (open circles in Figure 4) to the smooth curve drawn through the experimental calibration data for $2 < E_n < 15$ Mev.

The solid curve in Figure 4 is the best fit to both our calibrations and the normalized response functions of Fraki et al. The dotted curve is an extrapolation of $S(E)$ at 340 and 4.9 ev to thermal energies. Such a large difference in the response below 10 ev introduces only a two percent change in the mean efficiency of the detector because such a small fraction of the neutron leakage lies in this energy interval. The error bars indicated in Figure 4 take into account the uncertainties in absolute calibration of the neutron sources (natural and accelerator-produced), and in the response of the long counter with neutron energy, as well as errors from subtracting the background of scattered slow neutrons and from statistics. The largest source of error is, of course, in determination of the absolute neutron flux. The standard deviation of the individual calibration points from the smooth curve in the interval $2 < E_n < 15$ Mev is 15 percent, which may be used as an estimate of the accuracy of $S(E)$ in this interval. The largest uncertainty in the calibration is 20 percent at $E_n \approx 0.5$ Mev. The directional response of the complete sensor, measured at 2.7 Mev, is shown in Figure 5.

The charged particle counter system was not calibrated. The calculated geometrical factor for the charged particle counters operated in the add mode is $G_0 = 175 \text{ cm}^2$, assuming that the proportional counters are 100 percent efficient (Vouk, 1947). From the rocket flight at Natal, Brazil, (vertical cutoff rigidity $P_c = 13$ Gv) in March 1967, we used the known

primary cosmic-ray flux to find the geometrical factors for the charged particle counters operated in the add and coincidence mode. The ratio of the charged particle counting rate, R , to the integral primary cosmic-ray flux, J , (including the albedo flux) is EG_0 , where the efficiency of the counters, E , is assumed to be 1.0 and G_0 is the geometrical factor for the detector array. From the data of Webber (1967) the primary flux, including splash and reentrant albedo, is 405 ± 40 particles/m² sec ster. Hence, $G_0 = R/J = 185 \text{ cm}^2$ for the add mode and 17.5 cm^2 for the coincidence arrangement, assuming 2π isotropy for the primary and albedo flux. The calculated energy thresholds for electrons and protons are listed in Table 1.

Table 1: Energy thresholds for charged particle counters in the He³ neutron detector system

	<u>NOSE CONE ON</u>		<u>NOSE CONE OFF</u>	
Total (add mode)	electrons	protons	electrons	protons
$(EG_0) = 195 \text{ cm}^2$	5 Mev	50 Mev	1.3 Mev	20 Mev
Coincidence				
$(EG_0) = 18 \text{ cm}^2$	~25	90	20	75

We can use the calibration curve in Figure 4 and the directional response function shown in Figure 5 with an assumed energy spectrum for the neutron leakage flux to convert the counting rates to a neutron flux. If the differential

neutron flux in neutrons/(cm² sec Mev) is given by $N(E)$ and the response of the detector in counts/neutron cm² is $S(E)$, the mean response of the detector is:

$$\bar{S} = \frac{\int N(E)S(E)dE}{\int N(E)dE} \quad (10-1)$$

Assuming Lingenfelter's spectrum at 0°, 40°, and 90° geomagnetic latitudes (Lingenfelter, 1963) we calculate \bar{S} to be 3.6, 3.7 and 3.6 cm² respectively, with an uncertainty of <15 percent. The Lingenfelter neutron leakage flux and relative contributions to the counting rate of the detector from the different energy ranges at 0°, 40°, and 90° geomagnetic latitudes are listed in Table 2. From this table we see that a 20 percent error in $S(E)$ in the interval $0.1 < E_n < 1$ Mev introduces about 10 percent uncertainty in \bar{S} . In other energy ranges the experimental errors in $S(E)$ introduce much smaller uncertainties in \bar{S} . Hence, the 15 percent error assigned to \bar{S} is quite conservative.

Experimental Results

The rocket flight results are summarized in Table 3. The first five payloads were carried on Nike-Apache vehicles to a maximum altitude of 140 km, the last three payloads were flown on Nike Tomahawks to about 350 km. The neutron counting rates were averaged over the flight time above the altitude at which the nose cone was ejected: 45 km (150 k ft) and 180 km (600 k ft) for the Apache and Tomahawk vehicles respectively. The flight times for data acquisition were then 300 and 500 sec. respectively. The neutron data listed in Columns A and B have

TABLE 2: RELATIVE CONTRIBUTIONS TO THE NEUTRON COUNTING RATE FOR THE LINGENFELTER
NEUTRON LEAKAGE SPECTRUM AT $\lambda = 0, 40$ and 90° .

Neutron Energy (Mev)	Ratio $\frac{N(90^\circ)}{N(0^\circ)}$	Total Calculated Neutron Leakage Flux, N(%)			Counting Rate of Neutron Detector (%)			$\bar{S}(E)$ for Energy Interval		
		0°	40°	90°	0°	40°	90°	0°	40°	90°
$10^{-8} - 10^{-4}$	12.5	4.7	5.8	4.7	5.9	7.2	6.0	4.6	4.6	4.6
$10^{-4} - 10^{-2}$	10.5	8.0	9.2	7.2	11.3	12.8	10.5	5.2	5.2	5.2
$10^{-2} - 10^{-1}$	9.4	8.3	9.4	7.1	12.3	13.7	10.7	5.4	5.4	5.4
$10^{-1} - 1$	12.0	39.9	39.5	40.5	48.6	46.7	49.6	4.5	4.4	4.4
1 - 5	12.0	29.6	26.8	30.4	18.0	16.7	19.7	2.2	2.3	2.3
5 - 10	24.0	3.7	6.4	7.4	2.1	2.3	2.7	2.1	1.3	1.3
10 - 10^2	6.3	5.8	2.9	2.8	1.7	0.7	0.8	1.1	1.0	1.0
SUM							$\bar{S}(E)$	3.65	3.71	3.57

not been normalized for differences in calibration nor changes in the intensity of the cosmic radiation between February, 1965, and June, 1967. In Column C we have listed the normalization factors determined from intercalibration of the payloads with an Am-Be neutron source. For determining the relative cosmic-ray intensities at flight times, both the total charged particle counting and the coincidence rates are given.

Since the flights in 1966-1967 were after the minimum in solar activity and the cosmic-ray flux had declined, the neutron data were normalized to solar minimum. The Mt. Washington neutron monitor was used to indicate the cosmic-ray intensity level and it was assumed that at any latitude the change in neutron leakage flux calculated by Lingenfelter (1963) was a linear function of the cosmic-ray intensity. These normalization factors are listed in Table 3, Column F. Only flights 5 and 8 required large normalization. The values shown in Column G are the normalized neutron counting rates obtained by multiplying the N_{GT} (Column B) by the normalization factors for intercalibration (Column C) and for the change in cosmic-ray intensity (Column F). Only on flight 8 was a deadtime correction necessary for the neutron rate gated by the total charged particle rate. This correction is included in the value tabulated for flight 8 in Column G. The gated neutron rates were converted to neutron leakage fluxes at the different latitudes using equation (10-1).

In Figure 6 we have plotted the neutron rate gated by the total charged particle rate (N_{GT}) averaged over the flight

TABLE 3 SUMMARY OF NEUTRON MEASUREMENTS

Flight No.	Launch Date	Geographic Lat./Long.	Geomag. Lat.	P _c Gv	A Total Neutrons N _T (Sec) ⁻¹	B Neutrons Gated by Add NGA N _{GT} (Sec) ⁻¹	C Normalization Factor for Inter-calibration	D Total Charged Particles (Sec) ⁻¹	E Coincidence Rate (Sec) ⁻¹	F Normalization for Change in Cosmic Ray Intensity ⁺⁺	G Neutron Rate (Normalized) (Sec) ⁻¹	H Neutron Flux (cm ² Sec) ⁻¹	Relative Mt. Washington Neutron Monitor Rate
1	Feb 3 65	37°59'N 75°29'W	49.4°N	2.2	2.68±0.11 [*]	2.45±0.10 [*]	0.80	157±1 [*]	6.9±0.2	1.00	2.0	0.54±0.08 ^δ	99.5
2	Apr 2 65	12°07'S 78°13'W	0.5°S	13.5	0.50±0.05	0.43±0.07	0.83	47.8±0.4	4.3±0.2	1.00	0.36	0.10±0.02	98.4
3	Apr 5 65	30°38'S 75°02'W	19°S	12.0	1.18±0.05	1.08±0.05	0.72	52.5±0.5	4.6±0.2	1.00	0.77	0.21±0.03	98.9
4	Apr 13 65	60°00'S 78°00'W	48.5°S	4.2	3.70±0.18	3.54±0.17	0.77	104±1	6.0±0.2	1.00	2.74	0.76±0.11	99.6
5	Aug 24 66	58°45'N 94°05'W	~70°N	<0.2	3.24±0.12	2.42±0.12	1.00	256±3	13.3±0.1	1.35±0.10	3.1	0.87±0.12	91.0
46	Nov 30 66	37°59'N 75°29'W	49.4°N	2.2	2.42±0.10	1.64±0.07	0.82	98±1	4.1±0.1	1.07±0.02	1.45	0.39±0.06	93.8
47	Mar 27 67	05°13'S 36°00'W	~0	13.2	0.34±0.03	0.22±0.02	0.95	51±2 ^{**}	4.5±0.4	1.02±0.02	0.25	0.07±0.01	93.0
48	Jun 7 67	58°45'N 94°05'W	~70°N	<0.2	5.67±0.17	2.65±0.12	0.75	3007±0	48.8±0.2	1.43±0.10	4.25(2.98)	1.12(0.83)	88.5

⁺ Vertical cutoff rigidities from Shea et al. (1965) ^Δ Nike-Tomahawk flights

⁺⁺ For details see text

^{*} Statistical error

^{**} Averaged over time intervals

^δ Error includes calibration uncertainty

no apparent trapped radiation

time above 200 k ft as a function of geomagnetic latitude. For comparison purposes we have normalized Lingenfelter's leakage flux to the equatorial neutron counting rate. The most probable error for each flight is indicated by the error bar. This error includes the statistical uncertainty, the intercalibration and normalization errors, the uncertainty in the elimination of neutron production in the moderator assembly and in the calculation of the production in the rocket vehicle. Except for the flights at $\lambda = 70^\circ$, the statistical error is at least one half the most probable error. Flights 3 and 4 at 19° and 48.5° geomagnetic latitude (enclosed by the dashed lines) are about 50 percent too large which is attributed to electrical noise problems. Then electrical noise pulses could be removed because characteristically most appeared simultaneously (within 10^{-3} sec.) on all data channels. However, with the low counting rates observed, it was impossible to delete all the noise pulses from flights 3 and 4 on which large noise bursts were encountered.

Flights 5 and 8 both occurred near the minimums of Forbush decreases. Consequently, the normalization factors are large. The charged particle counting rates on flight 8 were much higher. We conclude that an appreciable flux of solar protons and helium nuclei were still present on June 7, 1967, from the low energy solar particle event on June 6, which followed a class 2B solar flare. This charged particle flux produced neutrons both in the atmosphere and in the payload.

Therefore, we cannot normalize the neutron data from flight 8 by the same method as used for the other flights. For now we will take the normalized neutron counting rate on this flight as $3.0 \pm 0.1 \text{ sec}^{-1}$ (shown in parenthesis in Column G, Table 3) and justify it in the next section.

The neutron counting rates converted to a flux by means of measured mean efficiencies for the detector are plotted in Figure 7 as a function of vertical cutoff rigidity. The flux agrees within 25 percent with Lingenfelter's calculated values at $P_c > 1.0 \text{ Gv}$ but is about one half the calculated value for $P_c < 1.0 \text{ Gv}$. The observed ratio of counting rate at latitudes greater than 60° to that at the equator is about 9 to 1, compared to the calculated latitude effect of 12 to 1.

Interpretation of Results

1. Neutron Production Effects

In measuring the neutron flux in the presence of an appreciable background of charged particles, the effects of neutron production must be carefully evaluated. The neutron production rates in different sections of the payload were calculated following a method similar to that outlined by Trainor and Lockwood (1964). Several refinements were made in the present calculations. These include: 1) the energy spectrum of the primary cosmic radiation was included rather than to assume it to be a monoenergetic source with a mean energy of 10 Gev; 2) the interactions of the primary alpha particles were included; 3) the secondary neutron production

by fast knock-on particles was evaluated; and 4) an energy distribution for the evaporation neutrons was folded into the known energy response of the detector. In these flights we have monitored certain counting rates related to production effects so that we can compare the calculated with the observed neutron production rates for different sections of the payload. These data are summarized in Table 4.

First, we can compare the difference between the neutron rates just before and after the nose cone was ejected to estimate the production of neutrons in the nose cone by galactic cosmic-rays. The measured values are listed in the next to last column of Table 4 and calculated contributions are given in the fourth column. The large errors for the measured ΔN are statistical. We conclude that neutron production from the clam-shell is negligible. It should be noted that the neutron production effects in the rocket vehicle, including the material in the mounting for the neutron sensor assembly, are comparable to those in the nose cone assembly. The vehicle production is more difficult to estimate and is not directly subject to experimental verification. Since the values for neutron production in the vehicle and nose cone assembly listed in Table 4 are upper limits, we infer that at $\lambda = 70^\circ$ these sources contribute less than 12 percent. The contributions are about the same at $\lambda = 0^\circ$.

Second, the difference between N_T and N_{GT} corrected for deadtime represents the neutron production in the moderator

TABLE 4. CALCULATED AND MEASURED NEUTRON COUNTING RATES FROM LOCAL PRODUCTION ON THE ROCKET VEHICLE

Latitude (GM)	P_c (Gv)	Calculated (Sec) ⁻¹		Vehicle	Measured $\%N_{GT}$	(Sec) ⁻¹		ΔN before and after nose cone ejection	$\%N_{GT}$
		Moderator Assembly	Clamshell Nose Cone			$(N_T - N_{GT})$	$(N_T - N_{GC})$		
>70°	<0.2	0.4 ± 0.2	0.2 ± 0.1	0.2	35	(5) 0.8 ± 0.15 (8) 1.3 ± 0.15	0.25 ± 0.2 0.45 ± 0.2	(5) 0.2 ± 0.4 (8) 0.2 ± 0.5	10
						(1) 0.2 ± 0.15 (4) 0.4 ± 0.15 (6) 0.6 ± 0.15	0.2 ± 0.15 0.3 ± 0.15 0.2 ± 0.15	(6) 0.0 ± 0.4	
50°	2.5	0.2 ± 0.1	0.10 ± 0.05	<0.2	17	(3) 0.15 ± 0.1	0.15 ± 0.1		12
20°	8.0	0.07 ± 0.04	0.04 ± 0.02	<0.1	20	(2) 0.6 ± 0.15 (7) 0.1 ± 0.05	0.10 ± 0.07 0.05 ± 0.05		20
0°	14.0	0.03 ± 0.01	.02 ± .01	<0.05	40			0.0 ± 0.1	<10

* Flight Number (Table 3)

assembly and material immediately adjacent to the neutron sensor. The calculated and observed neutron production rates in the moderator assembly listed in Table 4 are in reasonable agreement. The difference ($N_T - N_{GT}$) at $\lambda > 70^\circ$ is larger than the calculated production because neutron production effects from low energy protons ($E_p < 500$ Mev) were neglected in the calculations. There will be large contributions to the total charged particle rate at these latitudes from protons with $E_p > 20$ Mev, which will produce neutrons in the moderator assembly. Such low energy protons are not detected by the coincidence detector.

The two measured ($N_T - N_{GT}$) values enclosed by the dashed rectangles in Table 4 are questionable. On flight 2, electrical noise was present. On flight 6 the gating circuit malfunctioned. On flight 7 the 40 percent contribution of locally produced neutrons at the equator is too large. However, the statistical uncertainties are large and the contribution could be as low as $.05/.22 \approx 20$ percent. Within the large statistical errors, we conclude that the calculated and measured production in the moderator assembly agree and that production effects are very significant at $P_c \leq 1.0$ Gv.

Third, on flight 7 from Natal, Brazil, the total and coincidence counting rates of the charged particle detectors, shown in Figure 8, increased by 125 percent between an altitude of 200 km and apogee at 360 km. We can relate this increase to any observed increase in neutron counting rate, and thereby establish lower limits on the neutron production. Since the

fractional change in counting rates for the total and coincidence systems is the same, but the energy thresholds are different (for protons, 20 and 75 Mev respectively), we attribute the increase to trapped protons with $E_p > 75$ Mev.

We can convert the charged particle counting rates at 200 km to fluxes by using the geometrical factors determined from the known primary cosmic-ray flux at this latitude. Thus, if EG_0 is 195 and 17.5 cm^2 for the total and coincidence modes, the increased counting rate at apogee corresponds to 0.3 protons $(\text{cm}^2 \text{ sec})^{-1}$ with $E_p > 75$ Mev. However, $N_T - N_{GT}$, which represents the contribution to the counting rate from neutrons produced in the moderator, is independent of the increase of the charged particle rate with altitude shown in Figure 8.

Therefore, the neutron production from a proton flux ($E_p > 75$ Mev) of $0.3(\text{cm}^2 \text{ sec})^{-1}$ must be ≤ 0.1 neutron count/sec. This corresponds to 10 neutrons/sec produced in the moderator assembly, from the calculated efficiency of the neutron detector for evaporation neutrons in the moderator (Wilson, 1965). Assuming no cascading of the secondary nucleons at incident proton energies of ~ 100 Mev, the number of neutrons produced in the moderator assembly is

$$\eta = fvGJ_p \quad (16-1)$$

where η = neutrons produced/second, f = fraction of protons interacting, v = neutrons per interaction, $G = \epsilon G_0$ = geometrical factor for the detector, and J_p = protons/ cm^2 . For $J_p = 0.3 (\text{cm}^2 \text{ sec})^{-1}$, $G = 195 \text{ cm}^2$, moderator assembly thickness = 5 g cm^{-2} ,

and the known (p,n) reaction cross sections at about 100 Mev, we find $\eta = 5$ n/sec. The counting rate from this neutron production source is $.05 \text{ sec}^{-1}$, which is comparable to the statistical errors and might not be observed.

Interpretation of Results

2. June 7, 1967 Flight at Ft. Churchill

Now with some quantitative insight into the effects of neutron production, we can interpret the results of the June 1967 flight at Ft. Churchill. On this flight much higher charged particle and neutron rates were observed (Table 3) than on the August 1966 flight at the same location. For this earlier flight the charged particle rates corresponded to a cosmic-ray flux of $1.0 \pm 0.2 (\text{cm}^2 \text{sec})^{-1}$. If we normalize the primary cosmic-ray flux observations of Webber (1967) by means of the Mt. Washington neutron monitor intensity, we estimate that the primary flux on August 4, 1966, was $1.4 \pm 0.2 (\text{cm}^2 \text{sec})^{-1}$, agreeing with the measured value. However, on flight 8, the charged particle total and coincidence rates corresponded to fluxes $J_p(E \geq 20 \text{ Mev})$ 15 and $J_p(E_p \geq 75 \text{ Mev}) = 2.8 (\text{cm}^2 \text{sec})^{-1}$, but the Mt. Washington neutron monitor intensity was the same to within ± 2.5 percent. Hence, we attribute the higher counting rates to solar particles, probably associated with the solar proton event on June 6, 1967. Masley and Goedeke (1967) had observed on June 6 an absorption of 1.1 db on a 30 MHz riometer which they attribute to a 2B solar flare event. No riometer event was recorded on August 24, 1966. For this reason we take the neutron counting rate on flight 8 to be $2.98 (\text{sec})^{-1}$. This value is obtained by multiplying the

observed rate (Column B) by the normalization factor for inter-calibration and correcting for deadtime, which was approximately 50 percent. The corrected counting rate corresponds to a neutron leakage flux of $0.78 \text{ (cm}^2\text{sec)}^{-1}$. We can show by a self-consistent argument that the increased counting rate was from neutrons produced locally and in the atmosphere by low energy protons:

- a) The difference between the neutron counting rates on flights 8 and 5, normalized to the same cosmic-ray level, is $4.25 - 3.1 = 1.2 \pm 0.2 \text{ (sec)}^{-1}$ corresponding to a neutron leakage flux of $0.3 \pm .05 \text{ (cm}^2\text{sec)}^{-1}$. Since the neutron production in the moderator assembly is 50 percent greater on flight 8, we would estimate the vehicle production to be 0.3 (sec)^{-1} (see Table 4). This is comparable to the statistical error in the differences of neutron rates on flights 8 and 5, so will be neglected. If we can show that the rigidity spectrum of solar particles on June 7, 1967, was exponential, we can then use the calculated results of Lingenfelter and Flamm (1964) to determine the additional neutron leakage from solar particle production.
- b) Since the total and coincidence charged particle rates in the shield before and after the rocket nose cone was ejected have different energy thresholds for either protons or electrons (neglecting any contributions from alpha particles), we can use these counting rates to construct a crude integral spectrum. At Ft. Churchill

with $P_c \sim 0.2$ Gv, we can neglect the electron contribution to the counting rates. The four proton energy thresholds are: $E_p > 20$ Mev for the total charged particle rate, nose cone off; $E_p > 50$ Mev for the total charged particle rate, nose cone on; $E_p > 75$ Mev for the coincidence rate, nose cone off; $E_p > 90$ Mev for the coincidence rates, nose cone on. Converting the counting rates to particle fluxes from the known geometrical factors for the charged particle detecting system, the integral proton flux is plotted as a function of kinetic energy and rigidity in Figure 9. For an exponential rigidity spectrum $J = J_0 \exp(-P/P_0)$, we find that $J_0 = 700 \text{ (cm}^2\text{sec)}^{-1}$, $P_0 = 60$ Mv and $(dJ/dP)_0 = 14 \text{ (cm}^2\text{sec Mv)}^{-1}$. With this spectrum, Lingenfelter and Flamm (1964) predict a neutron leakage flux of $0.4 \pm 0.2 \text{ (cm}^2\text{sec)}^{-1}$ at this cutoff rigidity, agreeing with the observed increased neutron leakage flux. Of course, the flux is very dependent upon P_0 and the evaluation from Figure 9 is quite crude.

- c) From the riometer data (Masley and Goedeke, 1967), we estimate that the attenuation at 30 MHz on June 7, 1967, was < 0.1 db. From the vertical absorption calculations of Weir and Brown (1964), assuming the alpha to proton ratio for the solar particles to be zero, $J_0 \approx 10^3 \text{ (cm}^2\text{sec)}^{-1}$ for an exponential rigidity spectrum with $P_0 = 50$ Mv, in rough agreement with the proton spectrum estimated from the charged particle measurements.

- d) By comparing the normalized $(N_T - N_{GT})$ on flights 5 and 8 the increased production in the moderator assembly corresponded to 0.6 counts/sec, which implies a production of about 60 neutrons/sec. We can use equation (16-1) to calculate the neutron production in the moderator assembly. With $J(>P) = 700 \exp(-P/60) (\text{cm}^2 \text{sec})^{-1}$, there are about 15 protons $(\text{cm}^2 \text{sec})^{-1}$ at a mean energy of 20 Mev (200 Mv). With $v = 0.5$, $G = 195 \text{ cm}^2$, an average moderator thickness $\delta = 5 \text{ g cm}^{-2}$ and $\sigma = 0.2 \text{ b}$ for the cross section of neutron production in a mixture of aluminum and carbon, the production in the moderator assembly is

$$\eta = f v G J_p = \delta \frac{N_o}{A} \sigma v G J_p = 50 \text{ n/sec.}$$

This estimate agrees with the measured extra neutron production in the moderator assembly.

Therefore, we conclude that the excess neutron leakage flux observed on June 7, 1967, was due to neutrons produced by low energy solar particles. This observation is supported by the results of Chupp et al. (1967) and Smith et al. (1962) on neutron production in the atmosphere by solar particles.

Discussion

We have summarized recent measurements of the total neutron leakage flux in Figure 10. The measurements of Bame et al. (1963), Trainor and Lockwood (1964) and the present ones were made above

the atmosphere; the others are extrapolated from $<10 \text{ g cm}^{-2}$ altitude. The measurements of Holt et al. (1966) are of the fast neutron flux ($1 < E_n < 10 \text{ Mev}$) at $\sim 4 \text{ g cm}^{-2}$ extrapolated to the top of the atmosphere. We have converted their measurements at solar minimum to a total neutron leakage flux by using the calculated fraction of 1-10 Mev neutrons to the total flux at different latitudes (Lingenfelter, 1963). Both the data of Trainor and Lockwood (1964) and the present data have been normalized to solar minimum. Other measurements were made near solar minimum so that they were directly comparable. It is interesting to compare the recent leakage flux value obtained by Intrilligator (1968) from extrapolation of the neutron flux at an altitude of 4 g cm^{-2} at $\lambda = 42^\circ \text{ N}$ with the rocket flight measurements here. The neutron leakage flux determined directly at $\lambda = 49^\circ$ is $(0.46 \pm 0.07) \text{ cm}^{-2} \text{ sec}^{-1}$ (see Table 3). Using Lingenfelter's latitude dependence for the neutron leakage flux, we obtain $(0.31 \pm 0.06) \text{ cm}^{-2} \text{ sec}^{-1}$ at $\lambda = 42^\circ$ in agreement with $(0.36 \pm 0.06) \text{ cm}^{-2} \text{ sec}^{-1}$ obtained by Intrilligator. Except for the results of Trainor and Lockwood (1964), the agreement among measured values is good to $\sim 50^\circ$ geomagnetic latitude. (The results of Trainor and Lockwood will be discussed separately.) However, the accuracy of the data at $\lambda < 50^\circ$ is not good enough to distinguish between the two calculated leakage fluxes of Lingenfelter (1963) shown in Figure 10.

Above 50° there are large disagreements both among the experimental measurements and with the calculated fluxes. Green-

hill et al. (1965) and the present authors agree within experimental errors (+ 15%) at $\lambda > 50^\circ$. However, Greenhill et al. appear to have underestimated the contributions to the counting rate from local production at higher latitudes, so that their observations should be decreased by 10-15 percent. A normalization of the measurement in 1963 by Boella et al. (1965a) to sunspot minimum increases it from 0.58 to 0.66 $(\text{cm}^2 \text{sec})^{-1}$. Even so, it is smaller than the other values. The data of Holt et al. (1966) are much larger at high latitudes. It is not likely that these larger values arise from approximations used to extrapolate the neutron flux from the top to the outside of the atmosphere. Similar approximations were made by Greenhill et al., Boella et al., and Intrilligator (1968).

The differences in the experimental values of the neutron leakage flux at $\lambda > 50^\circ$ may be explained by the uncertainty in latitude dependence of the shape of energy spectrum in the interval 1-10 Mev. The form of the Lingenfelter spectrum is most probably correct below 0.1 Mev and above 50 Mev where the neutrons reflect directly the energy spectrum of the protons and alphas producing them. In the range $0.1 < E_n < 10$ Mev the Lingenfelter is probably most uncertain and the change with latitude not well known. Definitive experimental measurements in this interval are lacking. The results of Holt et al. (1966) at all latitudes indicate that the neutron spectrum for $0.1 < E_n < 10$ Mev is much flatter than calculated by Lingenfelter (1963). The Lingenfelter neutron leakage spectrums for $2 < E_n < 10$ Mev at $\lambda = 0, 40, \text{ and } 90^\circ$

can be written as $0.54E^{-1.83}$, $0.12E^{-1.78}$, and $0.038E^{-1.76}$ ($\text{cm}^2 \text{sec Mev})^{-1}$. If at $\lambda \geq 70^\circ$, the neutron spectrum for $1.0 < E_n < 10$ Mev were taken as $0.31E^{-1.30}$, for $10 < E_n < 100$ Mev were taken as $0.48E^{-1.5}$, and the "hump" in the spectrum at about 0.2 Mev reduced along with a 20 percent decrease in the total neutron leakage flux below 0.1 Mev, the experimental and calculated values would agree much better. The change in shape of the spectrum may be too drastic, but is closer to the present experimentally determined spectral data. The reduction in the total flux below 0.1 Mev is within estimated errors in normalizing the calculated neutron flux (Lingenfelter, 1963). The change in shape of the spectrum above 10 Mev is not important because the total leakage flux in this interval is only ~ 10 percent and the moderated detector has a small response above 15 Mev. As a result of this change in the neutron leakage spectrum, the mean efficiency \bar{S} of our detector decreases to 3.0 cm^2 , so the neutron flux increases to $1.0 (\text{cm}^2 \text{sec})^{-1}$. For this modified energy spectrum the calculated total neutron leakage flux is $1.27 (\text{cm}^2 \text{sec})^{-1}$. Since the fraction of neutrons with $1 < E_n < 10$ Mev to the total flux increases from 34 to 40 percent, the total neutron leakage flux estimated from the fast flux measurements of Holt et al. becomes $1.2 (\text{cm}^2 \text{sec})^{-1}$. Consequently, at $\lambda \geq 50^\circ$ there is agreement among the experimental values within the estimated errors and with the calculated neutron leakage flux. We do not suggest that this explanation is necessarily correct. It is a reasonable explanation until better experimental data are available on the neutron

energy spectrum in the interval 0.5-50 Mev, both inside and outside the atmosphere.

On the other hand, we interpret the very flat latitude curve obtained by Trainor and Lockwood (1964) as due to a higher background counting rate than originally estimated and too large a measured detection efficiency. With the observed neutron latitude variation of about 5 to 1, a background of 1.0 (min)^{-1} for the equatorial counting rate of 2.0 (min)^{-1} would give a corrected latitude dependence of 10 to 1. The measured efficiency may also have been about 25 percent too large. Applying these two corrections, the neutron leakage flux values essentially agree with the present results shown in Figure 10.

Conclusions

From these neutron leakage flux measurements we conclude:

1. The calculated (Lingenfelter, 1963) and measured total flux values agree for $\lambda < 50^\circ$ geomagnetic latitude.
2. Above $\lambda = 50^\circ$ the measured flux is about 60 percent of the calculated value at solar minimum.
3. At $\lambda > 60^\circ$ simultaneous measurements should be made of the neutron leakage flux, neutron and charged particle energy spectrums to separate the neutron production by galactic cosmic rays from that by solar particles.

Acknowledgments

We are grateful to Dr. E. L. Chupp for his assistance in the initial stages of this experiment and for many helpful discussions on interpreting the results. Mr. A. Sarkady designed and tested the original telemetry system for the payloads. We thank Drs. R. Houston and L. Larson for their assistance with the actual rocket flights. Without the assistance and cooperation of the National Aeronautics and Space Administration Sounding Rocket Section of Goddard Space Flight Center, the range crews at Wallops Island, Ft. Churchill and on the S. S. Croatan, these flights would not have been possible. The Brazilian Air Force, operating the Natal rocket range in Brazil was most helpful. Technical assistance was provided by Messrs. D. Schow, R. Simmons, E. Noble, and D. Meeker. Mrs. S. Dewdney assisted in data reduction. The expected neutron production in the payload and neutron detector assembly was calculated by T. Wilson.

This research was supported by the National Aeronautics and Space Administration under contract NASr-164.

FIGURE CAPTIONSFigure 1

Schematic diagram of the He^3 neutron detecting system.

Figure 2

Schematic diagram of the electronics system for the neutron and charged-particle detecting system.

Figure 3

Neutron sensor mounted on the rocket payload with clamshell nose cone open.

Figure 4

Efficiency of the He^3 neutron detector system as a function of neutron energy. Solid curve is best fit to both UNH calibrations and the response functions of Fraki et al. (1963) normalized as indicated in text.

Figure 5

Directional response of the neutron detector. 0° is perpendicular to the axis of the He^3 proportional counter.

Figure 6

The gated neutron rate above the atmosphere for eight flights. The smooth curve is the calculated neutron leakage at solar minimum (Lingenfelter, 1963) normalized to the experimental data at the equator. The data points enclosed by the dashed lines and at $\lambda = 70^\circ$ are explained in the text.

Figure 7

The measured neutron leakage flux as a function of vertical cut-off rigidity. The smooth curves are the calculated fluxes at solar minimum and maximum (Lingenfelter, 1963).

Figure 8

Coincidence counting rate vs charged particle rates at different altitudes during flight 7 from Natal, Brazil.

Figure 9

Integral proton flux as a function of rigidity deduced from the charged particle counting rates on flight 8 from Ft. Churchill. Errors indicated are statistical only. For details, see text.

Figure 10

Measured neutron leakage flux above the atmosphere as a function of geomagnetic latitude. The smooth curves are the calculated fluxes (Lingenfelter, 1963).

REFERENCES

- Bame, S. J., S. P. Conner, F. B. Brumley, R. L. Hostetler, A. C. Green, Neutron flux and energy spectrum above the atmosphere, J. Geophys. Res. 68, 1221-1228, 1963.
- Boella, G., G. Degli Antoni, C. Dilworth, L. Scarsi, G. Pizzi, and M. Tagliabue, Latitude effect on neutron albedo flux, Il Nuovo Cimento, 37, 1232-1235, 1965a.
- Boella, G., G. Degli Antoni, C. Dilworth, M. Panetti, and L. Scarsi, Measurement of the cosmic-ray neutron flux at 4.16 billion volts geomagnetic cutoff rigidity, J. Geophys. Res. 70, 1019-1030, 1965b.
- Chupp, E. L., W. N. Hess, and C. Curry, The neutron flux in space after the November 15, 1960, polar cap neutron event, J. Geophys. Res. 72, 3809-3816, 1967.
- Dragt, A. J., M. M. Austin, and R. S. White, Cosmic ray and solar proton albedo neutron decay injection, J. Geophys. Res. 71, 1293-1304, 1966.
- Fraki, R., M. Leindorfer, M. and S. Malensky, The energy variation of the sensitivity of a polyethylene moderated BF₃ proportional counter, Nucl. Instr. & Methods, 23, 341-348, 1963.
- Freier, P. S. and W. R. Webber, Exponential rigidity spectrums for solar flare cosmic rays, J. Geophys. Res. 68, 1605-1630, 1963.
- Greenhill, J. G., J. Phillips, K. B. Fenton, A. G. Fenton, and M. Bowthorpe, The neutron flux in the upper atmosphere during the 1964 solar minimum, Proc. Int. Conf. Cosmic Rays, London, 1, 538-541, 1965.
- Hanson, A. O. and J. L. McKibben, A neutron detector having uniform sensitivity from 10 kev to 3 Mev, Phys. Rev. 72, 673-677, 1947.
- Hess, W. N., Van Allen belt protons from cosmic-ray neutron leakage, Phys. Rev. Letters 3, 11-13, 1959.
- Hess, W. N., E. H. Canfield, and R. E. Lingenfelter, Cosmic ray neutron demography, J. Geophys. Res. 66, 665-667, 1961.
- Hess, W. N. and J. Killeen, Spatial distribution of protons from neutron decay trapped by the geomagnetic field, J. Geophys. Res. 71, 2799-2810, 1966.
- Holt, S. S., R. B. Mendell, and S. A. Korff, Fast neutron latitude variations in the atmosphere at solar minimum, J. Geophys. Res. 71, 5109-5116, 1966.

- Intrilligator, D. S., Albedo neutron source for high-energy protons trapped in the geomagnetic field, Phys. Rev. Letters, 20, 1048, 1968.
- Kellogg, P. J., Possible explanation of the radiation observed by Van Allen at high altitudes in satellites, Nuovo Cimento 10, 11, 48-66, 1959.
- Lingenfelter, R. E., The cosmic ray neutron leakage flux, J. Geophys. Res. 68, 5633-5639, 1963.
- Lingenfelter, R. E. and E. J. Flamm, Neutron leakage from interactions of solar protons in the atmosphere, J. Geophys. Res., 69, 2199-2207, 1964.
- Marian, J. B. and J. L. Fowler, Fast neutron physics, Part I: Techniques, 625-628, Interscience Pub. Inc., N.Y., 1960.
- Masley, A. J. and A. D. Goedeke, The 1966-1967 increase in solar cosmic ray activity, 10th Int. Conf. on Cosmic Rays, Calgary, Canada, 1967.
- Newkirk, L. I., Calculation of the low-energy neutron flux in the atmosphere by the S_n method, J. Geophys. Res. 68, 1825-1833, 1963.
- Shea, M. A., D. F. Smart, and K. G. McCracken, A study of vertical cutoff rigidities using sixth degree simulations of the geomagnetic field, J. Geophys. Res. 70, 4117-4130, 1965.
- Singer, S. F., Trapped Albedo theory of the radiation belt, Phys. Rev. Letters 1, 181-183, 1958.
- Smith, R. V., L. F. Chase, W. L. Iuhof, J. R. Reagan, and M. Walt, Radiation measurements with balloons, ARL-TDR-622, 6571, 1962.
- Trainor, J. H. and J. A. Lockwood, Neutron albedo measurements on polar orbiting satellites, J. Geophys. Res. 69, 3115-3123, 1964.
- Vouk, V., Projected area of convex bodies, Nature 162, 330, 1948.
- Webber, W., The spectrum and Charge composition of the primary cosmic radiation, Handbuch der Physik 46-2, 181-264, Springer-Verlag, Berlin, 1967.
- Weir, R. A. and R. R. Brown, On the contribution of solar-flare alpha particles to polar cap absorption events, J. Geophys. Res., 69, 2193-2197, 1964.
- Wilson, T. E., Production corrections to cosmic ray neutron albedo measurements, M. S. thesis, 1965.

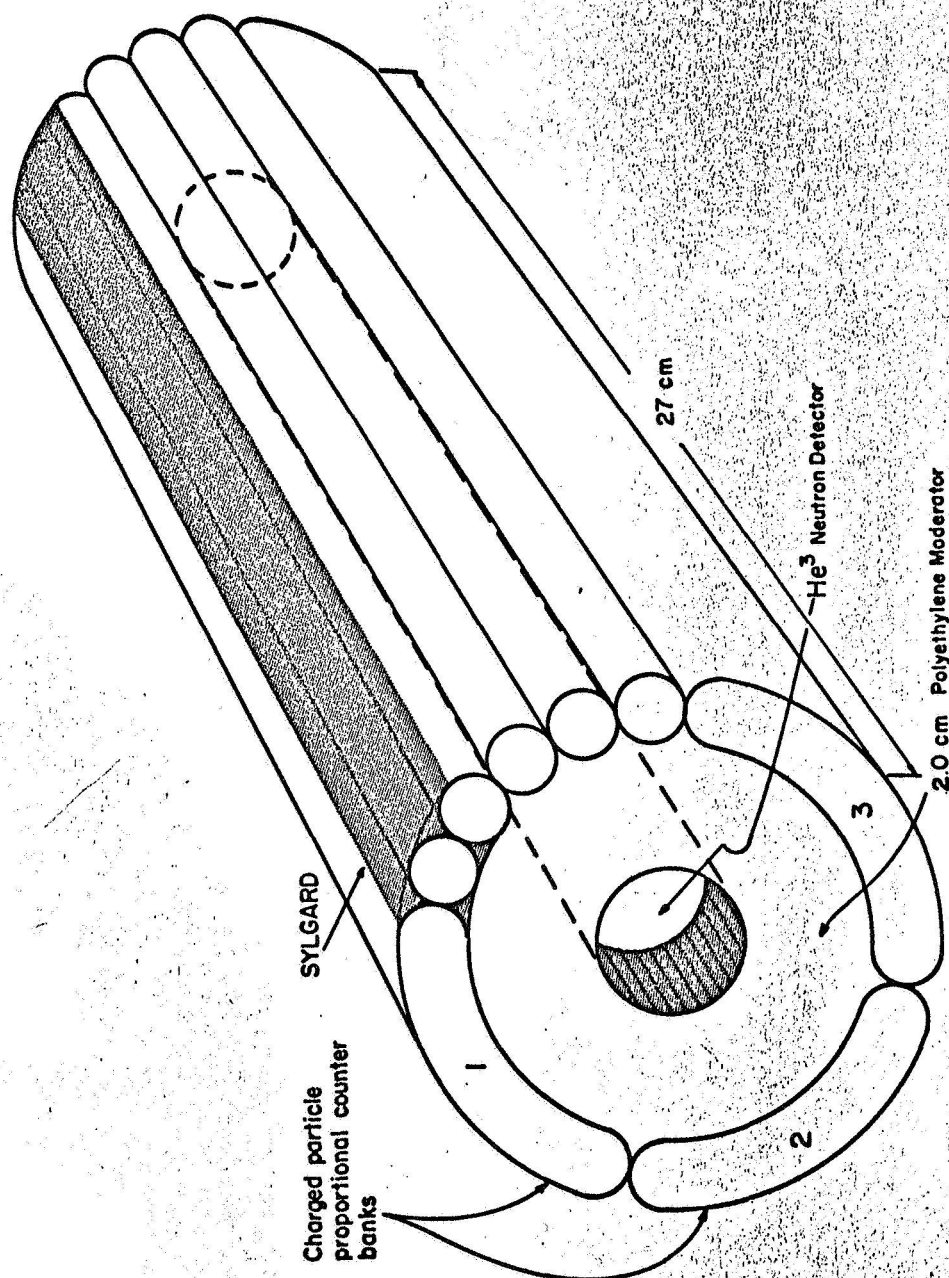


FIGURE 1

ELECTRONICS FOR NIKE-APACHE NEUTRON EXPERIMENT

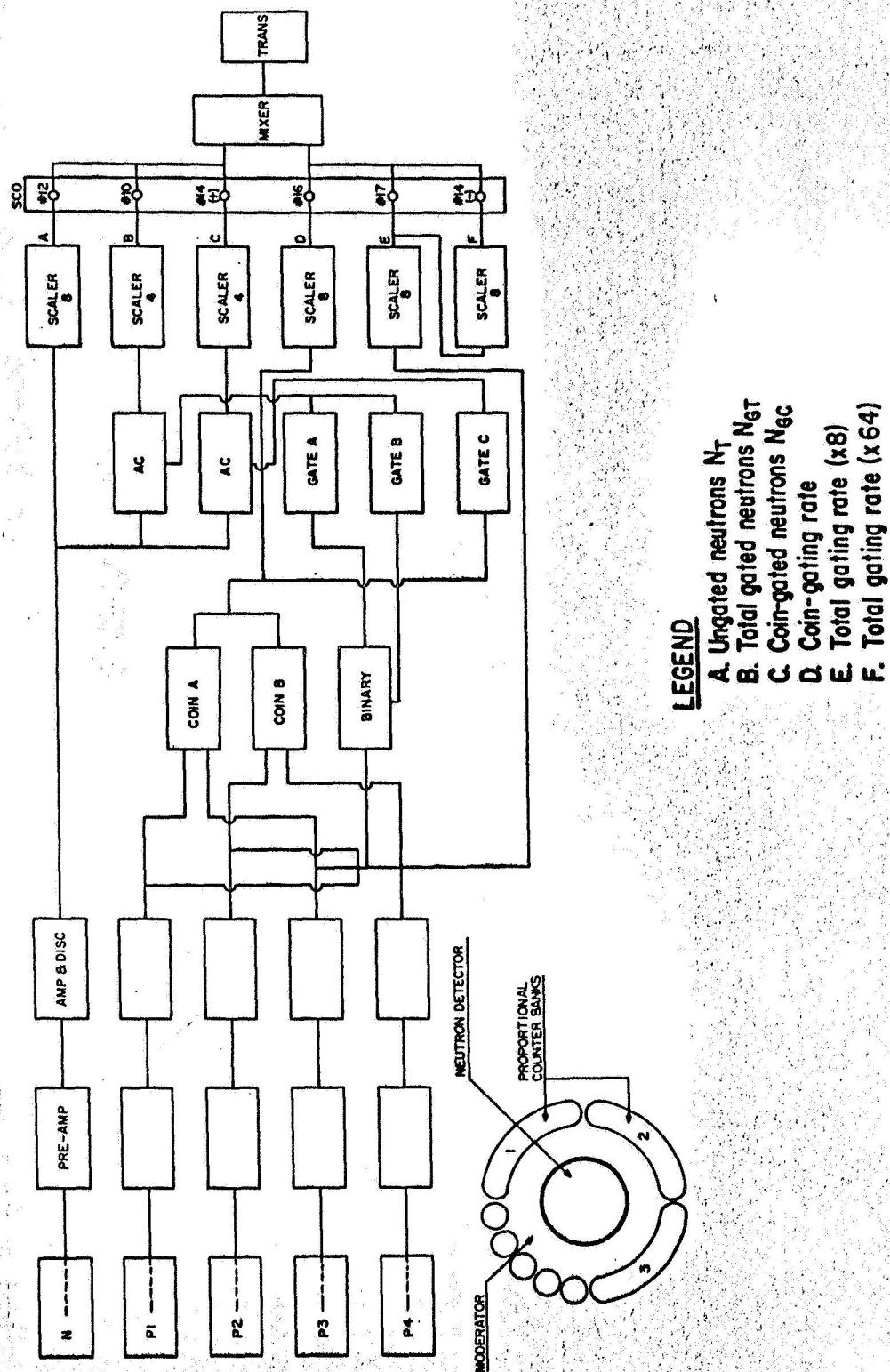


FIGURE 2

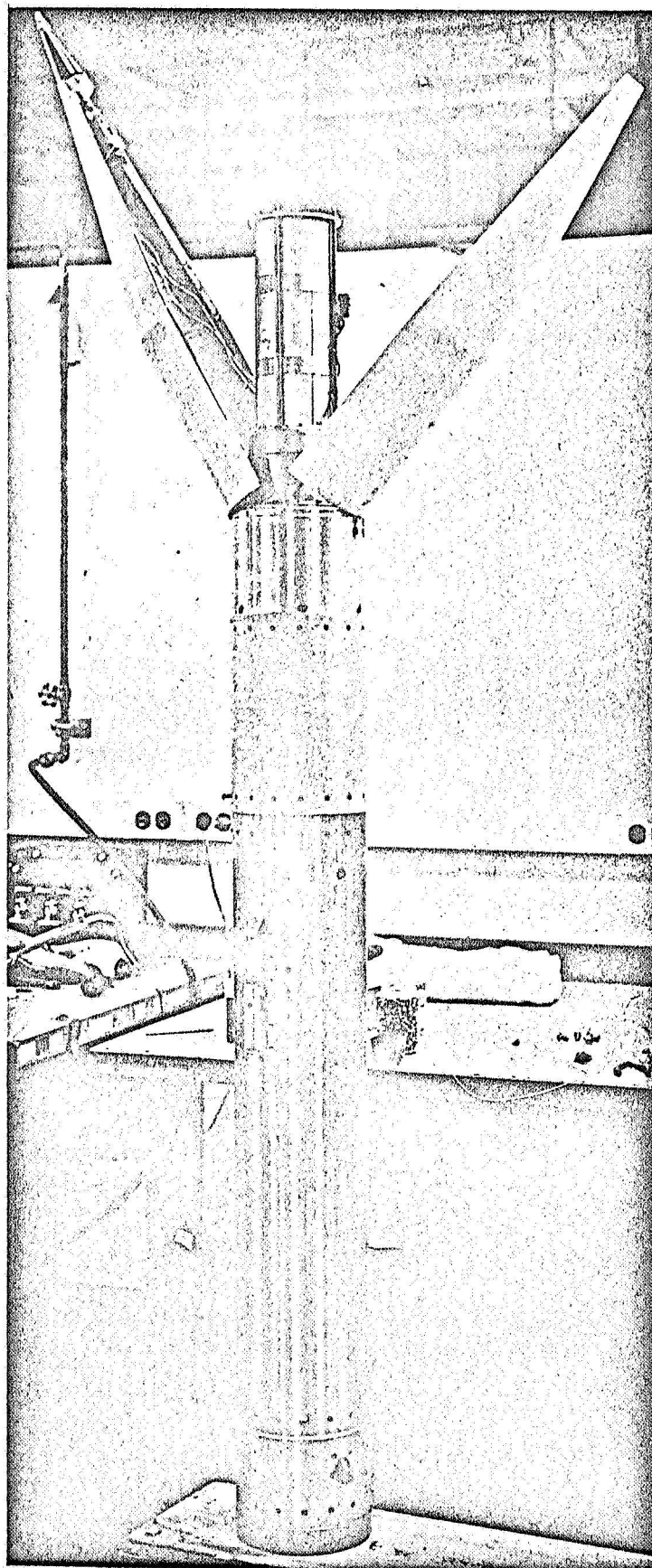


FIGURE 3

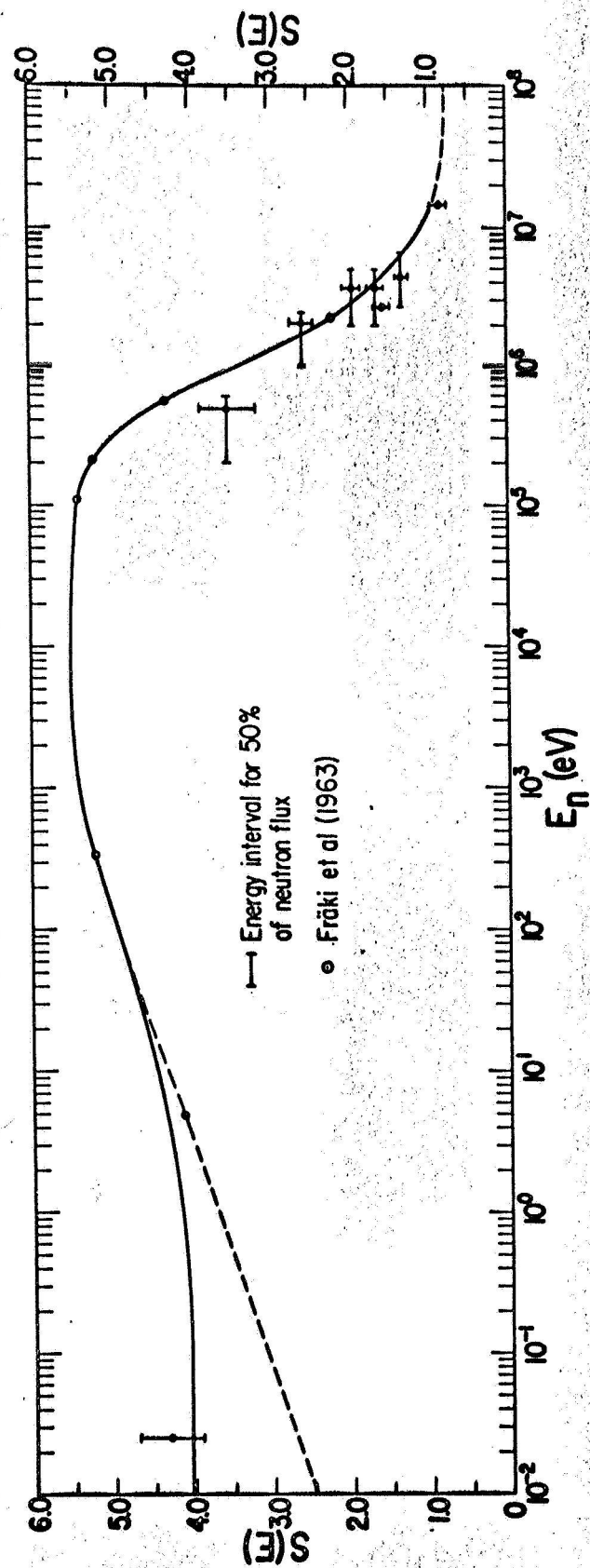


FIGURE 4

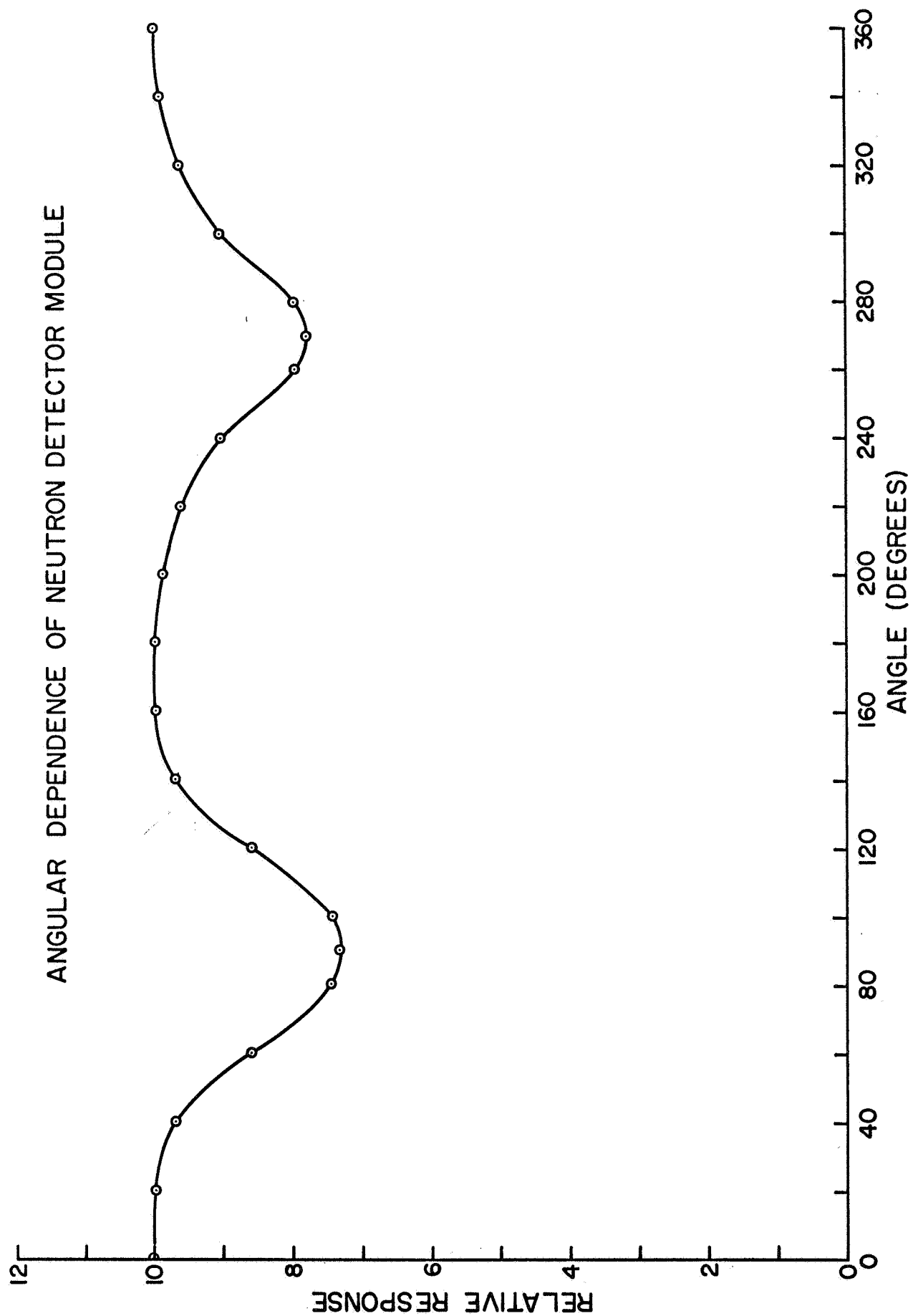


FIGURE 5

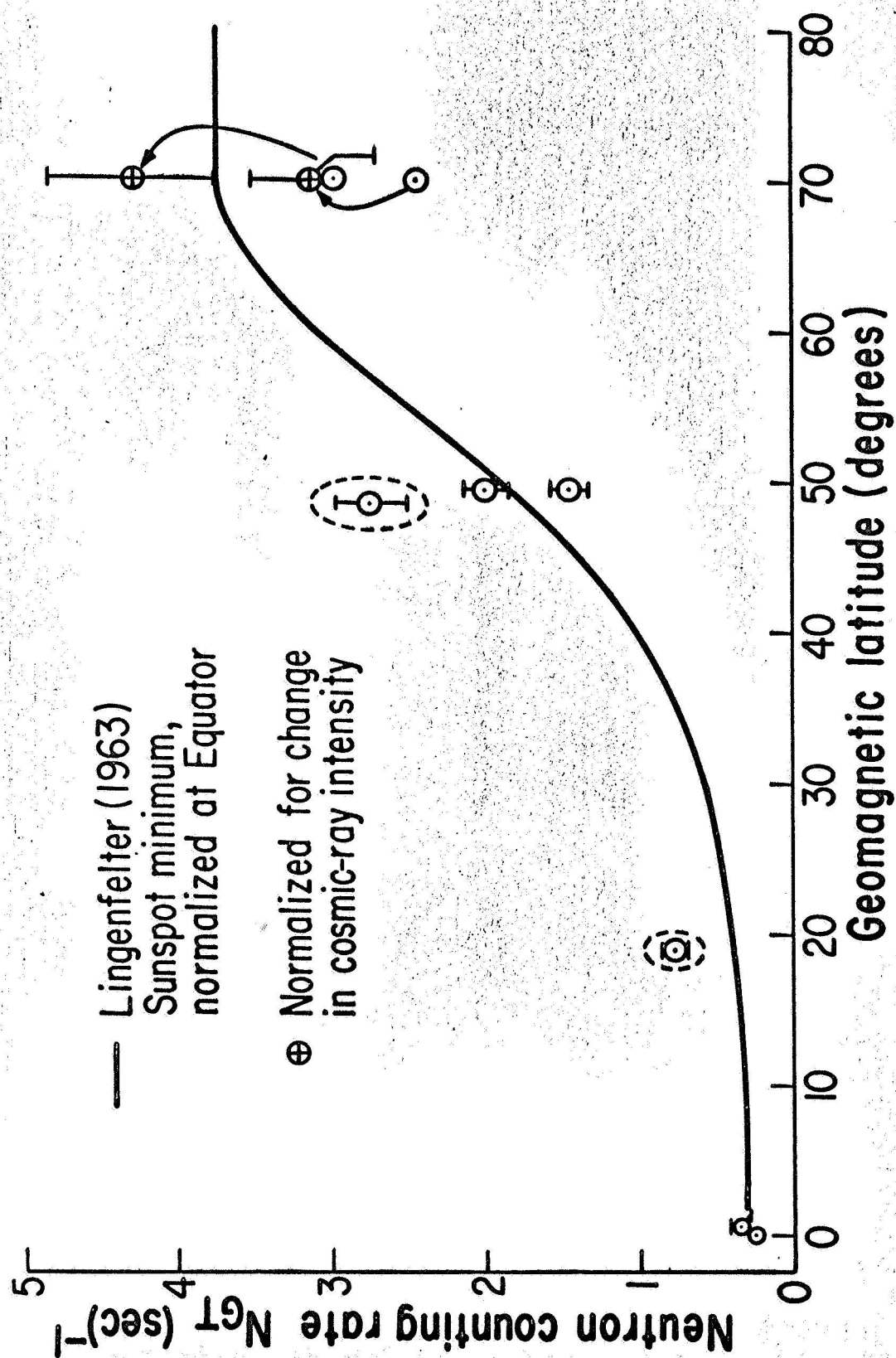


FIGURE 6

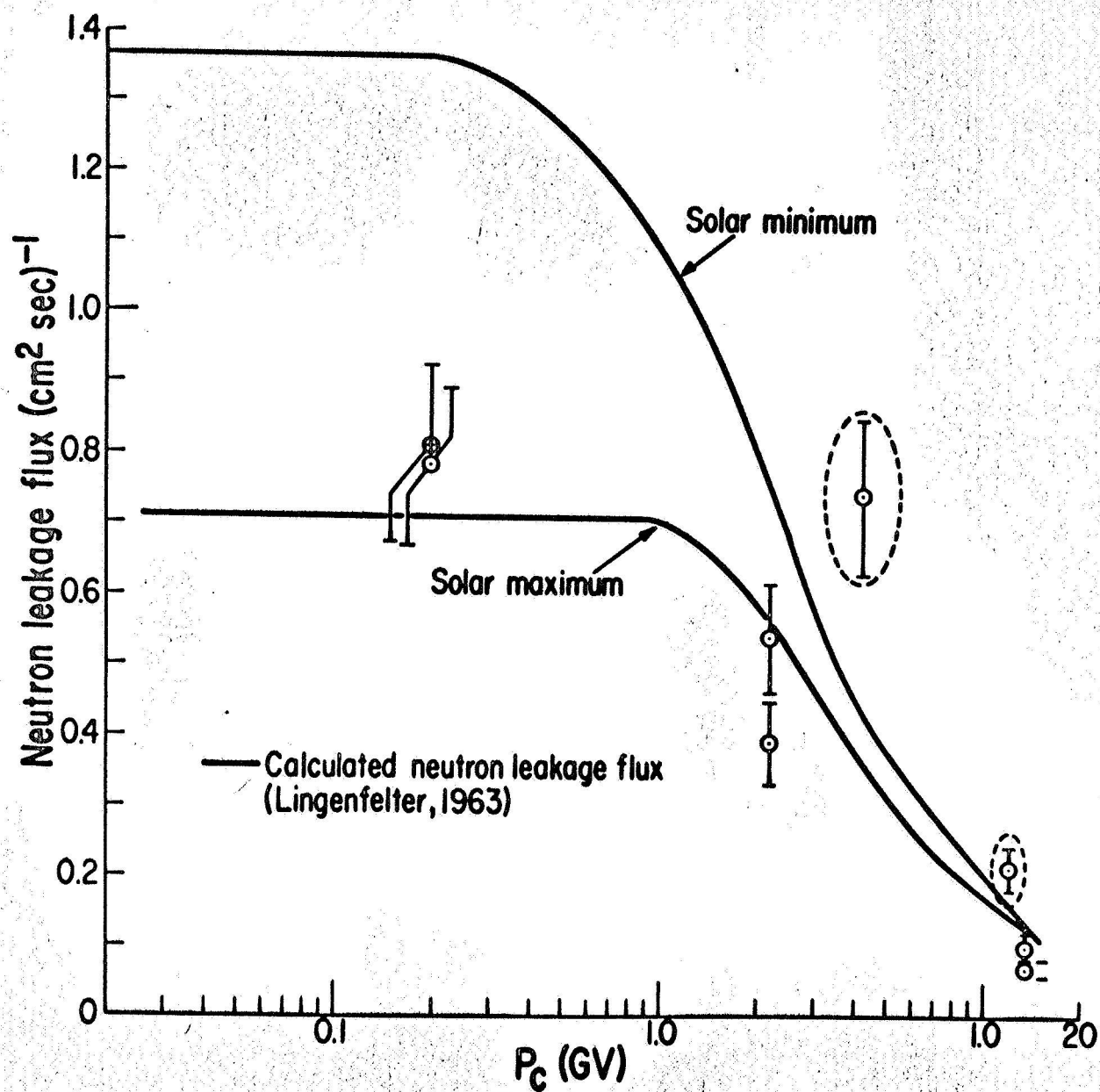


FIGURE 7

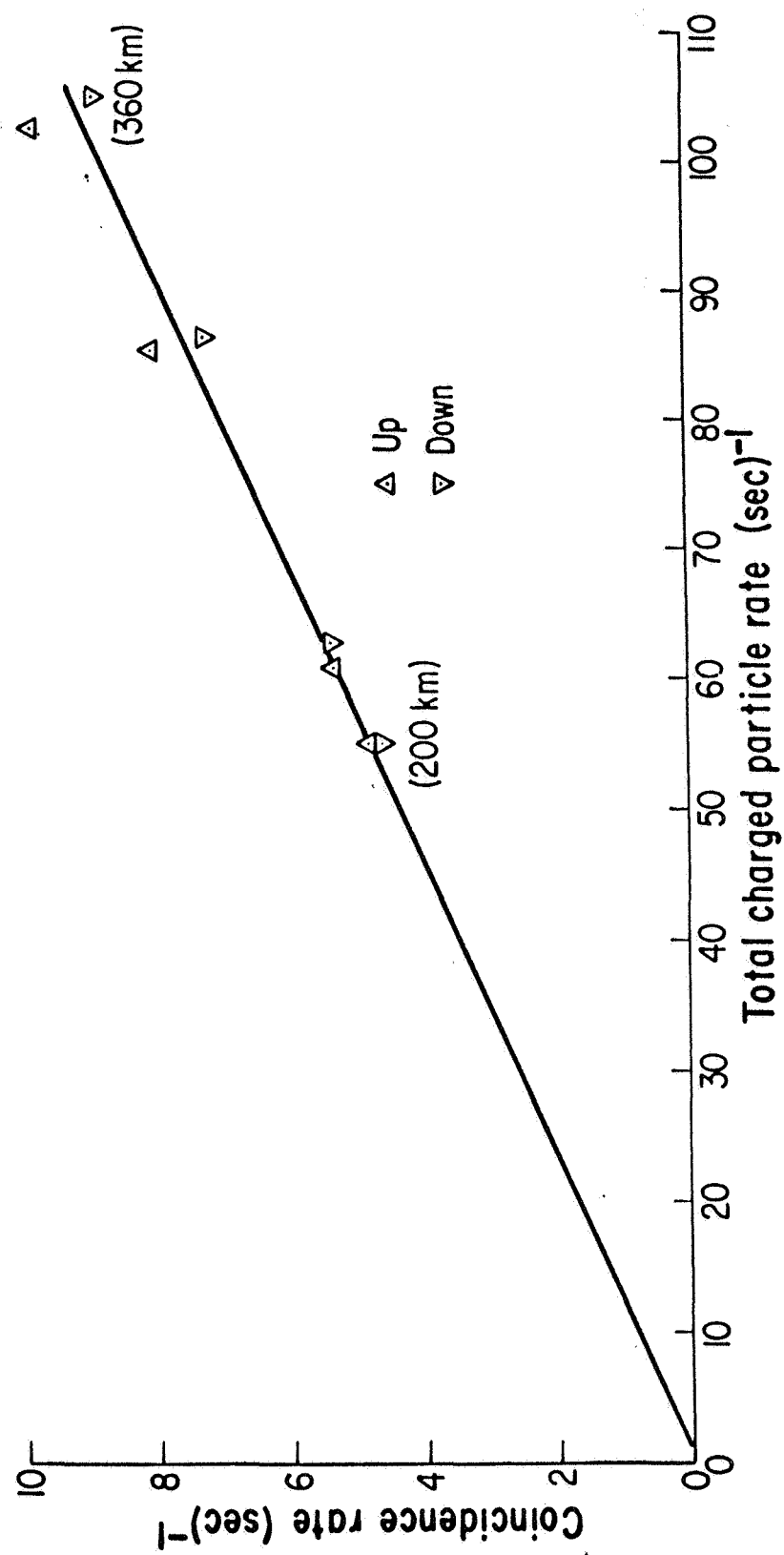


FIGURE 8

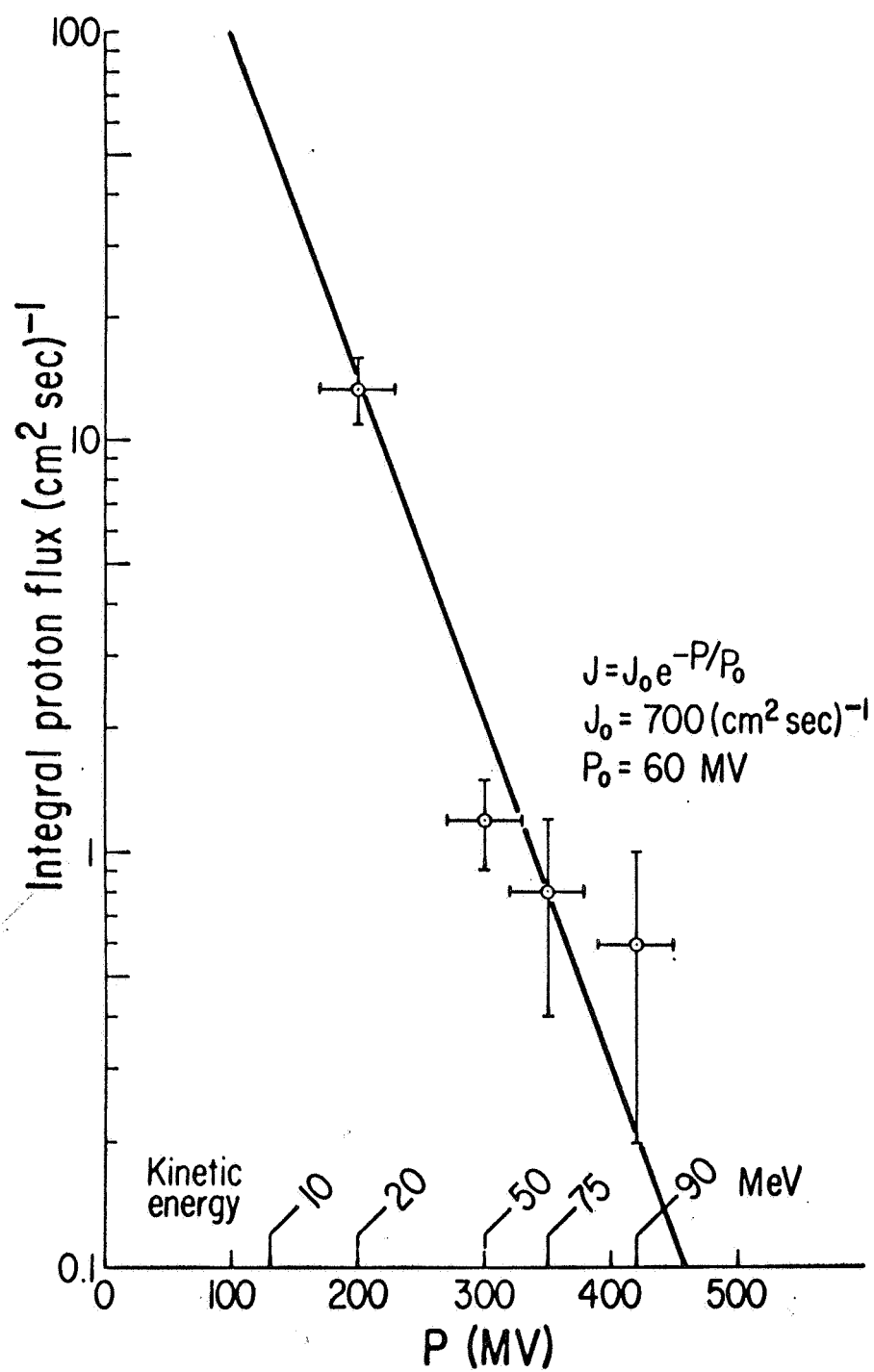


FIGURE 9

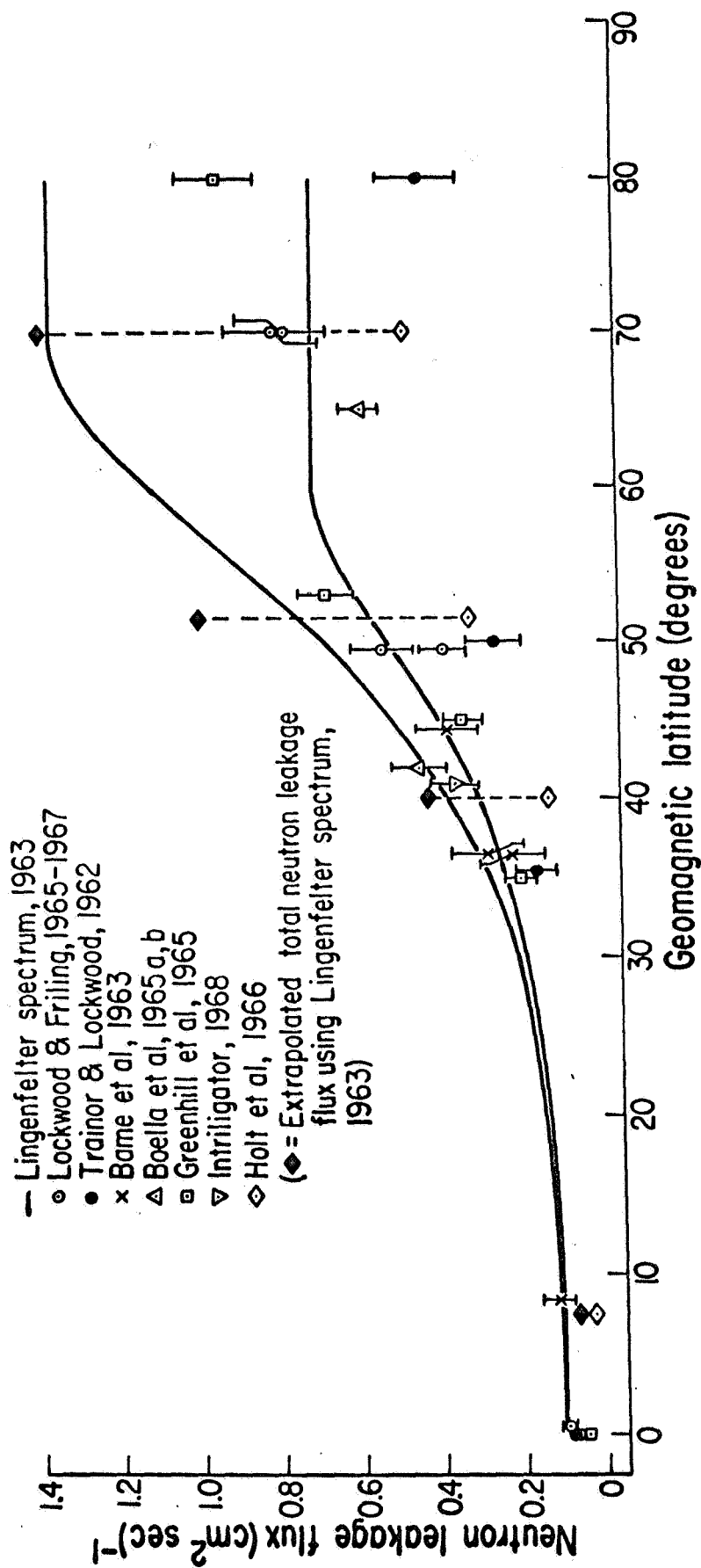


FIGURE 10

A FAST NEUTRON-GAMMA DETECTOR FOR SPACE RESEARCH

A FAST NEUTRON-GAMMA DETECTOR FOR SPACE RESEARCH*

R. N. St. Onge and J. A. Lockwood
University of New Hampshire
Physics Department
Durham, New Hampshire

Summary

The unique features of this instrument are the following:

- 1) The charged particle shield (NE 102) uses only two P. M. tubes.
- 2) The 4π charged particle shield encloses completely the neutron-gamma detector, all P. M. tubes and associated sensor electronics.
- 3) The pulse shape discriminator (P. S. D.) is passive and miniature, with "M">3.1 at the Co⁶⁰ Compton edge.
- 4) The separate spectra of neutrons ($1 < E_n < 20$ Mev) and gammas ($1 < E_\gamma < 7$ Mev) are extracted.
- 5) The I. F. C. (4% resolution) with P. S. D. on NaI(Tl & Am²⁴¹) is also displayed with (4).
- 6) The quality of data is checked by parity bits, and data are transmitted by a parallel, redundant FM-FM TM system.

Introduction

Attempts to evaluate the cosmic-ray neutron albedo theory as a source for the energetic protons trapped in the earth's radiation belts suffer from a lack of experimental data on the fast neutron flux at the top of, and above, the atmosphere. Recent experimental evidence of the absence of energetic alpha particles in the trapped radiation emphasizes the importance of absolute measurements of the fast neutron leakage flux.¹ The significance of gamma ray measurements in the Mev energy range has been cited in the literature.²

We have designed a recoil proton fast neutron-detector

*Supported by the National Aeronautics and Space Administration under contract NASr-164

system using pulse shape discrimination, with a 4π charged particle anticoincidence shield, to measure the neutron flux in range 1-20 Mev, and the gamma ray flux from 1-7 Mev.

The neutron detector, as shown in Figure 1, is a 5 x 5 cm. cylindrical NE 213 liquid scintillator with glass walls, wrapped with crinkled aluminum foil for optimum light collection. The neutron detector, associated electronic circuitry, and high voltage power supplies are enclosed within a 4π plastic scintillator shield (NE 102) which rejects all energetic charged particle events that could produce neutrons in the detector system.

The shield, consisting of two hemispherical domes and a straight cylindrical section, is designed to optimize the light collection from minimum ionizing events by using photomultipliers (P. M.) with bi-alkalide hemispherical photocathodes (RCA-C70132A) inserted into the plastic scintillator (Figure 1). A parallel summing and coincidence circuit between the outputs of two photomultipliers insures a rejection ratio exceeding $10^4/1$. This rejection ratio for the 4π scintillator eliminates the possibility of counting neutrons or gammas produced by energetic charged particles. Pulse shape discrimination is used on the liquid scintillator so that neutrons can be identified and separated from gamma rays.

In this paper we shall report on the results of tests on the anticoincidence system used as a charged particle shield, the pulse shape discriminating circuit for separating neutron from gamma ray events, the on-board data processing, the telemetry, and the ground station logic systems.

Detector Systems

Charged Particle Shield

The anticoincidence system necessary to identify incident particles as either charged or neutral completely encloses the central neutron and gamma detector. Thus, the measured neutron spectrum should represent as closely as possible the true neutron flux in the atmosphere or in space. Such extreme precaution in rejecting charged particles, which can produce neutrons or gammas in the sensor system, is necessary in view of the large contributions locally produced neutrons or gammas make to the total counting rate.

Ordinarily, a large 4π shield is not used because many photomultipliers are required to detect a minimum ionizing particle interacting anywhere in the system. It is also difficult to contain many phototubes within the 4π shield without the shield size becoming so large as to be count rate limited by charged particle events. The large number of photomultipliers is required because flat-faced tubes are attached to the surface of the scintillator so that there is a rapid loss in signal strength for events at large distances from the P. M. This can be seen in Figure 2 where the P. M. signal is plotted as a function of the distance between the tube and light source. If the phototube design is changed to incorporate a photocathode which is in the direct light path rather than being located so as to require diffuse light scattering to divert some of the light into the tube, the loss in signal strength with distance to the event is reduced considerably. Therefore, we chose a hemispherically faced P. M. which could be inserted

directly into the light path, as shown in Figure 1.

The 4π shield system can essentially be viewed as a large light pipe, emphasizing the importance of primary total internal reflection, secondary spectral reflection to recapture light losses from light cones inside the total reflection angle, and adiabatic curvatures. The simplest practical system is two mating hemispheres, including only one hemispherical P. M. inserted into each scintillating dome, with a short interconnecting cylindrical section between the domes. Further, it is required that minimum ionizing charged particles passing through any part of the shield be detected; and, since for minimizing ionizing events, the energy loss in traversing the shield is directly proportional to the shield thickness at the point of entry, we can make a further modification in design to reduce light losses between the scintillation event and the photomultiplier. This design modification has the shield thickness compensatingly greater at larger distances from the phototubes. Thus, the particle generates a larger light signal farther from the photomultipliers, which compensates for the light attenuation. Since this would require a surface too complicated to be fabricated easily, a simple workable solution is to offset slightly the centers of curvature of the inside and outside surfaces of the hemispheres.

To use such a 4π shield system to the fullest advantage, the associated electronics has been designed to include parallel summing and coincidence circuits (Figure 3). Normally, each of the two P. M. tubes viewing the shield are connected to separate lower level voltage discriminators, adjusted to be just above

the phototube noise, and the output of each voltage discriminator then fed to a coincidence circuit, generating the anti-coincidence gate signal for the internal $n\gamma$ detector. If we consider the attenuation of the light pulse traversing the shield to either of the phototubes, we realize that a scintillation occurring very near one of the two tubes may fail to trigger the coincidence circuit because there is a long optical path to the other P. M. However, to minimize such events, we add a parallel summing circuit which has a voltage discriminator set to a level much higher than the threshold of the coincidence circuit. Thus, scintillations occurring near any P. M. would, because of the short associated optical path, deposit a very large signal in this near P. M. and easily trigger the voltage discriminator of the summing circuit, but possibly fail to trigger the parallel coincidence circuit. Obviously, the other extreme is a scintillation occurring midway between the two P. M. tubes, in which case simultaneous signals from the tubes would trigger the coincidence circuit, but possibly fail to trigger the voltage discriminator of the parallel summing circuit.

Neutron-Gamma Detector

Since the anticoincidence shield eliminates the charged particle component, the organic liquid scintillator must identify and separate the types of neutral particle events. This is accomplished by pulse shape discrimination of the organic liquid (NE 213). Since these neutrals are predominantly neutrons and gammas, we designed the pulse shape discriminator to allow the simultaneous extraction of the separate spectra of gamma (γ) and neutron (n) events.

Many methods of pulse shape discriminating are available in the literature, but all known methods are severely limited by the use of diodes and transistors. The dynamic range is usually limited, and the electronic system is complicated, massive, and power consuming for application in space flights. The novel method designed for this experiment is of wide dynamic range, passive, and miniature. The pulse shape discrimination is accomplished with only one detector input feeding a fast pulse transformer. The pulse transformer has a pair of outputs, each 180° out of phase. One pulse of this output pair is differentiated, then recombined with the other pulse so that they interfere. The resultant is defined as the (dL/dt) pulse. A second pulse is taken simultaneously either from a different transformer output or from another P. M. output. This second pulse is integrated to allow the usual energy unfolding, and is designated the $(\int Ldt)$ pulse.

The entire spectrum of particles is displayed with a two-dimensional plot of the $(\int Ldt)$ vs. (dL/dt) pulses where each curve represents a different particle type. Figure 4 shows a two-dimensional contour display for an Am-Be neutron and gamma spectrum. For a relative comparison of the many pulse shape discriminating systems, we have plotted in Figure 5 a one-dimensional section through the two-dimensional spectra at the Co^{60} Compton edge (50% point). The relative separation of γ and n events is best described by the "M" value, the peak to peak separation divided by the sum of the two full-widths-at-half-maxima (FWHM). The spectrum of Figure 5 has a "M" value of greater than 3.1.

Since it was necessary for the $n\text{-}\gamma$ detector and associated electronics to have an in-flight calibration (I. F. C.) in order to check stability, two different methods were initially developed. It was also considered necessary that the I. F. C. be such as to calibrate the NE 213 scintillator along with the successive systems for both the ($\int Ldt$) and the (dL/dt) pulses. Since the P. S. D. was able to separate α from both n and γ , and since the anticoincidence system would not "leak" an external α ; the I. F. C. was designed around an α emitting isotope, Am^{241} . The first method tried was to use an organic-metal salt of Am^{241} which was completely soluble in the Xylene solvent of NE 213. Although the Am^{241} salt neither quenched the scintillator nor degraded P. S. D., it was found to exhibit only marginal α separation and too small a pulse height relative to the n pulse height. A possible explanation may be the 60 Kev γ , emitted in near coincidence with the α . A more satisfactory method of I. F. C. was found by coupling two different types of scintillators, one organic and one inorganic; the latter of which was doped with a radioactive salt of Am^{241} .³ A very small $\text{NaI}(\text{Tl}, \text{Am}^{241})$ doped scintillator was found to give excellent α P. S. D. from the n and γ , and to be of sufficient pulse height so as to form an I. F. C. with $\sim 4\%$ resolution in both the ($\int Ldt$) and (dL/dt) P. H. A.

On Board Electronic System and Ground Decoder System

Since the expected total counting rate of the detector will be less than 10 counts per second, one may apply noise detecting and correcting logic to the system. This low count

rate will permit adding reliability to the information transmitted. The data to be pulse height analyzed is two parameter: $(\frac{dL}{dt})$, $(\int Ldt)$. The flight electronics, therefore, consists of a pair of logarithmic analog to digital converters. Single error detection is incorporated by the use of a parity bit for the transmission of this pair of words. Furthermore, to offset the possible contamination of the pulse coded data in transmission, a redundant, one bit width delayed transmission is sent at a different subcarrier frequency. This same fixed delay is added to the received telemetry, but in the other subcarrier. This allows a simple electronic comparison check of the transmission, immune of R. F. noise.

Acknowledgments

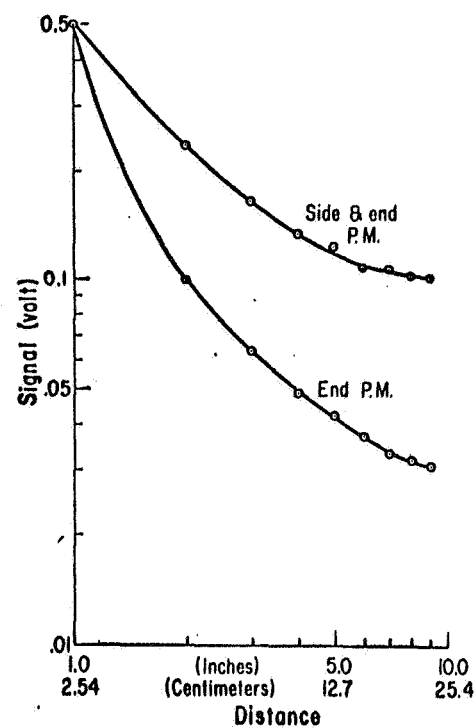
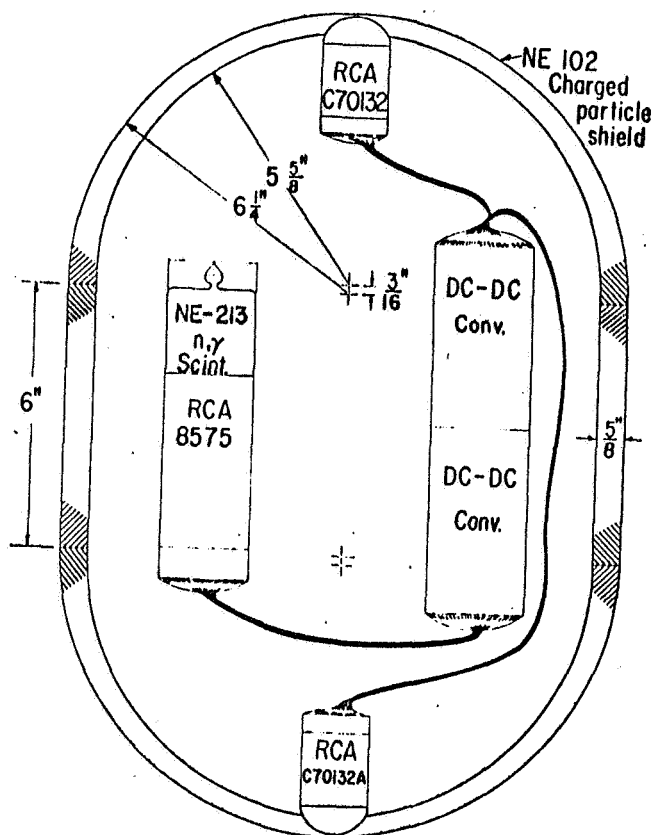
We acknowledge the assistance of Messrs. D. F. Schow, E. L. Nickoloff, and A. A. Sarkady in design and testing of the sensor and electronics system. The cooperation of Mr. Heath of Nuclear Enterprise, Ltd., in the fabrication of neutron scintillators and the 4π shield is appreciated. Discussions of neutron detecting systems with Dr. V. V. Verbinski and Dr. W. R. Burrus were most helpful.

References

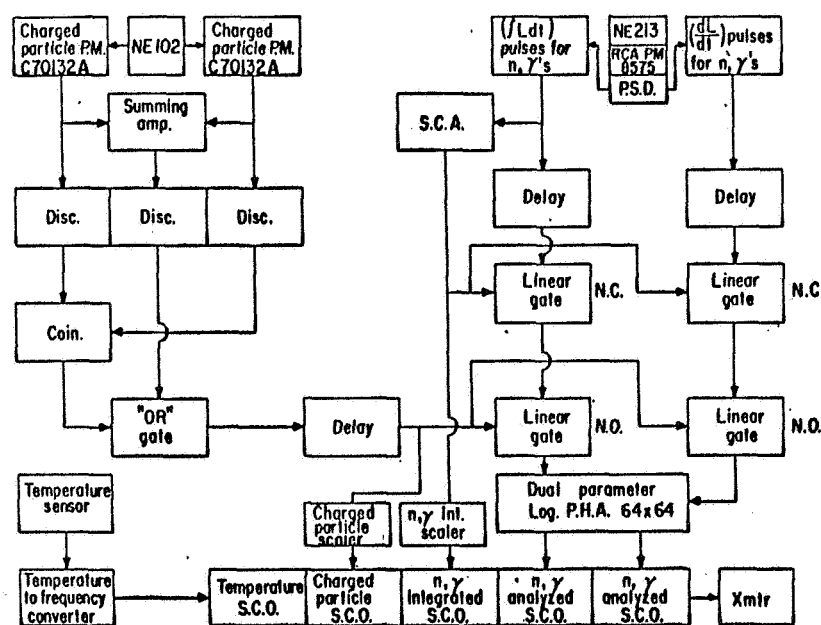
- 1) Fenton, K. B., J. Geophys. Res., 72, 3889-3894, 1967.
- 2) Chupp, E. L., A. A. Sarkady and H. P. Gilman, Planet Space Sci., 15, 881-892, 1967.
- 3) Harshaw Chemical Co., Integral Light Pulser

Figures

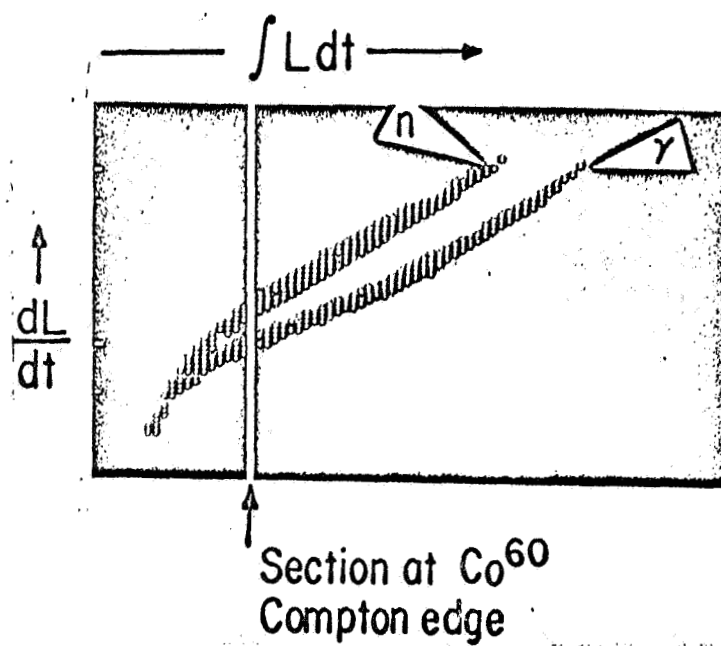
- 1) n- γ detector and charged particle shield.
- 2) Comparison of scintillator attenuation between two photomultiplier types: flat end with side and flat end only.
- 3) Schematic of Electronics System.
- 4) Two parameter (64 x 64) contour display of AmBe neutron-gamma spectra.
- 5) Single parameter section of Figure 4 at the energy equivalent to the Co^{60} Compton edge.



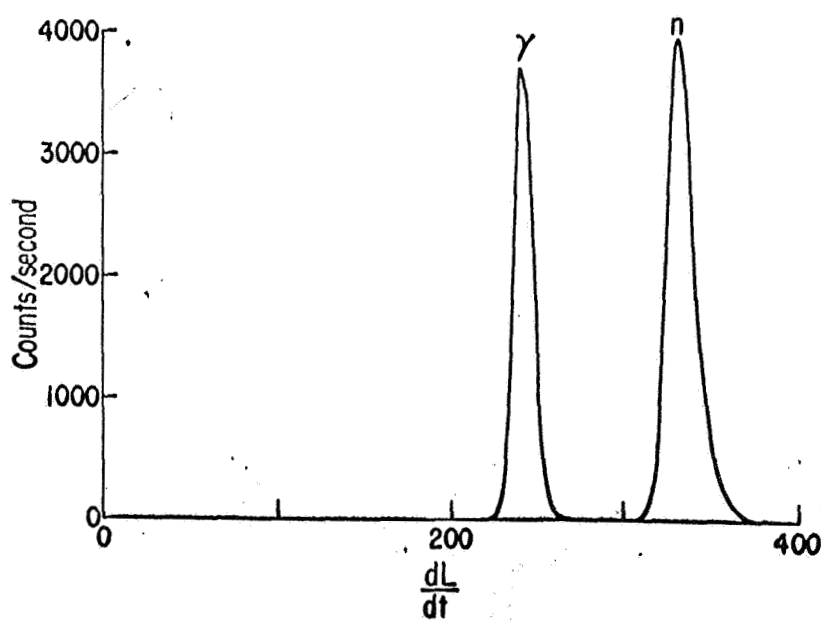
2



3



4



5

A SIMPLE HIGH RESOLUTION PULSE SHAPE DISCRIMINATOR

A Simple High Resolution Pulse Shape Discriminator

R. N. St. Onge and J. A. Lockwood
University of New Hampshire
Physics Department
Durham, New Hampshire

ABSTRACT

A pulse shape discrimination system has been developed with the following characteristics: high multi-particle resolution ($M \approx 3$), wide dynamic range ($1 < E_n < 30$ Mev), simplicity, passiveness, stability, high-count-rate capability (> 50 KHz), built-in calibration, minimum weight (< 20 grams) and low power consumption. This system simultaneously extracts the separate gamma-ray and neutron pulse height spectrums. The sample data presented were obtained with NE213 liquid scintillators, RCA 8575 photomultipliers, and two parameter pulse height analyzers.

A Simple High Resolution Pulse Shape Discriminator

I. Introduction

In experiments to measure the fast neutron energy spectrum at the top of the earth's atmosphere, it is necessary to separate the neutron events from the γ -rays, assuming the usual anticoincidence charged particle shield is included. The pulse shape discriminating system to be described provides good separation of neutrons from gamma rays over an extensive energy range. For γ -rays the energy resolution obtained with the organic liquid scintillator is good enough to determine the energy spectrum of the γ -rays. The data display method permits the simultaneous determination of both the neutron and γ -ray pulse height spectrums. This pulse shape discriminator (PSD) has been used to measure the neutron and γ -ray spectrums in the atmosphere with balloons and will be incorporated in a forthcoming series of rocket flights to evaluate the energy spectrum of the cosmic-ray neutron leakage flux.

The requirements imposed and successfully realized in the design of the PSD were (1) unambiguous simultaneous

identification of both particle energy and particle type; (2) wide dynamic range (neutrons, $1 < E_n < 30$ Mev; γ -rays, $0.5 < E_\gamma < 10$ Mev; (3) simplicity; (4) use of passive circuit elements for high temperature stability and low power consumption; and (5) minimum sensitivity to photo-multiplier (PM) gain changes. Present PSD methods do not meet all these criteria simultaneously. For example, the many methods suggested by M. Forte et al.¹⁾ use fast diodes which have inherently poor temperature characteristics and a limited useful dynamic range. The PSD of F. D. Brooks²⁾, and later of W. Daehnick and R. Sherr³⁾, is very difficult to adjust over a wide dynamic range, is quite sensitive to any PM gain changes and only the neutron channel is directly displayed. The space charge saturation method first employed by R. B. Owen⁴⁾, and later by R. Batchelor et al.⁵⁾ and H. W. Brock and C. E. Anderson⁶⁾, has a very limited dynamic range. The method of T. K. Alexander and F. S. Goulding⁷⁾ is very complex. Zero crossing methods^{1,8)} are also quite involved.

In this paper we will describe the PSD circuit, the method of incorporating an in-flight calibrator into the n- γ detecting system and typical PSD separations of protons from electrons.

II. Description of the PSD Circuit

Since different particles in traversing some scintillators lose energy by exciting the electronic transitions of organic molecules in a unique manner, the nuclear particle type and energy can usually be simultaneously identified. The excited scintillator subsequently radiates this energy in a particular combination of modes uniquely dependent upon the particle type and its energy loss⁹).

Discrimination among the different types of particles in a scintillator is usually made by comparing the amplitudes of the fast component to total output of all the decay modes for each particle type¹⁰). Although it is expected theoretically that the optimum comparison would be between the amplitudes of the fast and the slow components, the system to be described will compare the slow to the total integrated amplitude of all decays. The reason for this method of comparison lies in the saturating, non-linear characteristics of the PM, i.e., very fast, high intensity decays cannot be faithfully followed because of space charge saturation. Thus, the use of these distorted fast decays would cause a greater dispersion in the particle separation. Also, the use of the total integrated signal serves a dual purpose. First, the necessary pulse height spectrum can be simultaneously extracted from it. Second,

since the total integrated signal must always be greater than either its fast or slow component at the same PM output, the total integrated signal may be picked off at an earlier dynode to avoid any subsequent space charge saturation. Hence, practical considerations dictate the comparison of the slow to the total pulse amplitudes.

The basic idea of the PSD is the partially destructive and constructive interference of a pair of electronic pulses derived from one PM detector pulse. This one original pulse may be taken either from a dynode or the anode of the PM. The particular method of obtaining this pair of pulses from one pulse uses a 50 Ω miniature fast pulse transformer¹¹⁾ connected to the 50 Ω anode output of an RCA 8575 PM as shown in Figure 1. Such a device will produce two identical, conjugate, 180 $^\circ$ out-of-phase, unipolar pulses from one input pulse, i.e., opposite polarity, but exactly in time phase. These two opposite polarity pulses are then operated upon separately and subsequently recombined to interfere. The summing operation can be carried out in either of two methods: a simple resistor summing network or another two input, non-inverting fast pulse transformer.

Either the first or the second operation (as shown in Figure 1) can be chosen to suit the particular scintillator or PM characteristics. Such operations might be: RG differentiation,

RC integration, delay, clipping, stretching and identity (no operation).

The particular pair of operations chosen for the fast organic liquids such as Nuclear Enterprises 213 or 222 were RC differentiation and identity, indicated schematically in Figure 2. One pulse is RC differentiated with a short time constant, thus producing a bi-polar pulse. The other pulse, of opposite polarity, is added to interfere appropriately and thereby cancel the first part of the RC differentiated bi-polar pulse. Such a cancellation produces an extremely shape sensitive output without the use of any non-linear devices. The unipolar output is finally integrated before it enters a preamplifier. Since this pulse is related to a differentiation, it is conveniently defined as the (dL/dt) pulse and is particularly dependent on particle type.

Simultaneously a pulse is taken from another dynode, integrated for several decay times, and then amplified. So this pulse is defined as the $\int L dt$ pulse and is related to particle energy.

The two pulses (dL/dt) and $\int L dt$ are plotted against each other on a two-parameter field to realize the particle separation. This display method is similar to that used by $\frac{dE}{dx}$ x E detector systems.

The entire PSD circuit designed for space use weighs less than 20 grams and is less than 5 cm in diameter when mounted on a single printed circuit board. It has been used with the RCA 8575 PM operated at negative high voltage. A preliminary layout is shown in Figure 3. There is no limitation to the size reduction possible, but since stray capacitance is important, optimization would be necessary with each redesign.

III. Results

Figure 4 is a two-dimensional low-level contour display of (dL/dt) vs $\int L dt$ for the neutron and γ -ray spectrums from an Am-Be source. The Co^{60} Compton-edge pulse height corresponds to an electron energy of 1.1 Mev or of recoil protons of about 3 Mev. For a relative comparison with the many PSD systems, we have plotted in Figure 5 a one-dimensional section through a two-dimensional spectrum at the Co^{60} Compton edge (50% point). The relative separation of γ and n events is best described by the M value, defined by¹²⁾

$$M = \frac{\Delta}{\delta_1 + \delta_2}, \text{ where } \Delta = \text{peak-to-peak separation}$$

and δ_1 and δ_2 are the full widths at half maximum for the two peaks. For the data shown, $M = 3.1$.

We find that M values of 2 can be obtained down to proton energies of about 1 Mev. On the other hand, the upper limit can be extended to greater than 15 Mev with no apparent decrease in M . Moreover, the actual dynamic range is limited, not by the PSD itself, but by the characteristics of the amplifiers and pulse height analysers following the PSD.

The test results from exposing the actual balloon flight unit to the 14 Mev monoenergetic output from the (d,t) reaction and to a Co^{60} γ -ray source simultaneously are shown in Figure 6. The neutron energy range is 1 to 15 Mev and with a gain change can be increased to 30 Mev. Contours of full width at half maximum (FWHM) are plotted. The co-ordinate system is non-linear to make optimum use of the pulse height analyzer range, assuming that the neutron differential energy spectrum at the top of the atmosphere can be crudely represented by K/E .

Two methods of in-flight calibration (IFC), both of which used alpha particle sources, were tried. These were designed about the concept of a 4π -enclosing, anti-coincidence, charged particle shield¹³). This allows the inner, enclosed NE213 detector to "observe" only neutral

radiation. Since external alpha particles would normally be excluded, the α -particle region of the two-parameter display can be conveniently used to display the output from an internal α -particle IFC.

The first method involved a radioactive alpha-emitting salt of Am^{241} completely soluble in NE213 and yet not detrimental to the PSD property of the scintillator¹⁴). Although this approach was successful, it was not useful in this application because the light output obtained by alpha particle excitation of the organic scintillator was too small relative to neutron excitation in the energy range of interest.

The second IFC method used a small chip of NaI(Tl) light pulser¹⁵ doped with Am^{241} (≈ 4 mm diameter x 4 mm long). The pulse shape separation with such a technique is exceptional because the much slower decay time of NaI(Tl) is easily discriminated from the fast organic (NE213) decays, i.e., the PSD system is operating as a phoswich¹⁶).

The pulse heights from the scintillator for the IFC can be adjusted by changing the size of the exit aperture on the crystal face of the miniature light pulser. The allocation of PHA area to the pertinent energy region of interest can be optimized, yet an α -IFC peak can be retained in the adjacent region. The output from such an IFC is shown in the upper right-hand portion of the dL/dt vs $\int L dt$ plot in Figure 6.

Improved energy resolution in the IFC can be obtained by using a stronger source. In this flight unit the telemetry system limited the counting rate of the IFC source to $\sim 4 \text{ sec}^{-1}$.

IV. Discussion

Although this method has the obvious disadvantage of requiring a two-parameter PHA, one can obtain excellent n- γ separation ($M \approx 3$) over a wide dynamic range ($1 < E_n < 30 \text{ Mev}$) at relatively high count rates ($> 5 \times 10^4 \text{ sec}^{-1}$). No effort was made to go to neutron energies lower than one Mev, nor has the upper limit been explored. No adjustment of the PSD is needed for changes in any of the following: individual characteristics of 8575 PM tubes, high voltage value, type of PSD liquid scintillators, or particle energy.

In conclusion, this PSD system has the advantage of simplicity, passiveness and miniaturization. It operates over a wide dynamic range with high resolution and makes possible multiple particle pulse shape discrimination.

This research was supported under National Aeronautics and Space Administration contract NASr-164.

We are grateful to Dr. Victor Scherrer, National Aeronautics and Space Administration, Electronics Center, Boston, Massachusetts, and Dr. E. Chupp, University of New Hampshire, for the use of specialized electronics equipment. The computer programming for the data display was developed by Mr. Archer Buck and Mrs. S. Dewdney. Mr. Edward Nickoloff assisted with several data runs.

References

1. M. Forte, A. Konsta, and C. Maranzana, Proc. Nucl. Energy Conf. (Belgrade) 2 (1961) 277.
2. F. D. Brooks, Nuc. Instr. and Meth. 4 (1959) 151.
3. W. Daehnick and R. Sherr, Rev. Sci. Instru. 32 (1961) 666.
4. R. B. Owen, IRE, Trans. Nuc. Sci. 3 (1958) 198.
5. R. Batchelor, W. B. Gilboy, A. D. Purnell and J. H. Towle, Nuc. Instr. and Meth. 8 (1960) 146.
6. H. W. Brock and C. E. Anderson, Rev. Sci. Instr. 31 (1960) 1063.
7. T. K. Alexander and F. S. Goulding, Nuc. Instr. and Meth. 13 (1961) 244.
8. M. L. Roush, M. A. Wilson and W. F. Hornyak, Nuc. Instr. and Meth. 31 (1964) 112.
9. G. T. Wright, Proc. Phys. Soc. (B) 69 (1956) 358.
10. F. D. Brooks, Prog. Nuc. Phys. 5 (1956) 252.
11. Vari-L Co. Inc., (Model #50200E), Stamford, Conn.
12. W. B. Reid and R. H. Hummel, Can. Nuc. Tech. Jan.-Feb. (1966).
13. R. St. Onge and J. A. Lockwood, IEEE Trans. Nuc. Sci. 15 (1967) 264.
14. New England Nuclear Corp., Boston, Mass.
15. Harshaw Chemical Corp., Cleveland, Ohio, Integral Light Pulser
16. D. H. Wilkinson, Rev. Sci. Instr. 23 (1952) 414.

Figure Captions

- Figure 1. Schematic diagram of the PSD operations.
2. PSD circuit diagram
 3. PSD mounted on microstrip
 4. Two parameter (64 x 64) low-level contour display of the Am-Be n- γ spectrums.
 5. Single parameter cross-section for Figure 4 at the energy equivalent to the Co⁶⁰ Compton edge.
 6. Two parameter (64 x 64) contour display of 14 Mev neutrons and Co⁶⁰ γ -ray spectrums for flight unit.

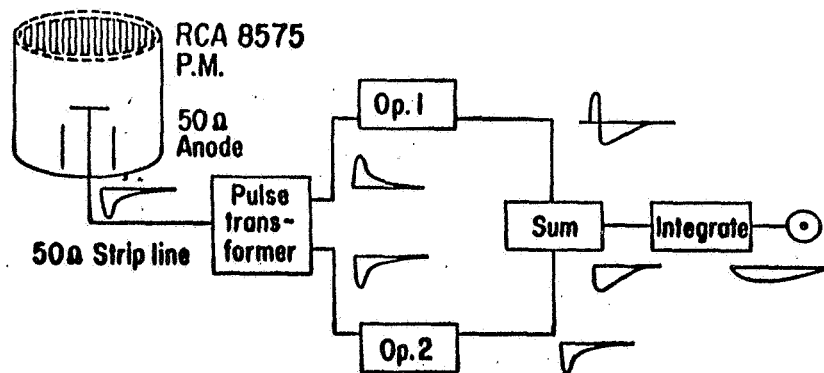


Figure 1

Fast Neutron-Gamma ray detection system

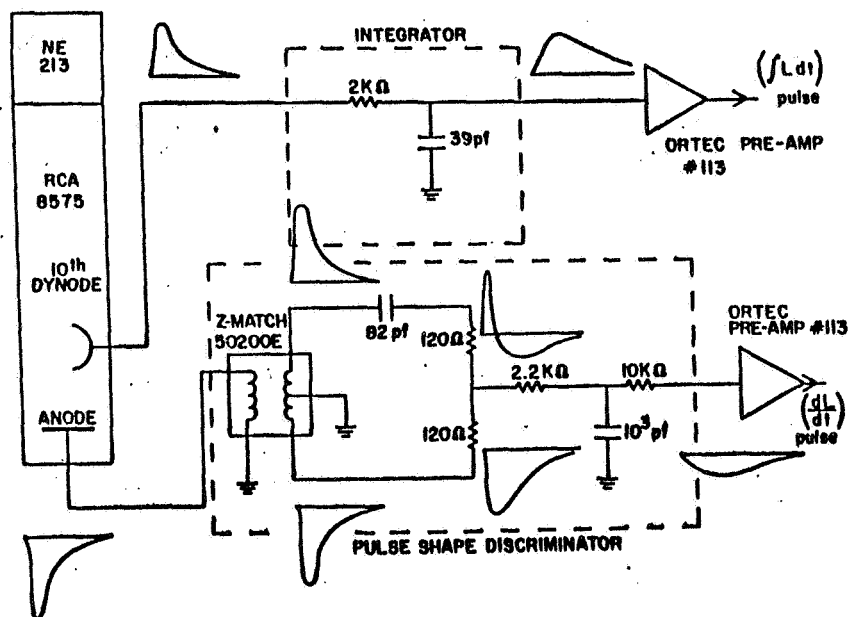


Figure 2

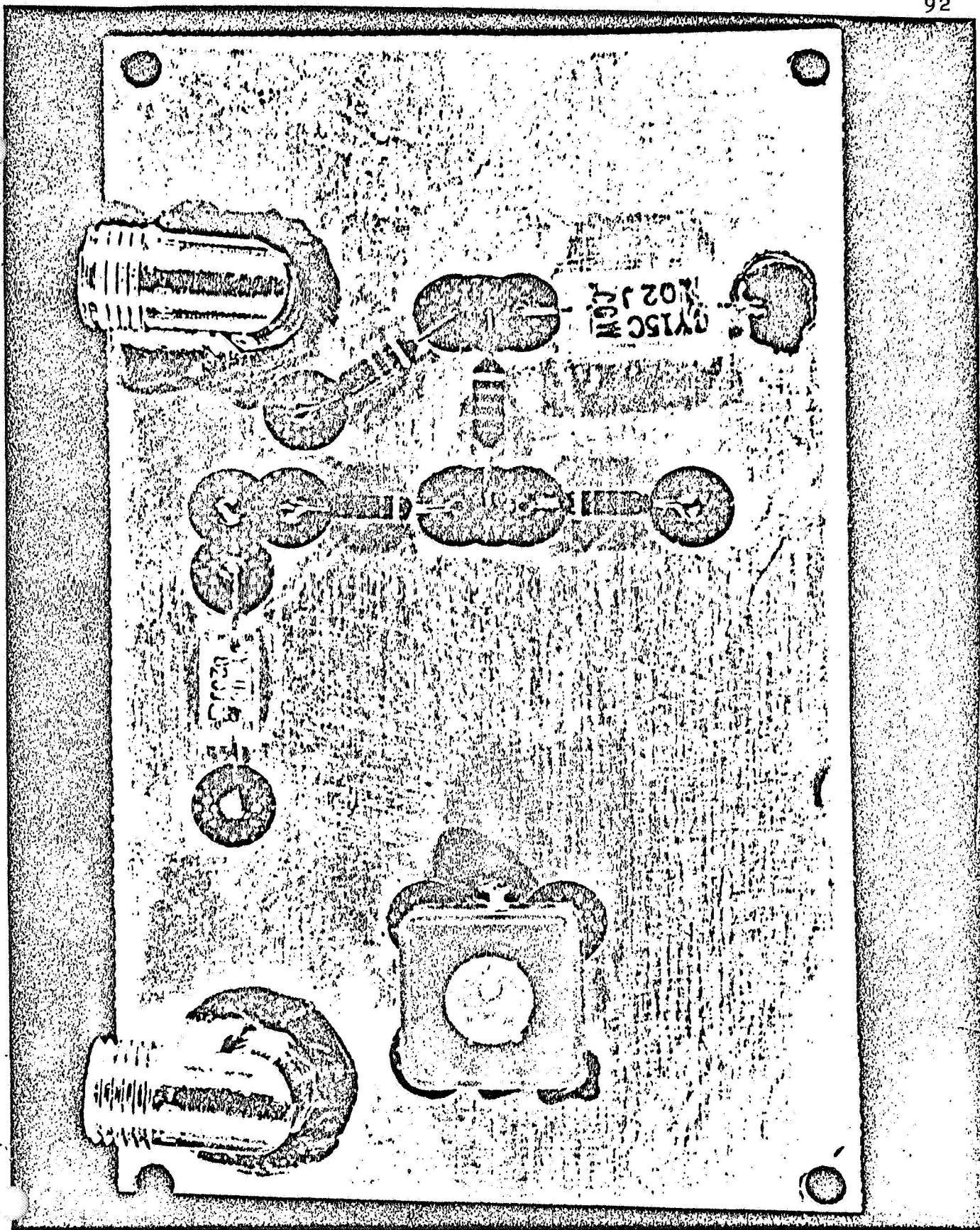


Figure 3 enlargement

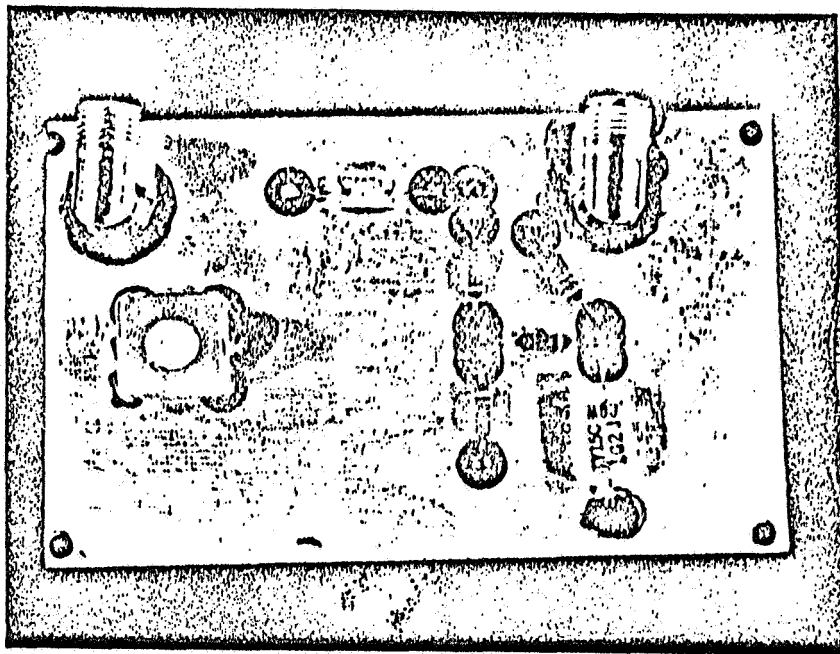


Figure 3

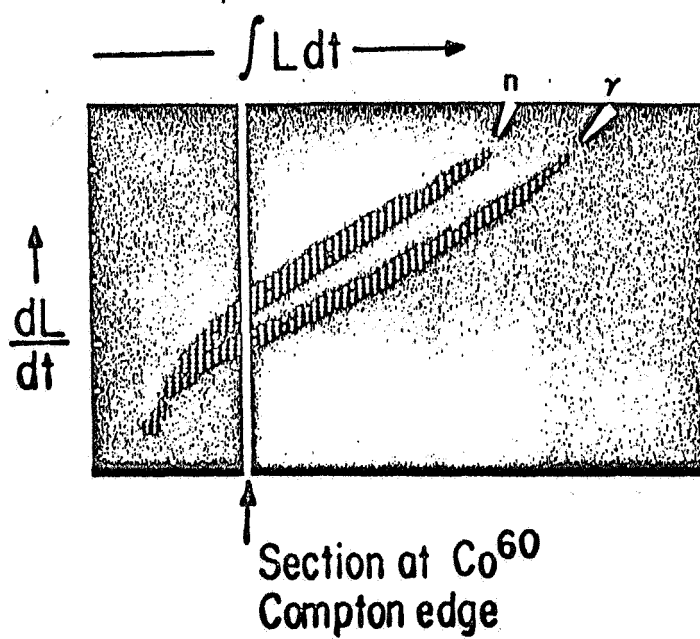


Figure 4

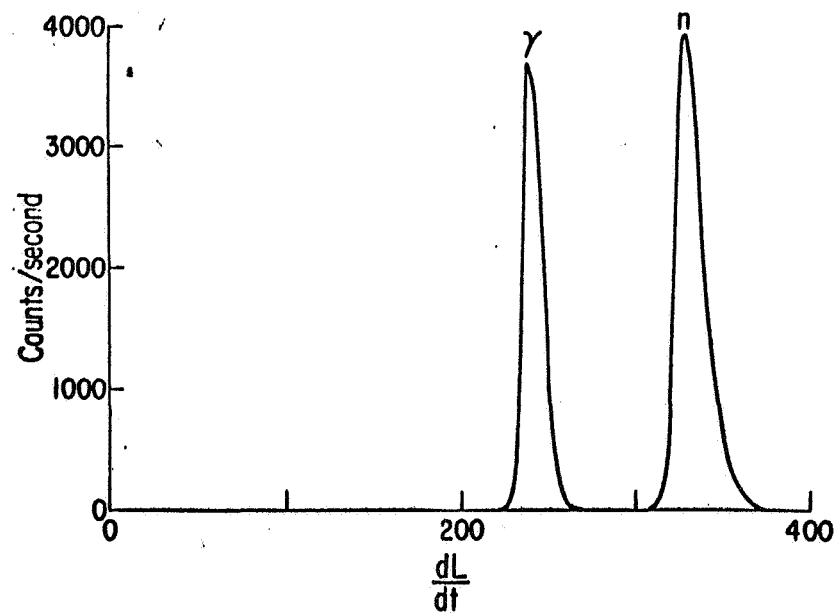


Figure 5

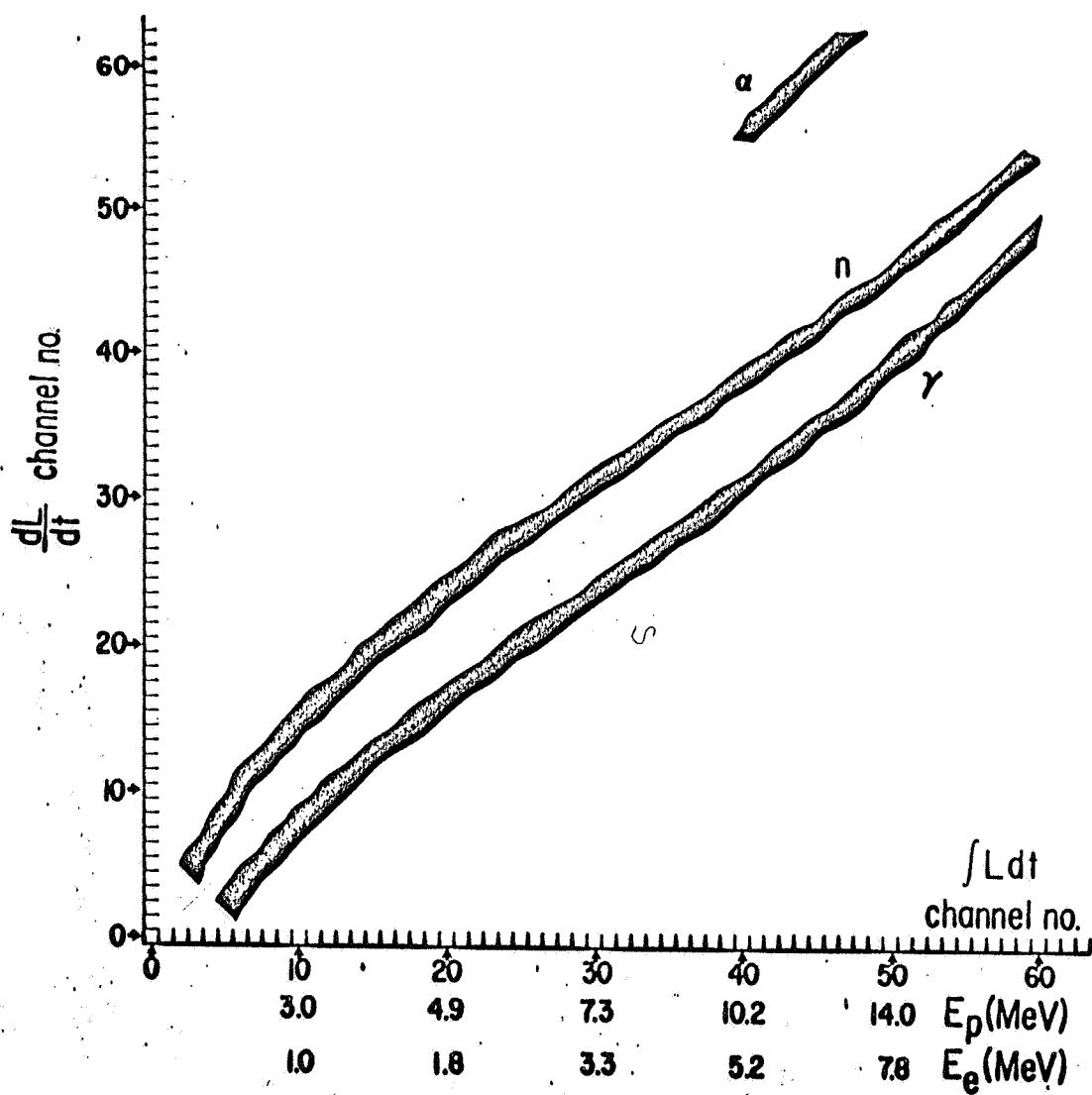


Figure 6

A TOTAL ENCLOSING ACTIVE CHARGED PARTICLE SHIELD

A Total Enclosing Active Charged Particle Shield

R. N. St. Onge and J. A. Lockwood
University of New Hampshire
Physics Department
Durham, New Hampshire

In order to measure accurately the neutron and gamma-ray fluxes at the top of the atmosphere, it is necessary to surround the neutron and gamma-ray detector with an anti-coincidence charged-particle shield. Since the ratio of the neutron or γ -ray flux to the charged-particle flux is small, the shield must be very effective ($> 99.9\%$) in rejecting minimum ionizing charged particles. For a series of balloon flights we have designed a 4 π active charged-particle shield, which operates in anticoincidence with the enclosed neutron detector. Neutrons are separated from γ -rays in the inner detector by a simple pulse-shape discriminating (PSD) circuit^{1,2}). The entire shield has a minimum total mass for the given internal volume and uses only two photomultipliers, both located within the volume of the active shield. The adiabatic light piping concepts used in the shield to minimize the light attenuation from unnecessary corners insures excellent charged-particle rejection. Only simple logic circuits are required in the associated electronic system for count rates $\sim 10^3 \text{ sec}^{-1}$.

The general shape and size of the dome are indicated in Figure 1. Two hollow plastic scintillators (NE102), which are hemispherical sections, are optically mated with a hollow cylindrical section of the same material. A photomultiplier (RCA C70132A) with a curved photocathode is optically potted into the inside of the top section, with the same arrangement in the lower half-section. The effects of both total internal reflection (TIR) and spectral reflection (SR) are successfully combined in the shield design. TIR is first used to gather the scintillation light falling within the acceptance angles defined by Snell's law. Secondly, SR from the crinkled aluminum foil, loosely wrapped around the entire dome, re-channels to the photomultiplier that light failing to meet the initial TIR critical angle. Diffuse white paint is applied directly to the outside of the dome areas near each PM to diffusely scatter more light into the PM cathodes.

The outputs from the two photomultipliers are fed separately into parallel sum and coincidence logic (Figure 2). This insures operation under the worst situations where particles do not traverse entirely through the dome, i.e., enter but do not exit. Two such extreme situations will be described. First, if a charged particle passes through the dome wall near either PM, there will be a very large signal generated at that PM. However, there may be no detectable

signal at the distant PM. Thus, the coincidence circuit would probably not be triggered. On the other hand, the summing circuit, which is followed by a voltage threshold discriminator will recognize the very large signal (near PM) added to the very small signal (distant PM). This large signal in the summing circuit triggers the associated lower level discriminator. Such an event would not be reliably detected in the normal coincidence logic. The second extreme situation will occur when a particle enters the cylindrical section about equi-distant from the two photomultipliers and generates small, approximately equal, signals in the two photomultipliers. Hence, the lower level discriminators before the coincidence circuit, which have been set at a lower level than for the summing circuit, are simultaneously triggered to generate a coincidence gate. In this latter situation, the summing network may also superflously generate a signal from its associated lower level discriminator. However, in this case, definitive gating is provided by the coincidence circuit.

Other events produced by particles not traversing the dome will be a combination of the above two extreme cases. For most cases where the charged particle penetrates completely through the dome the gating is provided by the coincidence logic. Then, the summing circuit provides redundancy.

This design is based essentially upon the shield thickness being compensatingly greater at larger distances from the phototubes. Consequently, the particle produces an appropriately larger signal farther from the phototubes. Further, the light is adiabatically guided to concentrate upon the small region of the PM cathode. To provide this light generating compensation, and yet facilitate manufacturing, the centers of curvature were offset for the inner and outer spherical surfaces. For an initial design criterion we can write:

$$\begin{aligned}\text{Sum voltage pulses} &= V(\text{PM}_1) + V(\text{PM}_2) \\ &= f_1(X) g_1(X) + f_2(X) g_2(X) = H,\end{aligned}$$

where X = distance (cm) along the light path from the particle entry point to the particular PM.

$f_1(X)$ = thickness function for particle entry at X_1 ,

$g_1(X)$ = attenuation function for light to travel from X_1 to PM_1 ,

H = a constant independent of X .

And the attenuation was taken to be:

$$\begin{aligned}g(X) &= K \exp(-X/20), \text{ so that the thickness} \\ \text{function } f(X) &= g(X)^{-1} = K^{-1} \exp(X/20).\end{aligned}$$

This function for a single PM is plotted in Figure 3 over the necessary range of X . Then as a first approximation for the thicknesses in the dome of a 25 cm diameter, the necessary ratio of the maximum to the minimum thickness was taken as $\sim 3/2$. This is one-half the ratio shown in Figure 3 because two PM's are summed in the flight unit. Since the size of the PM cathode required a minimum dome thickness of about 1.11 cm for adequate strength near the PM, the maximum wall thickness at the center section must be about 1.59 cm, which is accomplished by a center offset of 0.48 cm (Figure 1).

After construction of the shield, the experimental response of a single PM to the position of a Am^{241} Integral Light Pulser³) was measured to be approximately:

$$f(X) \approx 1.18 \exp(-X/2) + 0.15 \exp(-X/50)$$

as shown in Figure 3. The added first term in $f(X)$ is related to the initial rapid change with X of the solid angle subtended by the source at the PM, neglected in the original design. The second term $\exp(-X/50)$ is the normal exponential light attenuation of the curved material.

Based upon this measurement, we can improve the original design. However, since the exact inverse of $f(X)$ is not a simple function, it is difficult to machine the shield to conform to $f(X)^{-1}$. But as a best approximation, the ratio of maximum to minimum thickness could be made equal to the fractional loss by transmission for the near to the far light paths.

From Figure 3 this is 5.2, which is twice that for two PM's. Thus, the second generation of charged-particle shields to be built should have a maximum thickness of 2.54 cm with a minimum of 1.11 cm which can be obtained by a center offset of 1.11 cm.

Some n- γ detecting systems have used one photomultiplier to view both the n- γ detector and the charged-particle shield. Such a shield only encloses the n- γ scintillator against secondary production and not the associated PM or electronics. A pulse-shape discrimination (PSD) circuit separated neutrons from γ -rays in the inner detector and a phoswiching technique^{4,5}) gates off the n- γ detector whenever a charged particle passed through the thin phoswich shield. With such a scheme, it is very difficult to provide the necessary high resolution, unambiguous scintillation light to the PSD system which is required to separate the neutron and gamma-ray spectra⁵). Scintillations in the phoswich (charged-particle shield) and in the internal scintillator from neutrons and γ -rays become optically mixed. It is then difficult to decompose the light combinations to distinguish the neutrons from the γ -rays, as well as from the charged particles.

Conversely, if simple flat-sheet scintillators are shaped in a box, many PM's are required to provide excellent charged-particle rejection. If the PM's are placed inside, the

box must be larger than with the dome design. Such a large shield will have high-count rates and consequently large dead times. Alternatively, the PM's could be placed outside, but this would increase the cosmic-ray produced secondaries and distort the ambient neutral particle spectra.

We believe that this represents a considerable advance in the design and operation of charged-particle shields for neutron and gamma-ray experiments. A recent balloon flight of several hours duration has shown that the original design is adequate. It is important to note that this minimum mass shield would not work reliably without both the concept of non-uniform thickness and the parallel sum-coincidence electronic logic.

We acknowledge the assistance of Messrs. Edward Nickoloff and David Klumpar, in various stages of this investigation. Also, we are grateful to Mr. David Forrest for valuable discussions concerning shielding methods. The dome was manufactured by Nuclear Enterprises, Inc., under the cooperation and guidance of Mr. John Heath. This research was supported by the National Aeronautics and Space Administration contract NASr-164.

References

1. R. St. Onge and J. A. Lockwood, IEEE Trans. Nuc. Sci. 15 (1967) 264.
2. R. St. Onge and J. A. Lockwood (accepted for publication in Nuc. Instr. and Methods) 1968.
3. Harshaw Chemical Corp., Cleveland, Ohio, Integral Light Pulser.
4. D. H. Wilkinson, Rev. Sci. Instr. 23 (1952) 414.
5. R. B. Mendell and S. A. Korff, Rev. of Sci. Instr. 34 (1963) 1356.

Figure Captions

- Figure 1 Charged particle shield.
- 2 Schematic of charged-particle electronics system.
- 3 Transmission characteristics of the charged-particle shields.

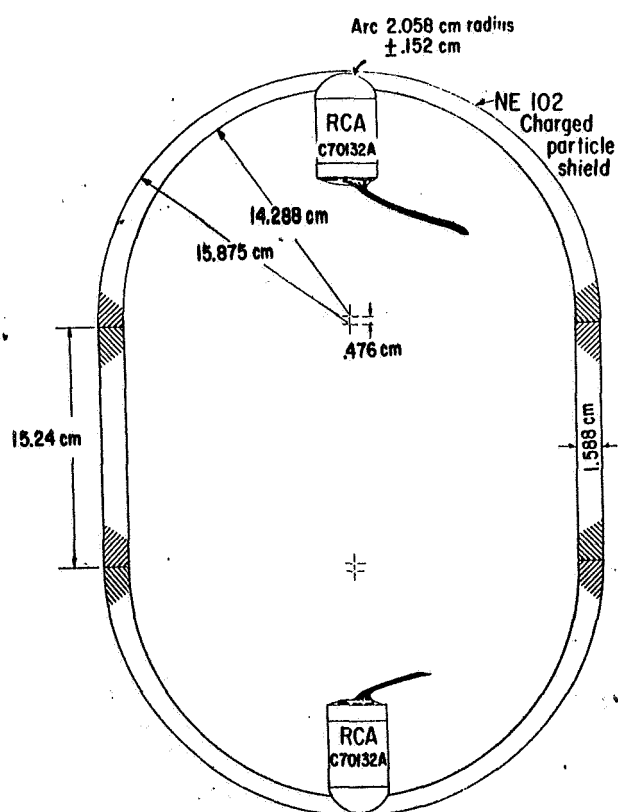
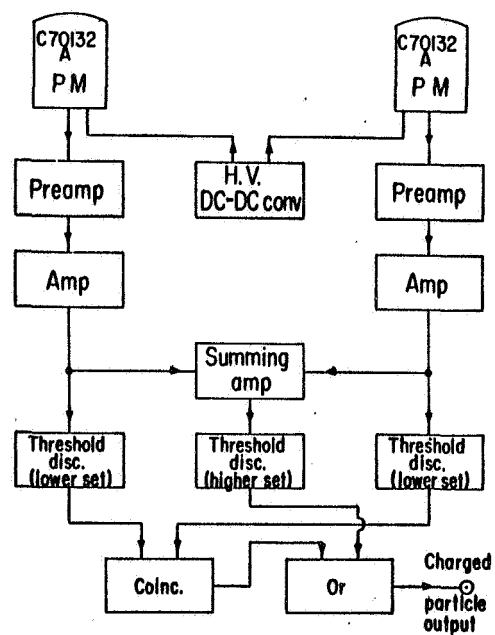


Figure 1



Charged particle shield system

Figure 2

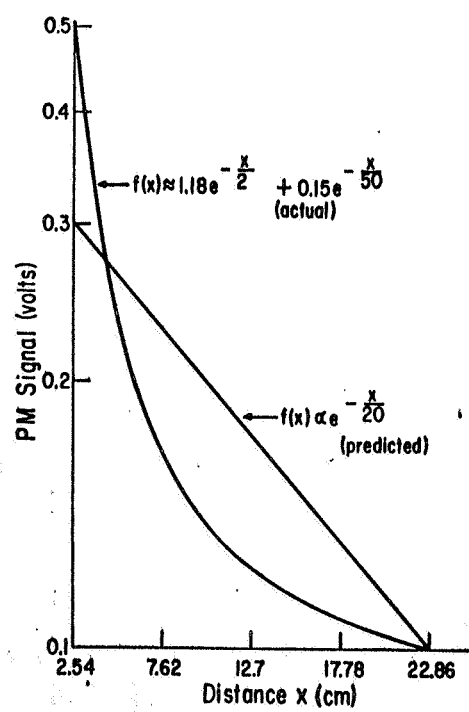


Figure 3

THE ENERGY SPECTRUM AND FLUX OF FAST NEUTRON
IN THE ATMOSPHERE

The Energy Spectrum and Flux of Fast Neutrons
in the Atmosphere

R. N. St. Onge* and J. A. Lockwood
Physics Department, University of New Hampshire
Durham, New Hampshire 03824

ABSTRACT

The energy spectrum of fast neutrons (3-20 MeV) in the atmosphere at the Pfofzer maximum ($\sim 100 \text{ g/cm}^2$) was measured at geomagnetic latitude 42°N ($P_c = 4.4 \text{ GV}$). The n- γ detector was a 5 x 5 cm diameter cell of organic liquid scintillator (NE213) coupled to a high-resolution, two-parameter, multiparticle pulse-shape discriminator (PSD) with a two-parameter (64 x 64) logarithmic pulse-height analyzer. An anticoincidence charged-particle shield completely enclosed the n- γ detector. The spectral parameter $\beta(E)$ of the differential neutron energy spectrum decreased smoothly from 4.0 ± 1.0 at 3 MeV to 1.2 ± 0.7 at 20 MeV. The integrated neutron flux at Pfofzer maximum between 3.5 and 10.0 MeV was $0.36 \pm 0.10 \text{ neutrons/cm}^2 \text{ sec}$. The implications of these results for the high-energy albedo neutron leakage as a source of the energetic proton flux in the radiation belts are discussed.

* Present address: Physics Department, Michigan State University, East Lansing, Michigan

I. INTRODUCTION

Neutrons in the earth's atmosphere are produced by the interaction of both galactic and solar cosmic rays with air nuclei. An investigation of the energy spectrum and flux of the neutrons from both of these sources is important for several reasons: (1) an energetic neutron diffusing out of the atmosphere can decay into a proton and electron within the magnetosphere and then these may be trapped by the geomagnetic field to contribute to the radiation belts¹; (2) the capture of neutrons by atmospheric nitrogen is responsible for the production of the age-dating nucleus C^{14} through the reaction $N^{14}(n,p)C^{14}$; and (3) the neutrons are genetically related to the lower portion of the energy spectrum of the galactic cosmic rays. A comprehensive review of atmospheric neutrons has been given by Schopper et al.².

Any evaluation of the contribution made by the neutron leakage (1) to the population of energetic protons in the inner radiation belt depends upon a knowledge of the neutron energy spectrum and flux at the top of, or above, the atmosphere. Calculations have been made of the intensity and energy spectrum of the neutron leakage³⁻⁵. Dragt et al.⁶ and Hess and Killeen⁷ have used these

calculations to determine quantitatively the contributions to the radiation belts. These calculated results agree that this source mechanism is inadequate for trapped protons with $E < 20$ MeV and for protons with $E > 20$ MeV is probably an order of magnitude too small.

Direct experimental evidence on the neutron energy spectrum near the top of the atmosphere is essentially limited to measurements of Haymes⁸, Holt et al.⁹, Baird and Wilson¹⁰, Mendell and Korff¹¹, Zych and Frye¹². The results of Zych and Frye in the energy range $12 < E_n < 100$ MeV were obtained with a spark chamber. The other measurements were all made with recoil-proton detectors using a combination of phoswiching and pulse-shape discrimination (PSD) to separate neutrons from gamma-rays and charged particles.

The present experiment was designed to measure the neutron energy spectrum and flux in the energy interval 3-20 MeV. The neutron detector utilized a separate charged-particle rejection scheme and a two-parameter display system for the PSD which separates gamma rays from neutrons. In this article the neutron energy spectrum and flux measured during a balloon flight on 7 September 1968 from Palestine, Texas, are presented with some discussion of the novel experimental techniques used.

II. EXPERIMENTAL SYSTEM

A major difficulty encountered in determining the secondary neutron decay population in the atmosphere is to reliably detect a small flux of fast neutrons in a much larger background flux of gamma rays and charged particles. To accomplish this, the counter logic first separated the particles into two groups: charged and neutral. Second, the neutral particles were separated into their predominant components: gamma rays and neutrons. Experimentally the charged particles were separated from the neutral particles by placing the neutron and gamma-ray detector inside a thin, hollow, 4π -enclosure of plastic scintillator. The neutral particle detector, contained within this closed shell, was gated off whenever a charged particle passed through the shield. The n - γ detector separated the gamma rays and neutrons by means of their different light-pulse shapes in an organic liquid scintillating cell.

A. The Charged Particle Identifying System

The hollow, 4π , charged-particle anticoincidence shield of plastic scintillator (NE102) is shown in Figure 1. It was monitored by two photomultipliers with hemispherical

photocathodes (RCA C70132A). The wall thickness of the shield was greater at larger distances from the phototubes to allow particles which enter the shield farther from the photomultipliers to generate a larger scintillation. This compensates for the greater light attenuation in the scintillator for these events.¹³ For the most effective use of such a 4π shield the parallel sum and coincidence logic scheme shown in Figure 2 was included. This unusual precaution allowed detection in the important situation where a high-energy charged particle enters the shield, interacts within it, but does not subsequently leave the shield. In order to ascertain quantitatively the rejection efficiency of the shield for charged particles, a preflight test with cosmic-ray secondary muons was conducted. The measured effectiveness was greater than 99.9%. The limitation on the measured effectiveness was due to spurious events occurring during the long time intervals required when using the secondary cosmic-ray muon beam.

B. The Neutral Particle Component n- γ Identifying System

The n- γ separation was made by the pulse-shape discrimination of an organic liquid scintillator (NE213) viewed by a fast photomultiplier (RCA 8575). The PSD

system¹⁴ compared the integrated scintillation light yield ($\int L dt$) with the slow-decay component of the scintillation (dL/dt) in the cylindrical liquid scintillator of 4.6 x 4.65 cm diameter. The photomultiplier (PM) pulses were fed to a high-resolution, multiparticle PSD and were subsequently analyzed and digitized by a logarithmic, two-parameter (64 x 64) pulse-height analyzer (PHA). The effectiveness of the PSD for separating gamma rays and neutrons can be seen quantitatively in Figures 3 and 4. In Figure 3 the two-parameter PSD data from an AmBe neutron gamma-ray source are plotted for a laboratory prototype. The scale in Figure 3 for both dL and L channels is different from that used in the actual flight. Figure 4 is obtained by taking a section of Figure 3 at the $\int L dt$ value for the Co⁶⁰ Compton edge from 1.17 MeV gamma rays. It should be stressed that the effectiveness of the PSD circuit to separate neutrons from gamma rays over a wide energy range is one of the most important factors in determining the neutron energy spectrum in the atmosphere.

An inflight calibrator (IFC) was incorporated into the neutron detector by optically coupling to the NE213 scintillator a small (~3 x 3 mm diameter) crystal of NaI(Tl) doped with a radioactive salt of the alpha emitter Am²⁴¹. The much slower NaI(Tl) scintillations resulting from these doped alpha particles were readily pulse-shaped

discriminated from the neutron and gamma-ray events as shown in Figure 3.

III. MEASUREMENTS

The raw data from the balloon flight, recorded from 4.7 Km (541 mbar) to 19.2 Km (62 mbar), are shown in Figure 5 as a two-parameter ($\int L dt \times dL/dt$) pulse-height spectrum. It can be seen that the PSD system separated four different scintillation pulse shapes. These correspond to Compton electrons, recoil protons, alpha particles from (n, α) reactions and from the IFC. The first three groups of secondary particles result from neutral particles, either neutrons or gamma rays, interacting in the organic scintillator with hydrogen or carbon nuclei. The Compton electrons arise from gamma-ray interactions with atomic electrons, and the recoil protons are produced by $H(n,p)n'$ and $C^{12}(n,p)B^{12}$ reactions. The alpha particles are produced by $C^{12}(n,\alpha)Be^9$ and $C^{12}(n,3\alpha)n'$ reactions. Each of these secondary charged particles was considered in deriving the neutron energy spectrum. The group marked IFC in Figure 5 corresponds to Am^{241} α -particle interactions in NaI.

The individual groups of particles (e,p, α ,IFC) separated in Figure 5 were extracted to obtain pulse-height spectra. However, since the data shown are the average

over a large range of altitudes (541-62 mbar), the pulse-height spectra were examined for changes in spectral shape with altitude. None were found. An analysis of the IFC data indicated that the gain of the two-parameter system and the counting rate were stable to less than 3%. Therefore, the data were scaled by an appropriate constant (1.42) to the count rate that was measured at the intermediate altitude of the Pfozter maximum ($\sim 100 \text{ gm/cm}^2$) to establish a base for comparison. The relative count rates obtained for the Compton electrons, recoil protons and the neutron-produced secondary alpha particles were 142/10/1. The importance of these relative count rates and spectral shapes will be discussed later.

The pulse-height spectra of alphas, protons, and Compton electrons are shown in Figures 6(a), (b), and (c). Then, the pulse-height spectrum for protons (Figure 6(a)) was converted to the recoil-proton energy spectrum shown in Figure 7. This conversion involves correcting for the non-linearity of the flight pulse-height analyzer, for the dependence of scintillation light yield upon energy¹⁵, and for second scattering and wall effects¹⁶. For example, the channel width of the logarithmic PHA was 0.05 MeV at channel number 10 (3.6 MeV) and 0.50 MeV at channel number 60 (15.0 MeV). Consequently, the number of proton recoils per MeV was much larger in the lower flight channels.

Then the method of Broek and Anderson¹⁶ was used to obtain the Pfozter maximum neutron energy spectrum shown in Figure 8. In this method the derivative $d/dE(dN_p/dE)$ as a function of E_p was evaluated from Figure 7. Then the neutron energy spectrum (dN/dE) as a function of energy (E) was calculated from

$$dN_n/dE = - \frac{E}{n_H \sigma_H L} \quad d/dE(dN_p/dE) \quad F(E)^{-1} \quad f(a,L)^{-1}$$

where $a(E) = (n_C \sigma_C + n_H \sigma_H)$ is the total effective cross-section in the scintillator, L = the length of the scintillator, $F(E)$ = correction factor for second scattering and wall effects, and $f(a,L)$ = correction factor for the neutron flux attenuation in the scintillator. Typically $F(E) = 1.10$ at $E = 1.0$ MeV and $F(E) = 0.95$ at $E = 20$ MeV¹⁶. The correction factor $f(a,L)$ was closer to unity.¹⁷

Since approximately one half the nuclei in the scintillator were carbon, an analysis of the effects of the carbon nuclei was necessary. There are two types of reactions with carbon that are important, $^{12}\text{C}(n,p)$ and $^{12}\text{C}(n,\alpha)$. The first reaction will produce a proton which complicates the unfolding procedure because the Broek-Anderson method was based upon protons from $\text{H}(n,p)$ reactions only. The relative proton contamination can be estimated from the $^{12}\text{C}(n,p)$ cross sections given by Kurz¹⁸ and the atmospheric neutron energy spectrum of Lingenfelter¹⁹; it is

less than 3% of the protons from the $H(n,p)$ reaction for protons of equal energy.

The possible contamination due to the second reaction, $^{12}C(n,\alpha)$, was similarly estimated. There are two reaction channels through which these alphas are produced: $C^{12}(n,\alpha)Be^9$ and $C^{12}(n,3\alpha)n'$. For the atmospheric neutron energy spectrum, the first reaction predominates. The alpha contamination from $C^{12}(n,\alpha)Be^9$ was found to be about 7% of the protons from $H(n,p)$ for particles which yield equal integrated ($\int L dt$) scintillations. In the flight data we were able to extract separately the secondary alpha particles from the recoil protons. We found that the relative alpha particle contribution was approximately 10%, which was in good agreement with the estimated contribution. It should be noted that since the alpha particles were PSD'd from protons in this experiment, these alphas will not be counted as "protons".

The unfolded differential neutron energy spectrum at Pfozter maximum shown in Figure 8 was fitted to a spectral shape of the form:

$$dN/dE_n = BE^{-\beta(E)},$$

where $\beta(E)$, the spectral parameter is defined:

$$\beta(E) = \frac{E}{-\frac{dN}{dE}} \frac{d\left(\frac{dN}{dE}\right)}{dE}.$$

In Figure 9 $\beta(E)$ decreased smoothly with energy, ranging from 4.0 ± 1.0 at 3 MeV to 1.2 ± 0.7 at 20 MeV.

IV. DISCUSSION OF RESULTS

Since both the experimental technique used and the neutron energy spectrum are quite different from previous atmospheric neutron spectral measurements^{9,10,11,20}, we believe that a consideration of the various possible difficulties in atmospheric neutron measurements is imperative. First, let us evaluate semi-quantitatively and, second, consider the possible difficulties encountered in fast-neutron measurements in a background of charged particles.

In this experiment the largest uncertainties in the proton recoil spectrum shown in Figure 7 arise from statistical and systematic errors. The statistical errors per channel are easily evaluated to be 15-20 per cent. The systematic errors, on the other hand, are much more difficult to evaluate. The main contribution comes from the differential non-linearity of the logarithmic PHA in the lower channels. This is estimated to be comparable to the statistical errors for the lower channels of the flight PHA and considerable less than statistical for the upper channels. The cross-calibration curve to convert the

logarithmic PHA to a standard linear PHA that can then be converted easily to light units is shown in Figure 10. Since the channel width is small in the lower channels, two criteria were used to minimize systematic errors. First, the differential of the calibration curve must be smooth and nearly logarithmic. Second, the sum of all flight channel widths must equal the total width of the single channel analyzer constraining the $\int L dt$ range of the PHA. The error bars shown in Figure 7 are the most probable values from combining these two major sources of errors. To obtain the error bars shown in Figure 8 and Figure 9 the uncertainty in the slope was determined at the energies for which the errors are plotted.

The most serious possible experimental difficulties in atmospheric neutron measurements can be attributed to one or more of the following: Compton electrons not being properly identified by the PSD, charged particles "leaking" through the anticoincidence system and thereby being falsely measured as neutrals, and the PSD falsely identifying neutron-produced secondary alpha particles as recoil protons. Each of these effects will both increase and harden the "measured" neutron energy spectrum. This can be seen by comparing Figures 6(a), (b), and (c).

The effects of Compton electrons being mistakenly identified as protons by the PSD can be seen by comparing

the relative intensities of Compton electrons and recoil protons as well as the shapes of the electron and proton pulse-height spectra. The Compton-electron pulse-height data of Figure 6(c) are obviously a harder spectrum than the recoil-proton data of Figure 6(a). Since the ratio of electrons to protons was 14.2, a 1% error in the PSD separation can produce a 14% error in the proton flux. The large difference in spectral shape can introduce a greater than 10% error in the slope $\beta(E)$ of the neutron energy spectrum for a 1% error in the PSD separation.

The second experimental uncertainty can be evaluated from the charged-particle pulse-height spectrum measured by the neutron detector when the charged-particle anti-coincidence system was turned off. We observed that it was very similar in shape to the Compton-electron spectrum, i.e., a much harder and more intense spectrum than the recoil-proton spectrum. Therefore, the "leakage" of a small amount of charged particles into the neutron detector would produce a more intense and harder apparent recoil-proton spectrum.

Third, if the PSD cannot separate alpha particles from recoil protons, both types of events are recorded as recoil protons. This would produce an increase of about 10% in the recoil-proton flux, as can be seen by comparing Figures 6(a) and 6(b). This again yields a more intense neutron spectrum.

V. CONCLUSIONS

We have found that the differential neutron energy spectrum at Pfozter maximum at 42°N geomagnetic latitude was considerably steeper in the energy interval 3-10 MeV (Figure 9) than previously measured spectra. The spectral parameter $\beta(E)$ for the differential neutron energy spectrum decreased smoothly from 4.0 ± 1.0 at 3 MeV to 1.2 ± 0.5 at 20 MeV. The calculated neutron flux in the energy range 3.5 to 10 MeV was 0.36 ± 0.10 neutrons/cm²sec, about that obtained earlier by Mendell²⁰. It is clear that the question of a possible change in the neutron energy spectrum between Pfozter maximum and the top of the atmosphere remains unresolved. The intensity and shape of the neutron energy spectrum between 3-100 MeV is important to the evaluation of the contributions made by neutron leakage to the population of energetic protons in the inner radiation belt. The results of this experiment show the necessity of using caution in interpreting earlier experiments and indicate that excellent PSD techniques must be used in atmospheric neutron measurements. Any linear extrapolations of the differential neutron energy spectrum to higher energies⁷ cannot be justified.

ACKNOWLEDGMENTS

The assistance of Messrs. L. Friling, D. Schow, and D. Huntley with the electronics design and construction is greatly appreciated. Messrs. A. Buck and K. Pratt handled the data reduction. We are grateful to Drs. W. Burrus and V.V. Verbinski of Oak Ridge National Laboratory for many helpful discussions. This research was in partial fulfillment of the requirements of a Ph.D. degree (R. N. St. Onge) and was supported by NASA under contract NASr-164 and the Air Force under contracts AF19(628)-2352 and F19628-68-C-0107.

FOOTNOTES

1. S. F. Singer, Phys. Rev. Letters 1, 181 (1958).
2. E. Schopper, E. Lohrmann and G. Mauchk, Encyclopedia of Physics (Springer-Verlag, New York, 1967) p. 372.
3. W. N. Hess, Phys. Rev. Letters 3, 1 (1959).
4. L. I. Newkirk, J. Geophys. Res. 68, 1825 (1963).
5. R. E. Lingenfelter, J. Geophys. Res. 68, 5633 (1963).
6. A. J. Dragt, M. M. Austin, and R. S. White, J. Geophys. Res. 71, 1293 (1966).
7. W. N. Hess and J. Killeen, J. Geophys. Res. 71, 2799 (1966).
8. R. C. Haymes, J. Geophys. Res. 69, 841 (1964).
9. S. S. Holt, R. B. Mendell, and S. A. Korff, J. Geophys. Res. 71, 5109 (1966).
10. G. A. Baird and B. G. Wilson, Can. J. Phys. 44, 2131 (1966).
11. R. B. Mendell and S. A. Korff, J. Geophys. Res. 68, 5487 (1963).
12. A. D. Zych and G. M. Frye, Jr., Bull. Am. Phys. Soc. 13, 1434 (1968).
13. R. N. St. Onge and J. A. Lockwood, Nucl. Instr. and Methods (1969).
14. R. N. St. Onge and J. A. Lockwood, Nucl. Instr. and Methods 69, 25 (1969).

FOOTNOTES(cont.)

15. V. V. Verbinski, W. R. Burrus, T. A. Love, W. Zobel, N. W. Hill, and R. Texter, Nucl. Instr. and Methods 65, 8 (1968).
16. H. W. Broek and C. E. Anderson, Rev. Sci. Instr. 31, 1063 (1960).
17. J. B. Marion and J. L. Fowler, Fast Neutron Physics (Interscience Publishers, Inc., New York, 1960) ch. 2B, p. 211.
18. R. J. Kurz, Ph.D. Thesis, University of California, Berkeley (1964).
19. R. E. Lingenfelter, Rev. of Geophysics 1, (1963).
20. R. B. Mendell, Private Communication, (1969).

FIGURE CAPTIONS

- Figure 1 Charged-particle anticoincidence shield design.
- Figure 2 Parallel sum and coincidence logic of the
charged particle shield system.
- Figure 3 A two-parameter (64 x 64) contour display of
Compton electrons, recoil protons and inflight
calibrator (IFC) for a laboratory prototype.
The widths of the dark bands are equal to one
full width at half maximum (FWHM).
- Figure 4 A section of Figure 3 taken at the $\int L \, dt$ value
corresponding to the Compton edge of Co^{60} .
- Figure 5 Two-parameter ($\int L \, dt$ vs dL/dt) flight data
taken from 541 to 62 mbar.
- Figure 6(a) Recoil-proton count rate data from Figure 5.
- 6(b) The secondary alpha-particle spectrum
extracted from Figure 5.
- 6(c) The uncorrected Compton-electron spectrum
taken from Figure 5.
- Figure 7 The recoil-proton energy spectrum obtained
from the data in Figure 6(a). To obtain the
actual number of protons/MeV multiply the
ordinate by 1.42.

FIGURE CAPTIONS(cont.)

- Figure 8 The differential neutron energy spectrum at Pfozter maximum. The actual neutron flux is 3.22 times the ordinate.
- Figure 9 The logarithmic slope of the differential neutron energy spectrum at Pfozter maximum as a function of energy.
- Figure 10 The linear (Technical Measurements Corp.) channel number as a function of flight channel number for $\int L \, dt$ pulses.

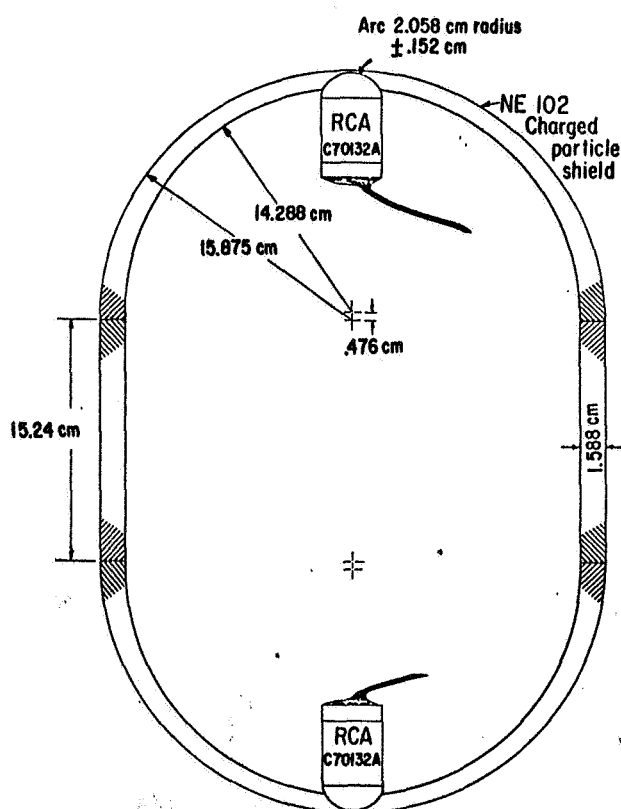
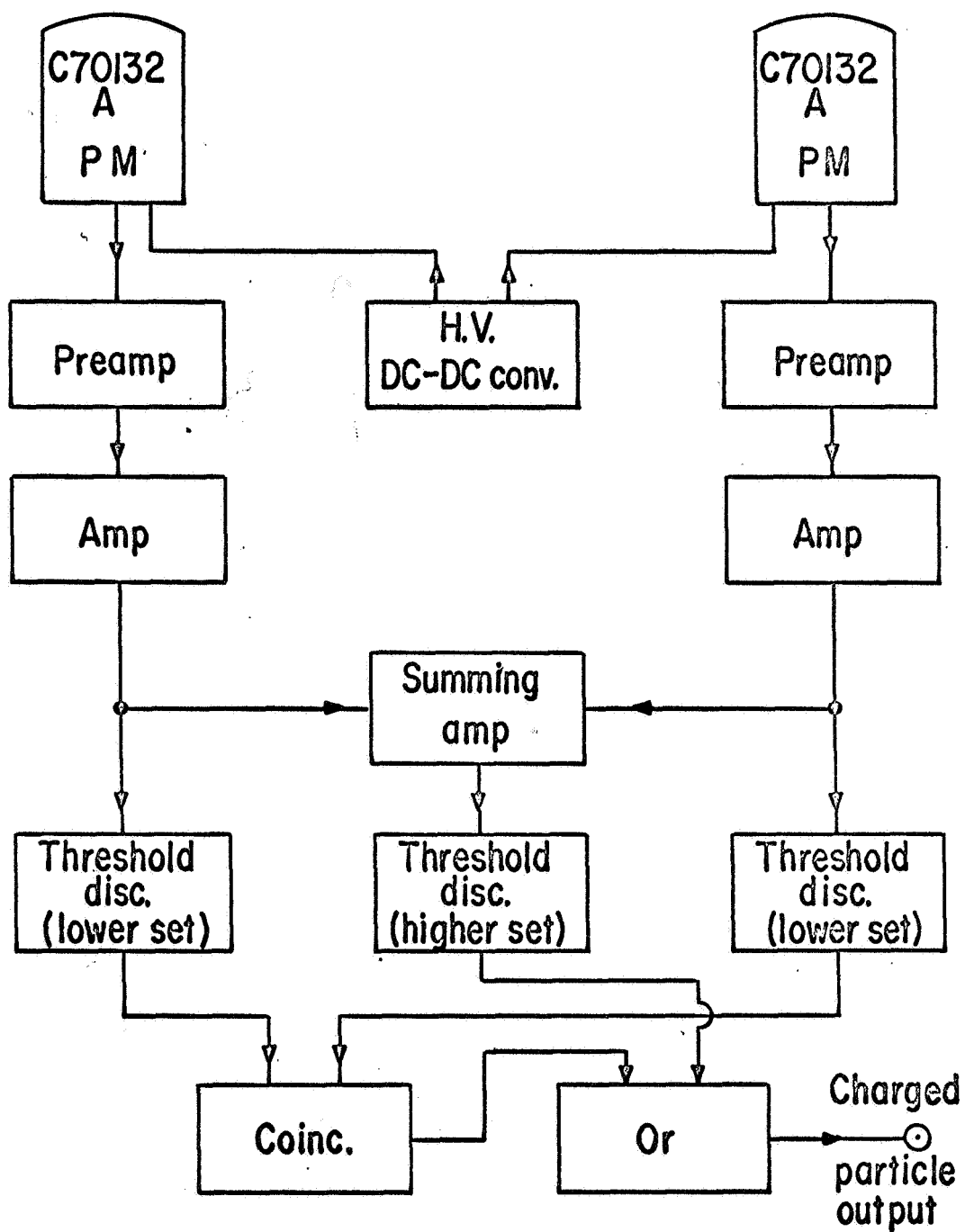


Figure 1



Charged particle shield system

Figure 2

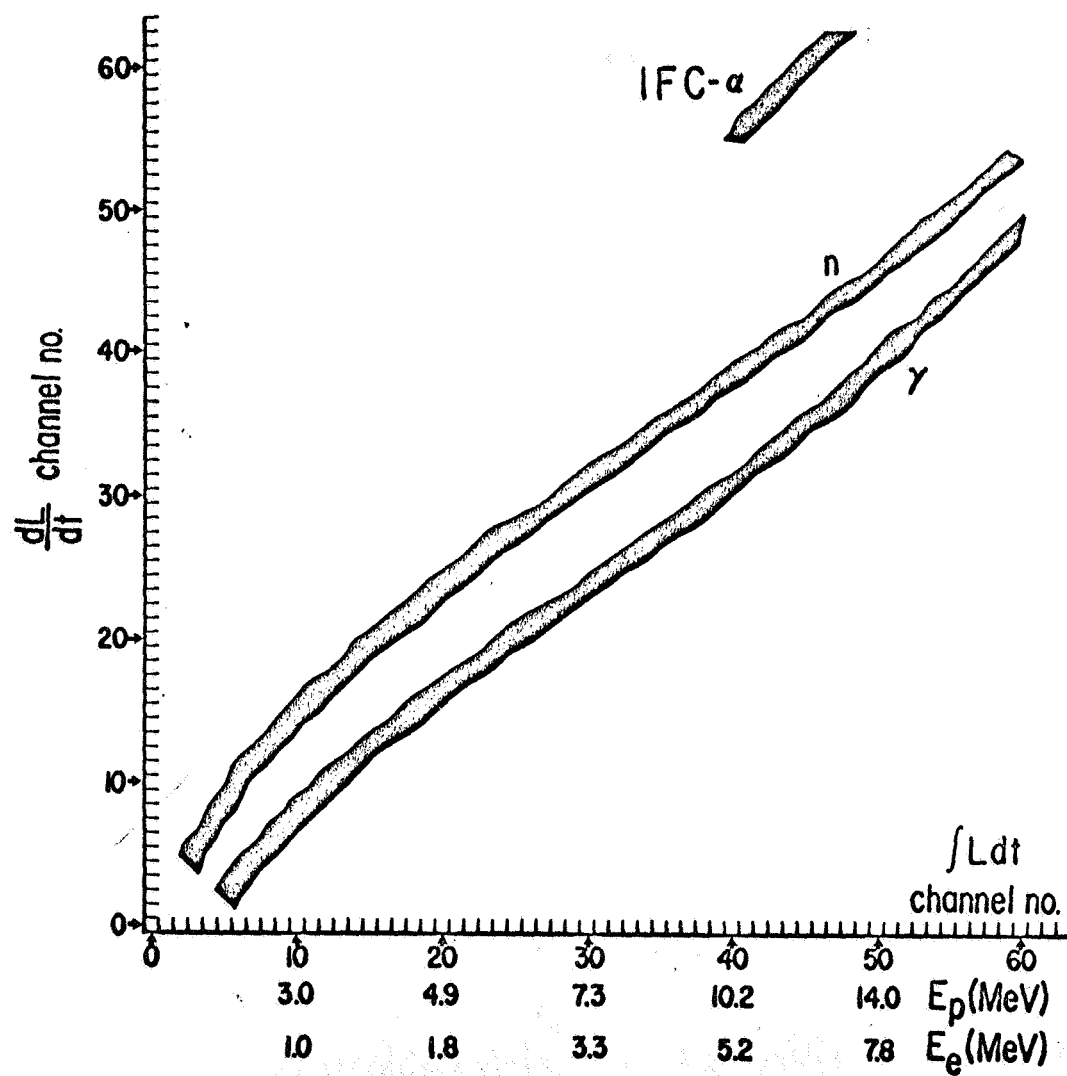


Figure 3

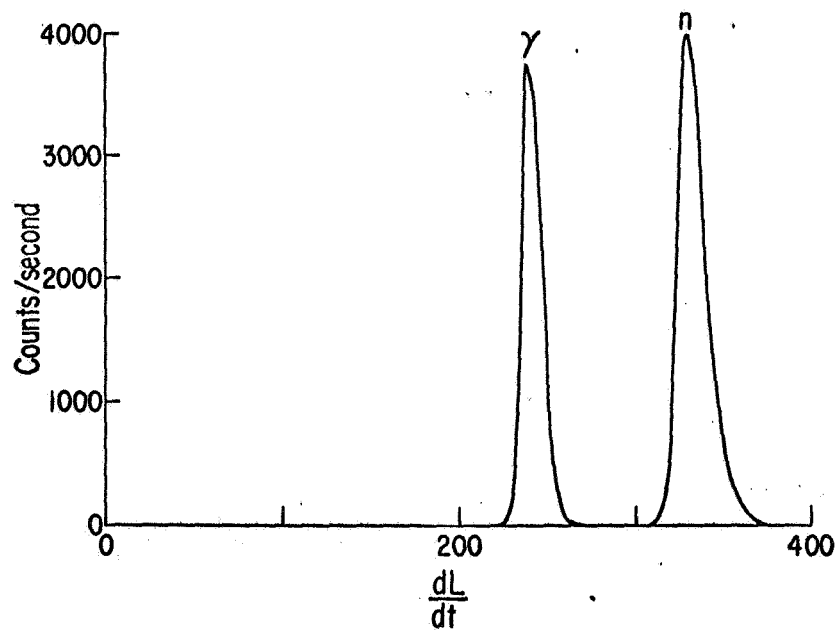


Figure 4

← dL/dt

131

IFC

→ Ldt

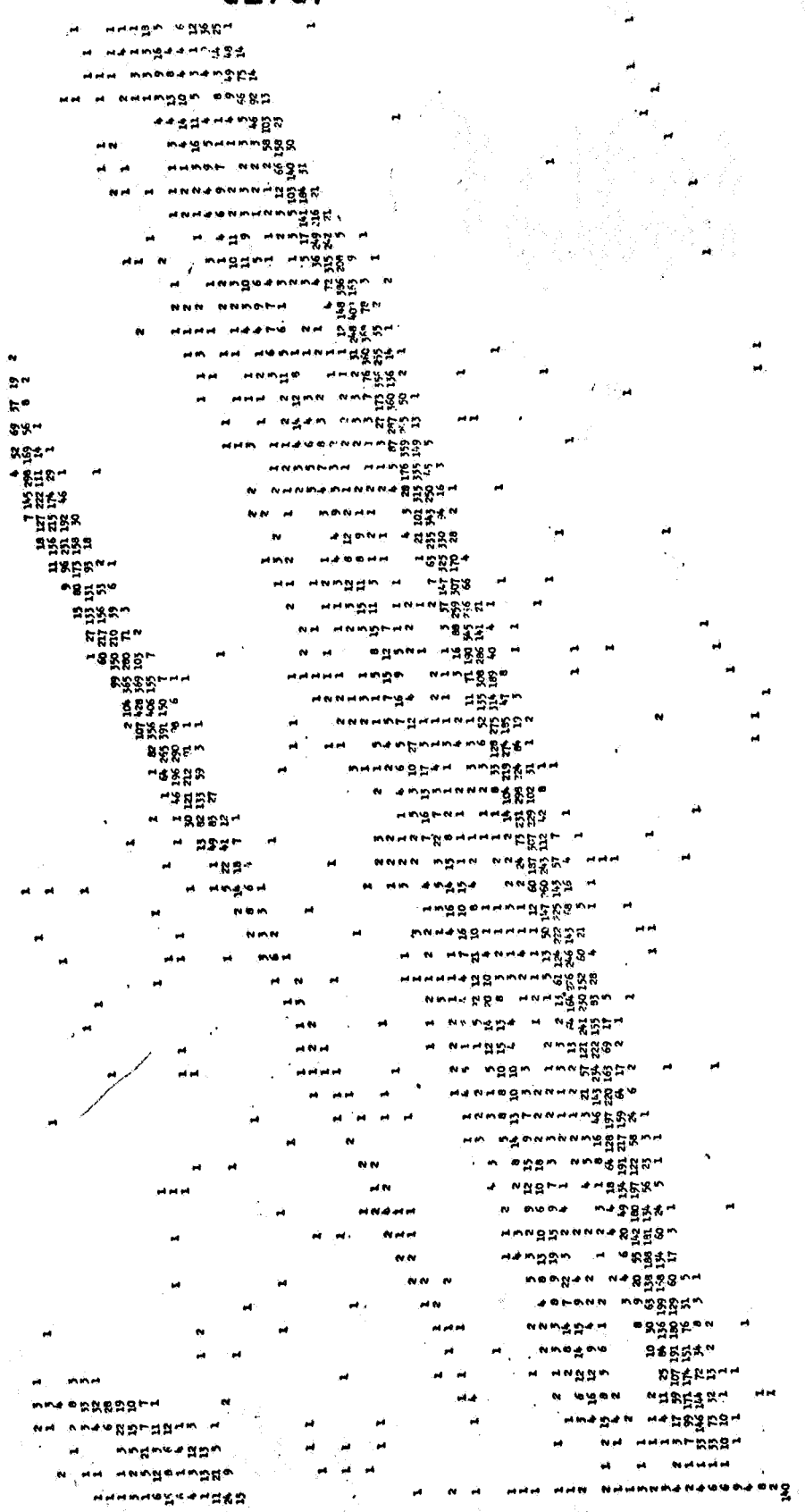


Figure 5

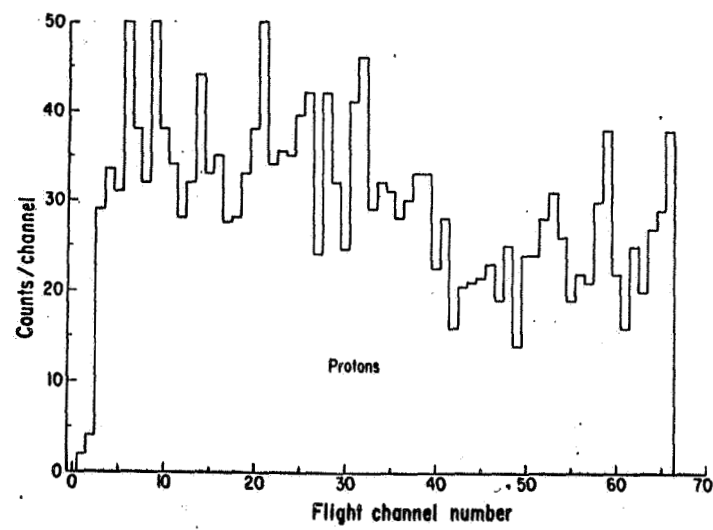


Figure 6(a)

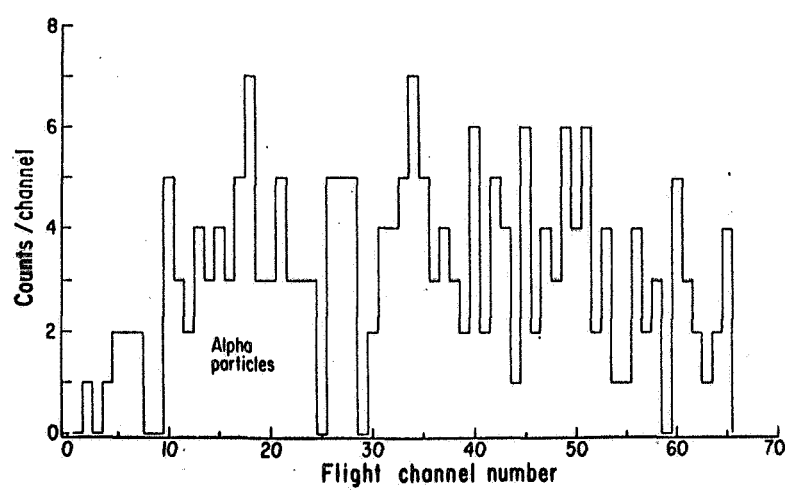


Figure 6(b)

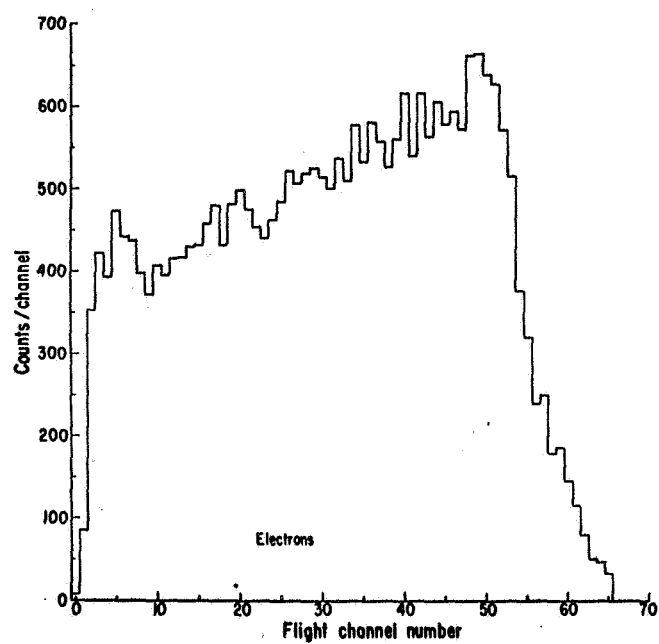


Figure 6(c).

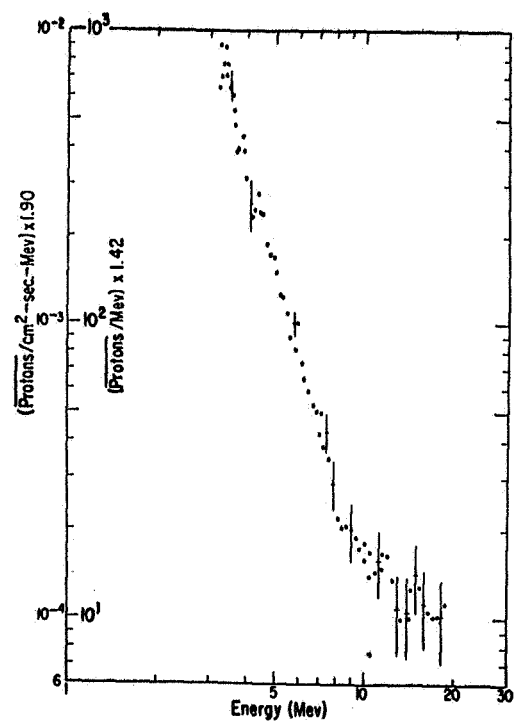


Figure 7

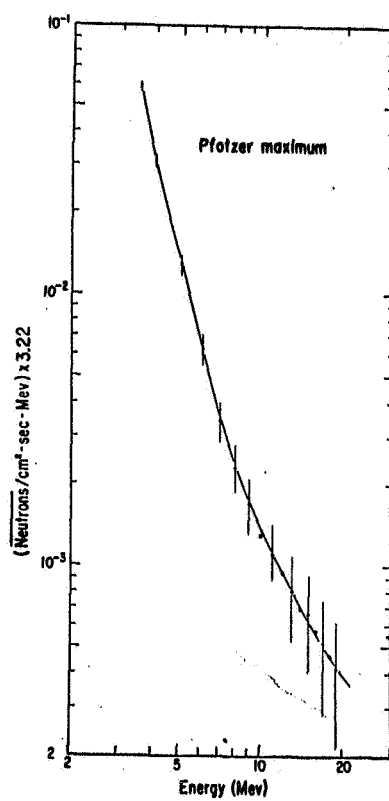


Figure 8

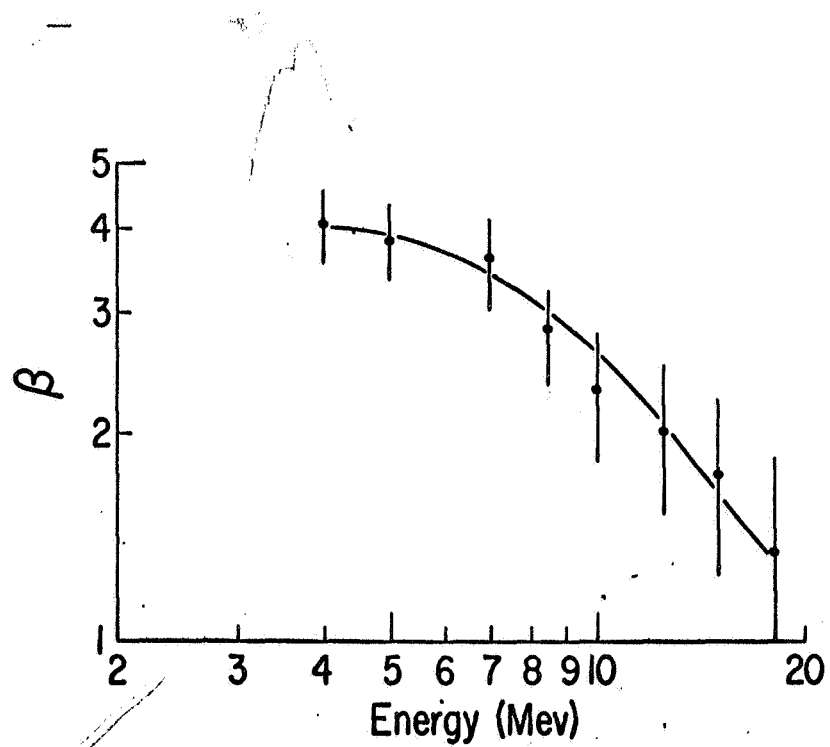


Figure 9

IONOSPHERIC MEASUREMENTS PUBLICATIONS

R. E. Houston et al.

ELECTRON DENSITY MEASUREMENTS
FROM SOUTHERN LATITUDE ROCKET FLIGHTS

R. E. Houston and L. E. Larson*
University of New Hampshire
Physics Department
Durham, New Hampshire

ABSTRACT

Propagation experiments in the 1 Mc/s and 3 Mc/s range have been utilized to determine electron distributions in the lower ionosphere. Nike-Apache flights at 12° , 30° , and 60° geographic south latitude provided data for computational techniques based on the Sen-Wyller form of the generalized Appleton-Hartree equations. Faraday rotation data obtained from the rocket telemetry signal and the appropriate linearly polarized ground based transmission are used to determine the difference in the ordinary and extraordinary indices of refraction. This difference is compared to a difference value generated by the Sen-Wyller equations.

Values of collision frequency are obtained from the differential absorption data of the ordinary and extraordinary waves as well as from theory.

Electron densities of the order of $5 \times 10^4 \text{ el/cm}^3$ at 100 km are obtained for all flights.

Comparison between values obtained by the above method and ionosonde techniques will be made.

This research was sponsored by the National Aeronautics and Space Administration under Contract NASr-164.

* Present address is Denison University, Granville, Ohio

LOWER IONOSPHERIC PARAMETERS AS MEASURED FROM SOUNDING ROCKETS

R. E. Houston and L. E. Larson*
 University of New Hampshire
 Physics Department
 Durham, New Hampshire

In a recent flight from Fort Churchill, Manitoba, propagation experiments in the 1 Hz/s and 3 Hz/s range were utilized to determine electron density profiles from approximately 65 km to 100 km. Measurement of the neutron albedo (thermal energy to 15 MeV) and charged particles (100 MeV and up) resulting from the incident cosmic-ray flux were carried out over the same altitude regime. A detailed comparison of these results is made.

In addition, measurements of the $^{1217}\text{Å}$ and $^{1450}\text{Å}$ radiation flux along with the X-ray flux in the 2 Å - 12 Å range were obtained.

The electron density profile is obtained from the generalized Sen-Wyller equation using Faraday rotation data from the rocket telemetry signal and the appropriate linearly polarized ground based transmission. Electron densities of the order of 100 el/cm^3 at 65 km and $5 \times 10^4\text{ el/cm}^3$ at 100 km were obtained. These will be compared to values obtained recently in Southern latitude measurements.

This research was sponsored by the National Aeronautics and Space Administration under Contract NASr-164.

* Present address is Denison University, Granville, Ohio

A MEASUREMENT OF THE EFFECTIVE RECOMBINATION
COEFFICIENT IN THE LOWER IONOSPHERE

R. E. Houston and L. E. Larson*
University of New Hampshire
Physics Department
Durham, New Hampshire

ABSTRACT

Utilizing the charged particle spectra obtained on a recent Nike-Tomahawk firing, the production of electrons in the lower ionosphere was calculated. On the same rocket a Faraday rotation experiment measured the electron density. The ratio of the electron production to the square of the electron density is the effective recombination coefficient, α_{eff} . The results obtained through this technique give a value for α_{eff} of approximately $6 \times 10^7 \text{ cm}^3/\text{sec}$ at 65 kilometers. This value is in reasonable agreement with that cited by other authors. Closer agreement is achieved when recent experimental values of the negative ion ratio are substituted in the earlier work.

* Present address is Denison University, Granville, Ohio

A SENSITIVE RADIO RECEIVER FOR IONOSPHERIC MEASUREMENTS

A Sensitive Radio Receiver for Ionospheric Measurements*

F. D. Szachta[†], R. E. Houston, Jr., and L. E. Larson[†]

Department of Physics, University of New Hampshire, Durham, New Hampshire 03824

A sensitive, narrow band, amplitude modulated radio receiver was designed to measure the electron density in the lower ionosphere.

The method employed was to send a continuous wave linearly polarized signal from a ground-based transmitter to a receiver located in a rocket payload. Modulation was provided by the spin of the rocket about its vertical axis which continually swept the dipole (loopstick) receiving antenna through the polarized electromagnetic field. The plane of polarization of the wave changes and it is attenuated by amounts which depend on the wave frequency, number density of free electrons, electron collision frequency, and electron gyrofrequency. If the collision frequency is measured by an independent method, then the angle through which the plane of polarization rotates per unit altitude (Faraday Rotation) can be related to the electron density.¹

The receiver circuit diagram is shown in Figures 1 and 2. The antenna was formed by winding a coil on a 1.6 x 14.0 cm cylindrical ferrite rod, and placing a capacitor in parallel with the coil such that it resonated at the desired frequency. Coupling to the rf stage was accomplished by a second coil wound around the rod.

The rf amplifier was a standard common emitter class A tuned amplifier. The local oscillator and mixer, which was combined to eliminate one stage, basically consisted of a crystal controlled Colpitts oscillator whose circuit parameters were chosen so that it would oscillate well over a range of frequencies (\sim 1-4 MHz) with just a change of crystal. Two crystal filters² were installed in this stage, one in the base circuit to prevent self-oscillations by effectively grounding the base at the i.f. frequency, and the other in parallel with the emitter circuit to enhance the gain at this one frequency only.

The three i.f. sections were identical, each using a transfilter³ for the frequency selection element. The resonant frequency of a transfilter is fixed. This is a desirable feature as the rapid acceleration and severe vibration of the vehicle cannot cause any alterations of settings during flight. A crystal filter was installed in each emitter circuit to improve the gain at the i.f. frequency. It should be noted that the capacitive component in the input and output impedances to the transfilters altered their resonant frequency by as much as 2 kHz. This necessitated measuring the frequency of best response for each completed receiver and selecting a transmitter crystal for each flight with a frequency matched to the measured receiver resonant frequency.

The detector was standard. The audio amplifier was designed to have good low frequency response since the signal modulation frequency was 6-20 Hz. A zener diode across the output limited the output voltage to 5 v (a standard telemetry requirement).

The automatic gain control (AGC) consisted of a feedback network which changed the biasing of the rf and i.f. stages such that their gain was reduced when a large input signal to the receiver was present. The time constant of this AGC circuit was about 2 sec so that the slow modulation of the signal received would not appear to be a signal strength change.

The completed receiver had a bandwidth of 2.2 kHz and the center frequency was stable within 60 Hz over a period of 1 hour and varied less than 300 Hz over a temperature range of -10 to +50° C. The sensitivity of a typical receiver was such that a 5 μ v/m field at the antenna^{5,6} resulted in an output signal well above the background noise.

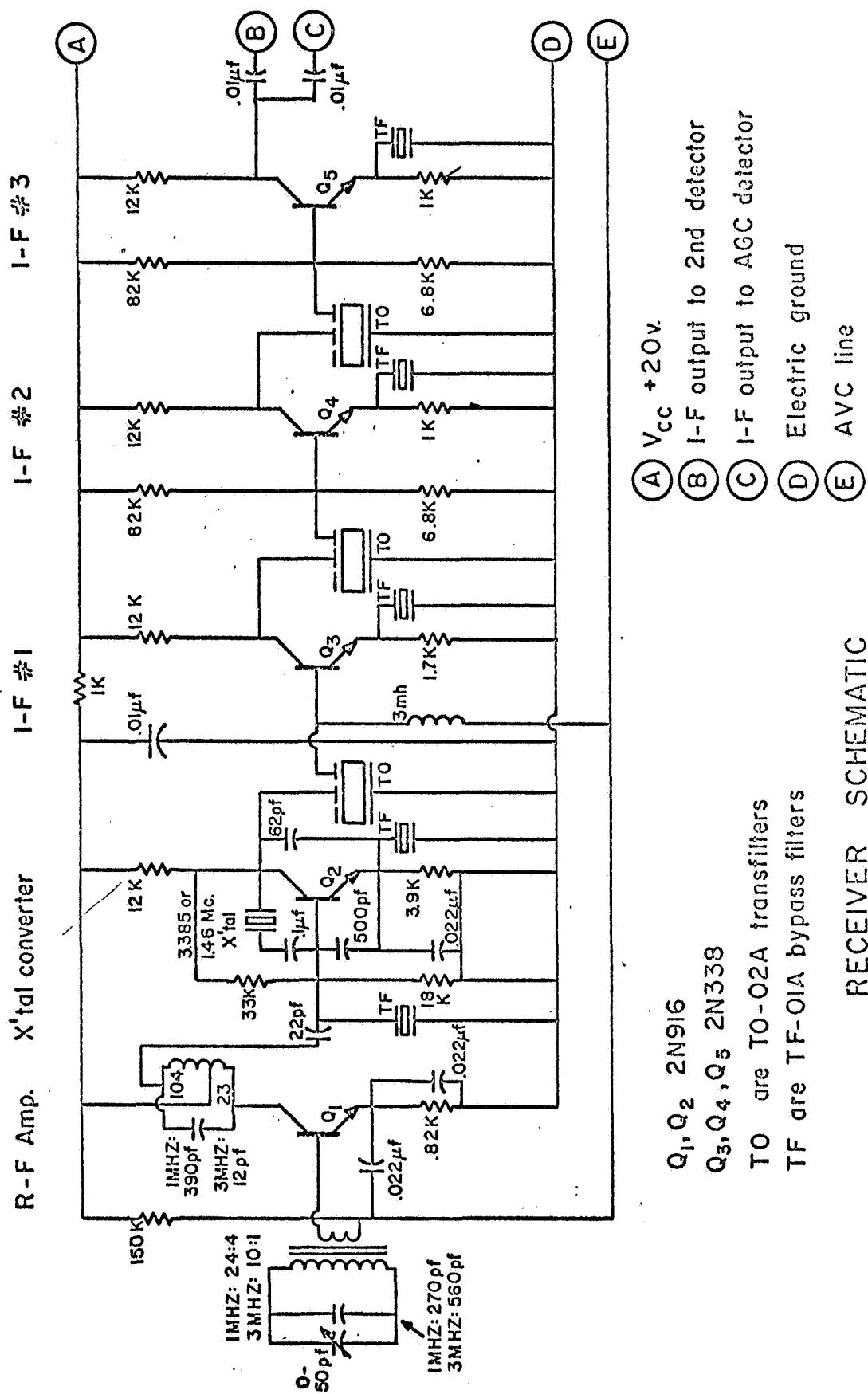
A printed circuit layout was used, and the completed units measured 7.0 x 10.0 x 2.5 cm. Receivers and antennas were encapsulated before flight to add mechanical strength. At this time 8 receivers have been successfully flown, some operating at 1.005 MHz and others at 3.385 MHz. The only changes required to allow the basic receiver to operate reliably at any frequency in this range were to suitably alter the antenna winding, to select a capacitor in the rf section that amplified the desired frequency, and to use the proper oscillator crystal. Parts, excluding the printed circuit board, cost about \$130.00.

- * Supported by the National Aeronautics and Space Administration under Contract NASr-164.
 - † Present address: McChord Air Force Base, Tacoma, Washington 98439
 - + Present address: Dept. of Physics, Denison University, Granville, Ohio
1. H. K. Sen and A. A. Wyller, J. Geophys. Research 65, 3931 (1960)
 2. Type TF-01A, Clevite Corporation, Piezoelectric Division, Bedford, Ohio
 3. Type TO-02A, Clevite Corporation
 4. F. D. Szachta, The Design of an Improved Receiver for Rocket Experiments, M.S. Thesis, Dept. of Electrical Engineering, University of New Hampshire (1965).
 5. IRE Standards on Radio Receivers, Methods of Testing Amplitude Modulation Broadcast Receivers (1948)
 6. IRE Standards on Radio Receivers, Methods of Testing Receivers Employing Ferrite Core Loop Antennas (1955)

Figure Captions

Fig. 1. Receiver circuit diagram - rf and i.f. stages.

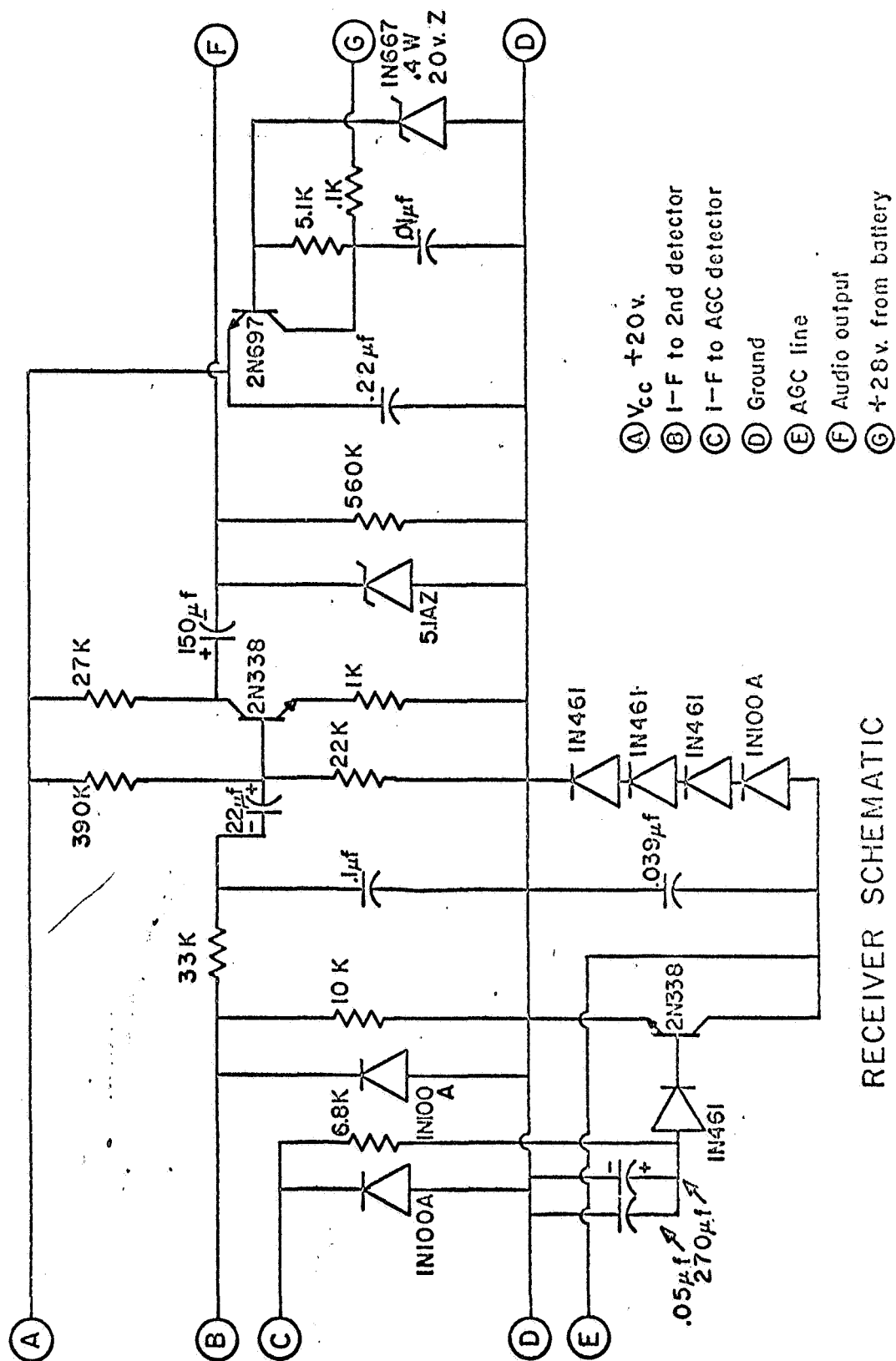
Fig. 2. Receiver circuit diagram - detector, AGC, audio, and voltage regulator stages.



VOLTAGE REGULATOR

AUDIO AMP

AGC AMP



RECEIVER SCHEMATIC

FIGURE 2

A MEASUREMENT OF THE EFFECTIVE RECOMBINATION
COEFFICIENT IN THE LOWER IONOSPHERE

A MEASUREMENT OF THE EFFECTIVE RECOMBINATION
COEFFICIENT IN THE LOWER IONOSPHERE

Lee E. Larson

Denison University, Granville, Ohio 43023

and

R. E. Houston, Jr.

University of New Hampshire, Durham, N. H. 03824

INTRODUCTION

The rate coefficients for free electron loss processes in the lower ionosphere are at present still subject to some question, with recent values reported in the literature varying over more than an order of magnitude (Webber (1962), Adams and Masley (1965)). One technique which can be used to measure an effective recombination coefficient is to measure simultaneously the electron concentration and the rate of electron production, and to derive the recombination coefficient from these measurements.

On June 7, 1967 (during a solar proton event) a Nike Tomahawk sounding rocket was flown from Churchill, Manitoba, which recorded the charged particle flux, Lyman α and 2-12A^o x-ray fluxes, and the electron concentration. These data are used here to find a value for the effective recombination coefficient in the range of 60-70 km.

THEORY

The rate of change of free electron number density in the lower ionosphere can be written as

$$\frac{dN_e}{dt} = Q - \alpha_D N_e N_A - \beta N_e + \gamma N^- N + \rho N^- \quad (1)$$

where Q = electron production rate, and N_e , N_A , N , and N^- are the electron, positive ion, neutral particle, and negative ion densities respectively.

α_D = electron-positive ion recombination coefficient

β = electron attachment coefficient

γ = collisional detachment coefficient

ρ = photodetachment coefficient

This expression can be simplified by writing

$$\frac{dN^-}{dt} = -\alpha_i N^- N_A + \beta N_e - \gamma N^- N - \rho N^- \quad (2)$$

where α_i = the ion-ion recombination coefficient. If we define $\lambda = N^-/N_e$, assume $d\lambda/dt = 0$, and utilize equation (2), equation (1) can be rewritten as

$$\frac{dN_e}{dt} = \frac{Q}{1+\lambda} - (\alpha_D + \lambda \alpha_i) N_e^2 \quad (3)$$

If the electron concentration changes slowly with time,

$$\frac{Q}{N_e^2} = (1+\lambda) (\alpha_D + \lambda \alpha_i) = \alpha_{eff} \quad (4)$$

Therefore, the effective rate coefficient may be found by measuring the electron concentration and the rate of electron production.

PRODUCTION RATE

The charged particle detection system, which consisted of a bank of proportional counters, as well as the method of deriving the observed proton spectrum are fully described by Lockwood and Friling (1968).

The integral spectrum determined for this flight is shown in Figure 1. It can be seen that the flux measurements fit an exponential integral rigidity spectrum

$$J(>P) = J_0 e^{-\frac{P}{P_0}}$$

with $J_0 = 700 \text{ (cm}^2 \text{ sec)}^{-1}$ and $P_0 = 60 \text{ Mv}$. J is the total flux of particles above rigidity (momentum per charge) P . Lockwood and Friling (1968) assume that the counts observed are due entirely to protons, and the flux is assumed to have 2π isotropy. It should be noted that this enhancement of the low energy proton flux can also be seen in data from Explorer 34 (Environmental Science Services Administration, 1968). The spectrum from Explorer 34 cannot be compared to the one found by Lockwood and Friling since the satellite was well outside the magnetosphere at this time.

The electron production rate Q was calculated using the method described by Adams and Masley (1965). The

specific production rate q , which is the rate of production of electron-ion pairs at an altitude z by a flux of l particle/cm² sec. of energy E is calculated. Then, Q can be found at altitude z by

$$Q(z) = \int_{E = E_c}^{150 \text{ Mev}} q j(E) \Delta E$$

where $j(E)$ is the flux of protons in an energy band ΔE centered at E and E_c is the effective geomagnetic energy cutoff. With the large flux of low energy particles present during the flight, it is found that over the altitude range considered, the effect on Q of particles with $E > 150$ Mev is negligible.

Shea et al. (1963) calculate the vertical cutoff rigidity at Churchill as < 210 Mv (~ 20 Mev), and a recent experimental value is given by Webber (1968) as 160 Mv (14 Mev). The latter value was adopted for this work, although if the former is used it changes the results by less than a factor of 2. The resulting Q as a function of altitude is shown in Figure 2.

It is assumed that the low energy protons were the only ionizing source. Flux measurements of Lyman α (1216⁰Å) and 2-12⁰Å x-rays, thought to be the other possible ionizing radiations in this region, indicate that these did not reach below 70 km during the flight (solar zenith angle $\chi = 58^\circ$). Calculations confirm that these radiations should be absorbed above 70 km.

ELECTRON DENSITY

The electron density was determined by measuring the angle ψ through which a 3.385 MHz linearly polarized radio wave rotates as a function of altitude in the ionosphere. It can be shown that

$$\frac{d\psi}{dz} = \frac{\omega}{2c} (n_1 - n_2) \quad (5)$$

where ω = wave frequency

c = speed of light

n_1, n_2 = 2 values of the ionospheric index of refraction

Also,

$$n_1 = F_1(\omega_o^2, \omega, s, \nu) \quad (6a) \quad n_2 = F_2(\omega_o^2, \omega, s, \nu) \quad (6b)$$

where F_1 and F_2 are functions determined from the generalized magnetoionic theory (Sen & Wyller, 1960).

$$\omega_o^2 = \frac{4\pi N_e e^2}{m_e}, \text{ the plasma frequency}$$

$$s = \frac{eH}{m_e c}, \text{ the electron gyrofrequency}$$

$$\nu = \text{electron collision frequency.}$$

The electron collision frequency was obtained by observing the attenuation of the Lyman α radiation in the earth's atmosphere, relating this quantity to the

atmospheric pressure, and using the experimental relationship between pressure and electron collision frequency (Phelps, 1960) as described by Aikin, Kane, and Troim (1964). The collision frequencies derived are shown in Figure 3. An experimental value of $(n_1 - n_2)$ can be determined from equation (5) since $d\psi/dz$ is a measured quantity. Also a computed value of $(n_1 - n_2)$ was found from equations (6) using an assumed value of N_e . The experimental and theoretical values were then compared, and the assumed value of N_e was corrected by an iterative process until the computed value of $(n_1 - n_2)$ matched the experimental value, resulting in a unique determination of N_e .

The electron density profile is shown in Figure 4. The uncertainties are due primarily to uncertainties in the value of $d\psi/dz$.

RECOMBINATION COEFFICIENTS

Using the data from Figures 2 and 4, and equation (4) the recombination coefficients shown in Figure 5 are obtained. Also shown on the same graph are values determined by Webber (1962) and by Adams and Masley (1965). The values originally reported by Adams and Masley should be corrected by a factor of 2.27 (private communication, Adams, 1968) and this has been done here. The measurements reported here show fair agreement with those of Adams & Masley at lower altitudes but indicate fairly large discrepancies in the upper altitude range. Good agreement

is seen with Webber except for the middle part of the range. Here, Webber's data could be brought into closer agreement if his values of λ were assumed to be somewhat smaller. Recent measurements by Hale et al. (1968) indicate that it is possible for λ to stay constant with a value of 3 from 60 to 65 km increasing to a value of 5 from 67 to 70 km. It can be seen from equation (4) that if these values of λ for this altitude region are substituted for those used by Webber, that his value of α_{eff} in this region would correspond very closely with that determined by the present authors.

CONCLUSIONS

It is concluded on the basis of this one flight in which the low energy solar proton flux was sufficient to give a measurable electron density, that the method reported here is one of the most direct ways to determine α_{eff} . It is obvious that there are still discrepancies present in recent determinations of the effective recombination coefficient, and that more flights of this type could be used to ascertain the correct value.

ACKNOWLEDGMENTS

This work was supported by the National Aeronautics and Space Administration under Grant NASr-164.

The authors gratefully acknowledge the contributions of Mr. Gene Adams, ESSA, Boulder, Colorado.

REFERENCES

- Adams, G. W. and A. J. Masley, Production Rates and Electron Densities in the Lower Ionosphere due to Solar Cosmic Rays, J. Atmosph. Terr. Phys. 27, 289-298, 1965.
- Aikin, A. C., J. A. Kane, and J. Troim, Some Results of Rocket Experiments in the Quiet D-Region, J. Geophys. Res. 69, 4621-4628, 1964.
- Environmental Science Services Administration, Solar Geophysical Data IER-FB-282, February 1968.
- Hale, L. C., D. P. Hoult, and D. C. Baker, A Summary of Blunt Probe Theory and Experimental Results, Space Research VIII, pp. 320-331, North Holland Publishing Company, Amsterdam, 1968.
- Lockwood, J. A. and L. A. Friling, Cosmic Ray Neutron Flux Measurements above the Atmosphere, to be published, J. Geophys. Res. 73, 1968.
- Sen, H. K. and A. A. Wyller, On the Generalization of the Appleton-Hartree Magnetoionic Formulas, J. Geophys. Res. 65, 3931-3950, 1960.
- Shea, M. A., D. F. Smart, and K. G. McCracken, A Study of Vertical Cutoff Rigidity using Sixth Degree Simulations of the Geomagnetic Field, J. Geophys. Res. 70, 4117 - 4130, 1965.
- Webber, W. R., The Production of Free Electrons in the Ionospheric D-Layer by Solar and Galactic Cosmic Rays and the Resultant Absorption of Radio Waves, J. Geophys. Res. 67, 5091-5106, 1962.
- Webber, W. R., Diurnal Variation of the Intensity and Energy Spectrum of Low Energy Electrons Incident at Ft. Churchill, Canada, J. Geophys. Res. 73, 4905-4913, 1968.

FIGURE CAPTIONS

- Figure 1 - Integral proton flux versus rigidity measured on flight 18.29, 7 June, 1967.
- Figure 2 - Electron production versus altitude, 7 June, 1967.
- Figure 3 - Electron collision frequency versus altitude, 7 June, 1967.
- Figure 4 - Electron density versus altitude, 7 June 1967.
- Figure 5 - Effective recombination coefficient versus altitude as determined by data obtained on flight 18.29, 7 June 1967.

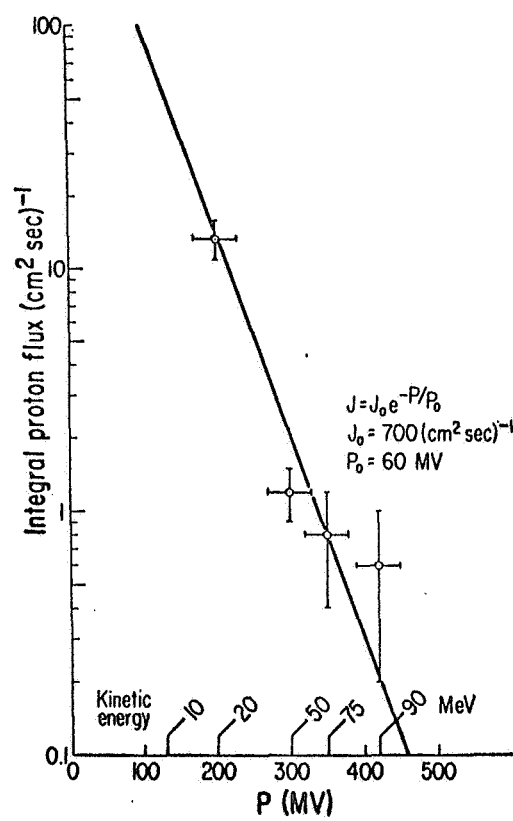


Figure 1

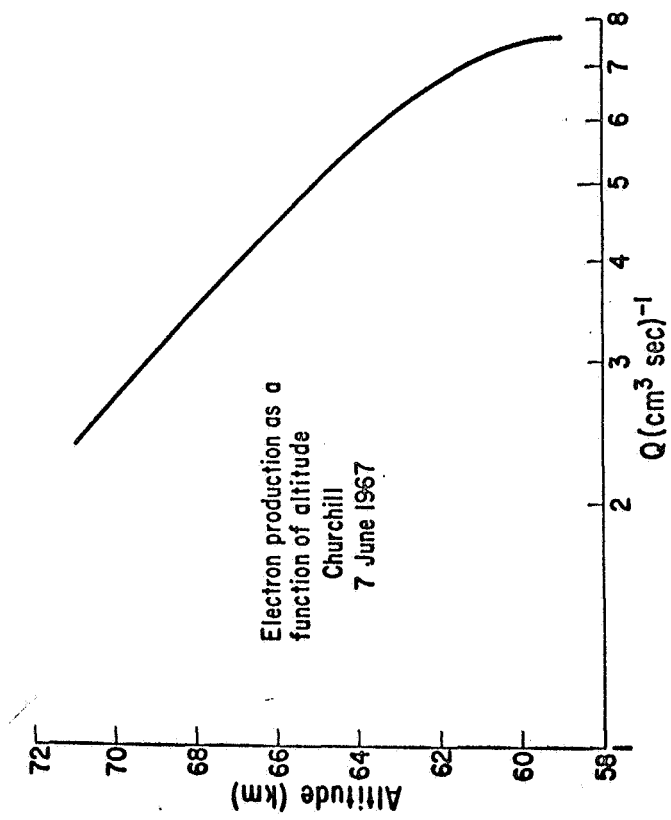


Figure 2

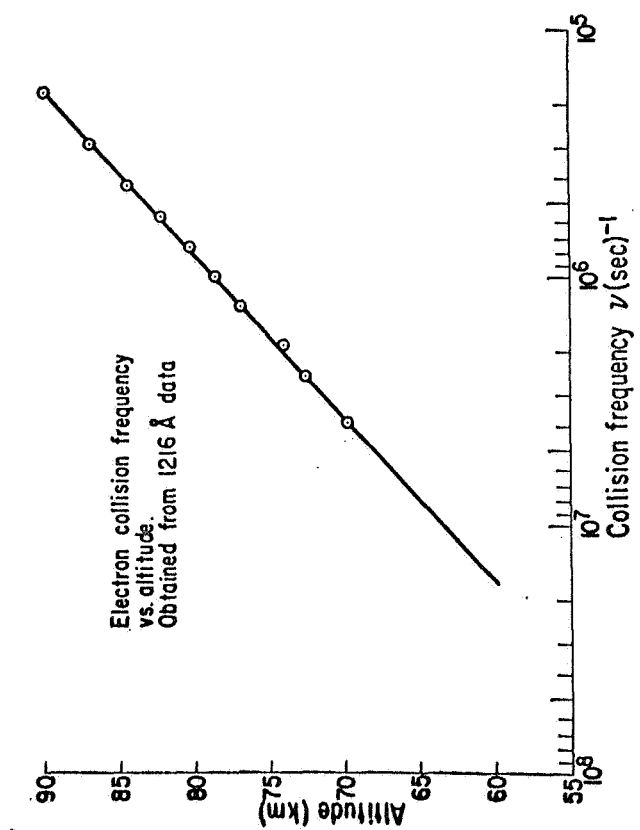


Figure 3

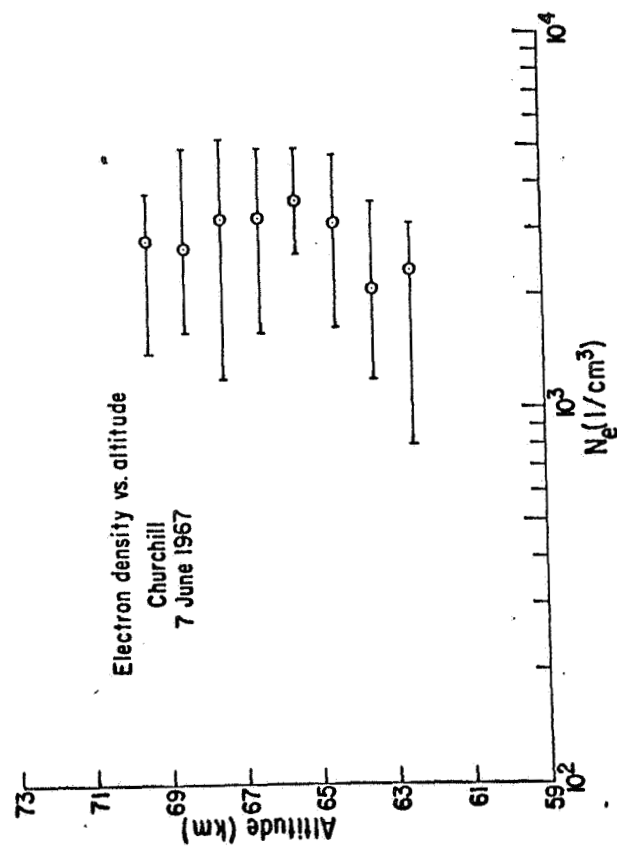


Figure 4

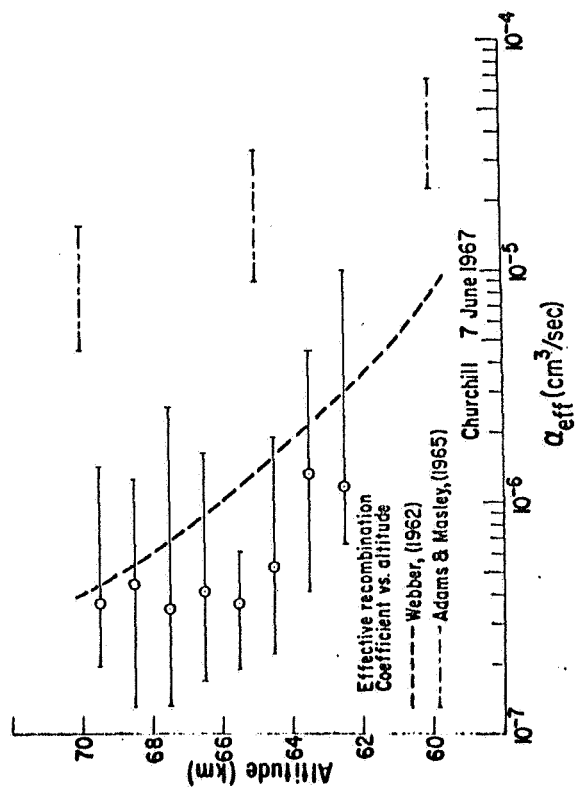


Figure 5